The Effect of Late Holocene Ice-Mass Changes on Glacial Isostatic Adjustment in West Antarctica

Grace A. Nield

Thesis submitted for the degree of
Doctor of Philosophy

School of Civil Engineering and Geosciences
Newcastle University

November 2014

Abstract

Glacial isostatic adjustment (GIA) describes the Earth's response to changing ice and water loads as ice sheets grow and diminish. GIA is difficult to model in Antarctica due to limited knowledge of ice history and Earth properties. The signal confounds satellite gravity measurements of present-day ice-mass change and needs to be accurately removed, but remains the biggest uncertainty. One problem with current Antarctic GIA models is that they neglect ice-mass changes over the past few thousand years, which, in regions of low viscosity mantle, may dominate the present-day bedrock uplift.

This study investigates deficiencies in millennial-scale GIA models arising from omission of Late Holocene and present-day ice-mass changes. In the Antarctic Peninsula increasing accumulation observed in ice cores since the 1850s has been shown to cause loading and present-day GIA-related subsidence, although results are dependent on the Earth model. This missing signal may help to reconcile the misfit between GIA model predictions and GPS-observed uplift.

GPS records from the northern Peninsula provide an opportunity to place bounds on the regional Earth properties. Since 1995 several ice shelves have collapsed triggering ice-mass unloading that invokes a solid Earth response. However, non-linear GPS-observed uplift cannot be explained by elastic deformation alone. Using a viscoelastic model to predict uplift due to recent ice loss and testing the fit to GPS time series, an Earth model has been constrained with upper mantle viscosity much lower than previously suggested.

Elsewhere, the stagnation of Kamb Ice Stream on the Siple Coast ~165 years ago has caused localised thickening of ice which may cause significant GIA-related subsidence if the regional mantle viscosity is low. Combining with an LGM deglacial history and comparing with an empirically-derived GIA model shows large misfits, indicating that the regional mantle viscosity is high and highlighting potential errors in the LGM deglacial model.

Acknowledgements

This research was funded by a NERC PhD studentship. I would like to thank my supervisors Professor Matt King, Professor Peter Clarke and Dr Pippa Whitehouse for the endless support and encouragement over the past few years. Thanks to Professor Mike Bentley who also supervised some of the work and provided some very useful discussions.

I would like to acknowledge all those who have assisted me in doing this research by providing data or model codes. First of all, Glenn Milne, Valentina Barletta and Andrea Bordoni who provided the GIA models used in this thesis, and Mark Tamisiea and Martin Wolstencroft who provided additional Earth models for one of the GIA models. Thanks to the many people who have allowed me to use their data in this work, or made data publicly available. These include Eugene Domack, Ted Scambos, Etienne Berthier, Brian Gunter, Michiel van den Broeke, Jan Lenaerts, Elizabeth Thomas, and Hamish Pritchard. I would also like to acknowledge Anne Le Brocq and Stewart Jamieson for valuable advice on Glimmer.

Finally, I would like to acknowledge my colleagues in Civil Engineering and Geosciences at Newcastle University for their support and advice, and all those in the GIA community who have provided interesting and stimulating discussions at the many conferences I have been fortunate enough to attend over the past few years.

Contents

List of Figures

List of Tables

List of Abbreviations

AIS	Antarctic Ice Sheet
A-NET	Antarctic Network
AP	Antarctic Peninsula
APIS	Antarctic Peninsula Ice Sheet
BE	Best estimate
BP	Before present
DEM	Digital Elevation Model
EOF	Empirical orthogonal function
GIA	Glacial isostatic adjustment
GPS	Global Positioning System
GRACE	Gravity Recovery And Climate Experiment
ICESat	Ice, Cloud, and land Elevation Satellite
InSAR	Interferometric Synthetic Aperture Radar
ka	Thousand years
KIS	Kamb Ice Stream
LARISSA	LARsen Ice Shelf System, Antarctica
LB	Lower bound
LGM	Last Glacial Maximum
LVZ	Low viscosity zone
MacIS	MacAyeal Ice Stream
NAP	Northern Antarctic Peninsula
POLENET	The Polar Earth Observing Network
PREM	Preliminary Reference Earth Model
RMS	Root mean square
SIA	Shallow ice approximation
SMB	Surface mass balance
UB	Upper bound
VE-CL0V3RS v1.4	Visco-Elastic Compressible LOVe numbER Solver
VE-HresV2	Visco-Elastic High Resolution technique for Earth deformations
WAIS	West Antarctic Ice Sheet
WIS	Whillans Ice Stream
yr	year

Chapter 1. Introduction

1.1 Background

Glacial isostatic adjustment (GIA) describes the Earth's response to changing ice and water loads as ice sheets grow and diminish. The degree to which the Earth deforms is governed not only by the amount of ice and water loading but also by the internal structure and composition of the Earth. The high viscosity of the Earth's mantle leads to a time-delayed response to surface loading or unloading, meaning uplift of the Earth following the demise of ice sheets from the end of the Last Glacial Maximum (LGM), around 20,000 years ago, can still be observed today. Understanding this process is important because it allows constraints to be placed on former ice-sheet changes and provides a way to 'sample' Earth structure. GIA also causes changes in the shape of the geoid, the Earth's surface of equal gravitational potential that coincides approximately with mean sea level, as internal mass is redistributed in response to surface loading. This can confound satellite gravity measurements of present-day ice-mass change (e.g. from NASA's Gravity Recovery And Climate Experiment, GRACE) and needs to be accurately removed. Changes in the shape of the Earth due to GIA also affect local sea levels. Although ice melt leads to overall sea-level rise, the uplift of the Earth in response to ice unloading, or the change in shape of the geoid, may result in a local sea-level fall. Understanding GIA is therefore critical in order to accurately predict future relative sea-level changes.

GIA at the location of former ice sheets in the Northern Hemisphere is relatively well known. For example, in Fennoscandia several models of ice history produce a good fit to extensive networks of measured uplift (Steffen and Wu, 2011; Lidberg et al., 2007). In contrast, GIA in Antarctica is less well known and there are large differences between the leading models (Thomas et al., 2011). There are several issues which hinder advances in this area. Knowledge of the two main inputs to a GIA model – ice history and Earth parameters – is limited. In particular, the past few thousand years of ice history in Antarctica is not well known (Bentley, 2010). In terms of observational present-day uplift data with which to constrain or validate models of GIA, e.g. Global Positioning System (GPS), Antarctica is lacking compared with other regions such as Greenland (Bevis et al., 2012), although networks have significantly expanded in recent years (Wilson et al., 2011). A further complication when using GPS measurements of

uplift in Antarctica to constrain models of GIA is that they also contain the instantaneous elastic response of the Earth in relation to present-day ice-mass change. This is especially relevant for regions undergoing high rates of present-day ice-mass change such as the Antarctic Peninsula (AP).

The last few thousand years, known as the Late Holocene, is a period of time often neglected in Antarctic GIA models due to the lack of observational constraints. In regions where the Earth has lower than average mantle viscosity, omitting changes in ice-sheet thickness over the past few thousand years may lead to errors in model-predicted rates of present-day GIA. In terms of the structure of the Earth, Antarctica can typically be thought of as having two distinct halves, East Antarctica with a thick cratonic lithosphere and high-viscosity mantle, and West Antarctica with thinner lithosphere and lower mantle viscosity (Morelli and Danesi, 2004). A high mantle viscosity means the Earth responds slowly to changes in surface loading and ice-mass changes over the past few thousand years do not contribute much, if anything, to the present-day signal. Conversely in West Antarctica, where mantle viscosity is lower, the Earth responds much more quickly to changes in surface loading so that present-day GIA is likely to be dominated by recent ice-mass changes rather than LGM ice history. Therefore currently unmodelled Late Holocene ice-mass changes are a potential source of large errors in GIA models of West Antarctica.

The focus of this thesis is to explore the effect of Late Holocene ice-mass changes on GIA in two regions of West Antarctica – the Antarctic Peninsula and the Siple Coast (see Figure 1.1). The Antarctic Peninsula is a region of recent rapid ice change coupled with a low viscosity mantle compared with the rest of Antarctica (Ivins et al., 2011). This means that changes on a decadal to centennial scale may be influencing the present-day GIA signal in this region. Ivins et al. (2000) considered the effect of different loading scenarios over the past 4 ka on present-day uplift in this region and found that results vary significantly. They showed that the pattern and magnitude of uplift resulting from an oscillating (loading-unloading) ice history can be considerably different to that resulting from a continuous deglaciation scenario, and even have the opposite sign. This demonstrates the importance of considering recent ice loading in this region.

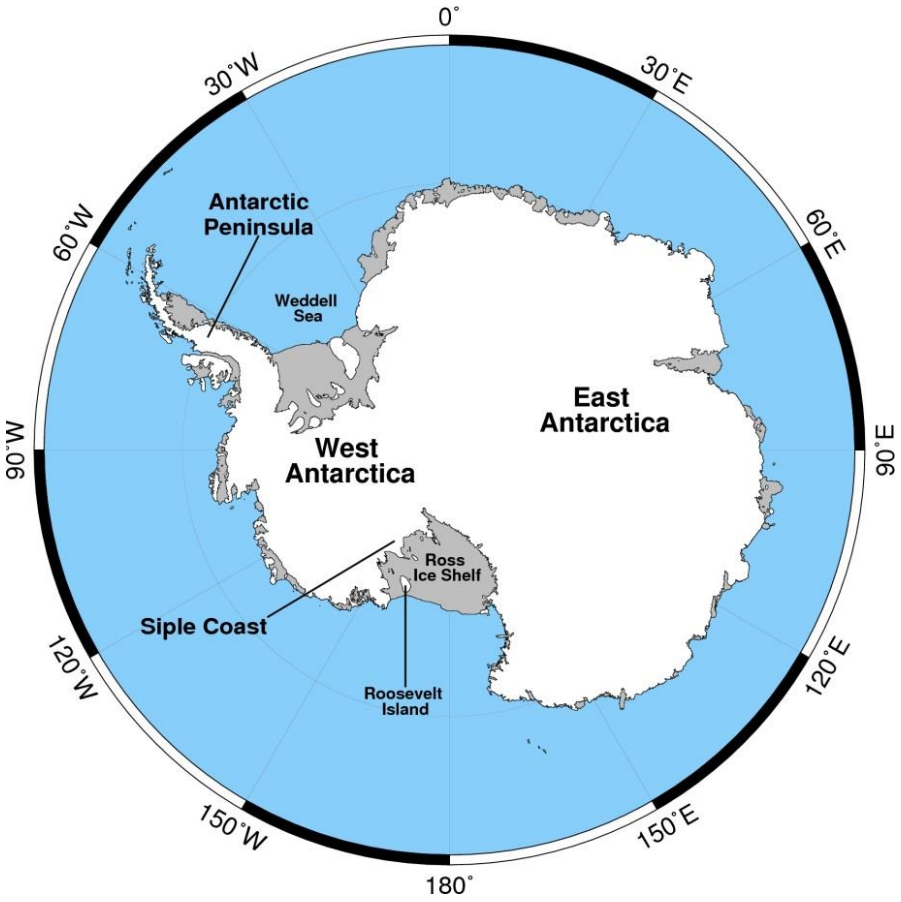

Figure 1.1: Location map showing the two study areas and the main locations discussed in the text.

On the Siple Coast, localised fluctuations in ice-sheet thickness over the past 1000 years have been caused by ice-build up related to stagnation of ice streams. These stagnation and reactivation events occur at different times for different ice streams and are likely to cause localised loading and unloading on a century-scale. These changes in ice-sheet thickness have never before been included in a GIA model.

The following sections provide an overview of the limitations in knowledge of Antarctic ice history as well as a brief description of recent ice history in the two regions that are the subject of this study. Section 1.3 outlines the observations that can be used to constrain models of GIA such as records of past sea-level changes and geodetic observations of present-day deformation. Finally, Section 1.4 details the specific aims of the work carried out for this thesis and Section 1.5 gives an outline of how it is presented.

1.2 Ice History

1.2.1 Antarctic Ice Sheet

Ice history is one of the two key inputs to a GIA model and provides the loading or unloading history with which to force the GIA model and calculate solid Earth deformation and changes in the geoid. The delayed response of the Earth to surface loading means that several thousand years of ice history needs to be taken into account in order to accurately predict present-day GIA rates.

The LGM refers to the maximum global ice extent that was reached during the most recent glacial cycle and is reported to have occurred between 26.5-19 ka before present (BP), or even earlier for the West Antarctic Ice Sheet (WAIS) (Clark et al., 2009). The LGM corresponds to global sea level lowstand with sea levels approximately 120-130 m lower than at present (Peltier, 2004; Yokoyama et al., 2000). The total Antarctic contribution to total sea-level rise since this time is debated and current estimates are in the range 8-17 m (see Figure 2 of Ivins et al. (2013)). An abrupt rise in global sea-level of around 20 m occurred approximately 14.5 ka BP (Meltwater Pulse 1a), as shown in far-field sea-level records (Fairbanks, 1989), and the Antarctic contribution to this is also debated. Glacial geological data suggests only a minor contribution is likely as the available evidence does not support large changes in the ice sheet during this time (Bentley, 2010), although it has been shown that sea-level data do not rule out a dominant Antarctic contribution (Bassett et al., 2007).

It is important to understand how the Antarctic Ice Sheet (AIS) has diminished since the LGM, not only for GIA studies, but also to provide context for recent change and to predict future evolution in response to external forcing (Bentley, 2010). By improving knowledge of the volume of the AIS at the LGM its contribution to global sea-level rise can be constrained further (Bentley, 1999). However, the deglacial history of Antarctica remains poorly understood both in terms of timing and nature of retreat, e.g. progressive thinning or rapid stepped retreat (Bentley, 2010), which may also vary with location.

The ice history of Antarctica can be reconstructed using glacial geological and glaciological data. Marine geophysical and geological data record the locations of past extent of grounded ice on the continental shelf and radiocarbon dating of sediment cores reveals the timing of grounding line retreat. Cosmogenic surface exposure dating of boulders and erratics from around Antarctica can provide the timing of retreat. Ice cores can also provide constraints on ice-sheet thickness and accumulation history. Evidence

such as this can be used to validate numerical models of ice history (e.g. Whitehouse et al., 2012a), which are valuable tools for filling in the gaps where field data are unavailable. The timing of deglaciation in Antarctica is not well known, due to the limited availability of post-LGM timing or thickness constraints compared with other regions (Whitehouse et al., 2012a; Bentley, 1999).

1.2.2 Antarctic Peninsula

Retreat of the Antarctic Peninsula Ice Sheet (APIS) since the LGM is complex. The ice sheet was up to 500 m thicker at the LGM than it is at present (Wright et al., 2008) and formed two domes along the spine of the southern Peninsula that merged with the WAIS in the Weddell Sea (Bentley et al., 2006). There is evidence for early onset of deglaciation between 18 and 9 ka BP which occurred progressively from the outer to the inner shelf and progressively from north to south (Heroy and Anderson, 2007). On the west of the AP, deglaciation was almost complete by the early Holocene but on the east of the AP there is no data to constrain thinning after 7.2 ka BP (Bentley et al., 2006).

Evidence exists for climate fluctuations on the AP during the Holocene. Temperature reconstructions from James Ross Island ice core show an early Holocene warm period between approximately 12 and 9.5 ka BP followed by a stable period between 9.2 and 2.5 ka BP. After 2.5 ka BP a cold period lasted until 600 years ago (Mulvaney et al., 2012). There is evidence that ice shelves around the AP have collapsed in the past coinciding with the fluctuations in temperature. Pudsey and Evans (2001) suggest that Prince Gustav ice shelf collapsed during a period of regional climate warming and was absent between 5 and 2 ka BP, reforming in the cold period that followed. George VI ice shelf also collapsed between 9.6 and 7.9 ka BP following a warm period (Bentley et al., 2005).

Presently, the Antarctic Peninsula is one of the fastest warming regions on Earth and meteorological records show that warming since the 1950s is several times greater than the global average (Vaughan et al., 2003). Rapid changes in climate have led to the retreat and eventual collapse of several major ice shelves, such as Prince Gustav between 1993 and 1995 (Rott et al., 1996), Larsen A in 1995 (Rott et al., 1996), and Wordie Ice Shelf between 1966 and 1989 (Wendt et al., 2010; Rignot et al., 2005). Perhaps the most significant ice-shelf breakup is the collapse of the Larsen B ice shelf in March 2002, where 2300 km^3 of the ice shelf broke up in just one week (Rack and Rott, 2004). A complete summary of ice shelf break-up in the Antarctic Peninsula is

given in Cook and Vaughan (2010). It is widely reported in literature (Rignot et al., 2004; Scambos et al., 2004; De Angelis and Skvarca, 2003) that Antarctic Peninsula glaciers have displayed acceleration and thinning as a result of ice-sheet collapse and are in a state of negative mass balance. Acceleration of glaciers flowing into former ice shelves is widely attributed to the removal of the buttressing effect of their ice shelf (Rignot et al., 2004).

Warmer atmospheric temperatures in the Antarctic Peninsula have also led to an increase in snow accumulation which has been observed in ice cores. The Gomez ice core on the western Peninsula shows that accumulation has doubled since 1850 (Thomas et al., 2008). The spatial pattern of accumulation is complex, however, and increasing accumulation is observed to a lesser extent in other ice cores from around the Peninsula, such as James Ross Island in the north (Thomas et al., 2008), or not at all in the case of Siple Station at the southern end of the Peninsula (Mosley-Thompson, 1992).

1.2.3 Siple Coast

The WAIS is largely a marine based ice sheet and the Siple Coast region contains several large fast-flowing ice streams that drain ice from its interior, feeding the Ross Ice Shelf. Retreat since the LGM in the Ross Sea Embayment took place in the mid-late Holocene from around 12.8 ka BP onwards (Conway et al., 1999). The grounding line had reached the location of the modern day ice shelf by about 7 ka BP (Wright et al., 2008). Retreat then occurred as a swinging gate hinged at the eastern side of the embayment near Roosevelt Island (Figure 1.1) until around 3.2 ka BP, before finally retreating to the present-day grounding line along the Siple Coast (Conway et al., 1999).

Many studies have reported the cycle of stagnation and reactivation of ice streams that has occurred over the past thousand years (e.g. Hulbe et al., 2013; Catania et al., 2012; Hulbe and Fahnestock, 2007). For example, Whillans Ice Stream shut down 850 years ago and restarted 400 years later, and MacAyeal Ice Stream shut down 800 years ago and restarted 250 years later. Catania et al. (2012) provide a complete synthesis of data and timings over the past millennia. The most recent ice stream to shut down was Kamb Ice Stream which rapidly stagnated approximately 165 years ago (Retzlaff and Bentley, 1993). Leading up to its complete stagnation several events occurred that are likely to have contributed to its shutdown. Approximately 350 years ago an area to the north of the ice stream stagnated resulting in narrowing and slowing of the main trunk of Kamb

Ice Stream (Catania et al., 2006), followed 100 years later by the shutdown of an upstream tributary (Catania et al., 2012). Neighbouring Whillans Ice Stream has also been decelerating in the past few decades, slowing by around 23% between 1973 and 1997 (Joughin and Tulaczyk, 2002), and is expected to stagnate in the next 50-150 years (Joughin et al., 2005). A recent study by Beem et al. (2014) showed rates of deceleration increased between 2009 and 2012 to nearly double that of the long-term average rate, suggesting stagnation may happen sooner than previously predicted.

As a result of ice stream stagnation the ice sheet thickens locally as ice continues to flow from upstream but no longer flows out. This has been observed by geodetic techniques. Joughin and Tulaczyk (2002) used measurements of ice flow velocity from InSAR (interferometric synthetic aperture radar) to show a positive mass balance over the region largely due to the stagnation of Kamb Ice Stream, and the continuing deceleration of Whillans Ice Stream. Surface elevation change data from ICESat (Ice, Cloud, and land Elevation Satellite) laser altimetry measurements (Pritchard et al., 2009) shows a present-day thickening of the Kamb Ice Stream of up to 0.65 m/yr, which has been confirmed more recently by CryoSat-2 radar altimetry data (McMillan et al., 2014).

1.3 Observations of GIA

1.3.1 Relative Sea-Level Constraints

Observations of relative sea-level change can be used to constrain GIA models (Whitehouse et al., 2012b; e.g. Bassett et al., 2007). Relative sea-level can be determined from radiocarbon dating of organic material contained in raised beaches, such as shells, bones, and penguin guano. Dating of these kinds of deposits gives a minimum or maximum limit on past sea level. A minimum limit would come from dating of a shell, as it would have been deposited below sea level. A maximum limit would come from samples such as penguin guano, as they would be deposited above sea level. Raised beach deposits such as buried cobbles can also be dated by means of optical stimulated luminescence which determines the time since the cobbles were exposed to light (Simms et al., 2012).

Another common type of relative sea-level observation is lake isolation events. Lake isolation events occur if small basins become cut-off from the sea, indicating a relative sea-level fall. The sediment record will show a change from marine to freshwater environment. Conversely, a change from freshwater to marine environment indicates a

relative sea-level rise. By dating the change in environment within sediment cores from isolated lakes, and measuring the elevation of the sill of the basin above sea level, the mean sea-level at the time of isolation can be estimated (Watcham et al., 2011). Combining data from these different sources allows a relative sea-level curve to be derived for a specific location which can then be compared with GIA model-predicted relative sea-level change. For example, Watcham et al. (2011) compared their relative sea-level curve for the South Shetland Islands with GIA-model predicted sea-level change for three different ice histories.

1.3.2 GPS

The most common geodetic method used for constraining GIA is GPS (King et al., 2010). Installing GPS receivers in Antarctica is limited by the small proportion of ice-free bedrock and the logistical difficulties of installing and powering receivers. However, technological advancements mean that sites can now run through the winter so many of the networks that have been recently installed provide continuous measurements. There are now several networks in operation such as POLENET's A-NET in West Antarctica (http://polenet.org/), and the LARsen Ice Shelf System (LARISSA) network in the Antarctic Peninsula (http://www.hamilton.edu/news/exp/LARISSA/). In addition to this, recent advances in the processing and analysis of GPS data have led to improvements in the accuracy of measurements.

Vertical velocity measurements are most commonly used to constrain GIA, but horizontal velocities can also provide important information regarding the location of ice loading or unloading (Wahr et al., 2013). However, horizontal velocity measurements need to first be corrected for tectonic motion signals, and may be significantly affected by lateral heterogeneities in Earth structure, which complicates their use for constraining GIA models that do not incorporate these lateral variations. Surface velocities measured by GPS may also record uplift due to the immediate elastic response of the Earth in areas where there is significant present-day ice-mass loss, e.g. the Antarctic Peninsula as described in Section 1.2.2. In order to use GPS-observed uplift to constrain GIA models, the elastic signal must first be removed (Thomas et al., 2011).

1.3.3 Other Satellite Data

In addition to relative sea-level constraints and GPS measurements, observations from satellites can be used to derive empirical GIA models, which are not computed from, and are therefore are independent of, past ice-sheet changes and Earth structure. Traditional GIA models can be compared with empirical models to verify results.

This method of deriving GIA uses a combination of satellite gravimetry (GRACE) and satellite altimetry (ICESat) to distinguish between signals caused by GIA and those due to present-day ice-mass change. GRACE measures time-variable gravity change from which total mass change can be derived and ICESat measures surface elevation change and hence volume change can be directly estimated. By combining these signals it is possible to solve for the GIA uplift signal, according to the method outlined in Riva et al. (2009).

Riva et al. (2009) were the first to use this method to infer the GIA signal for Antarctica. Their work was recently updated by Gunter et al. (2014) to include longer data sets with improved processing techniques and to include a firn densification model which allows for differences in density due to firn compaction and surface processes. Gunter et al. (2014) compared their empirically-derived GIA uplift with GPS-observed uplift and found a good agreement between the two data sets, and in most cases a better agreement than traditional GIA models.

Groh et al. (2012) applied this method to estimate GIA-related mass changes and vertical deformation in the Amundsen Sea sector of West Antarctica. They found that their inferred GIA uplift of up to 20 mm/yr, which was verified by campaign GPS data, is significantly greater than GIA model-predicted uplift in this region. Gunter et al. (2014) estimate a GIA uplift of around 6 mm/yr for this region, and whilst much lower than the uplift rate predicted by Groh et al. (2012), is still higher than GIA model-predicted uplift.

Schön et al. (2014) estimated West Antarctic GIA using a similar data-driven method which employs GRACE, ICESat and GPS data, but without the same reliance on models of accumulation and firn densification. They find a different spatial pattern of present-day GIA uplift than Gunter et al. (2014), that is consistently lower in all basins but one (the northern Antarctic Peninsula). Furthermore, in the Amundsen Sea sector they estimate a GIA uplift of close to zero in contrast to the large rates predicted by both Groh et al. (2012) and Gunter et al. (2014).

1.4 Aims

Improving GIA models in Antarctica has important implications for the accurate estimation of the mass balance of the Antarctic Ice Sheet from GRACE gravity data, and for current and future predictions of sea-level rise. Ice-mass changes in the last few thousand years cannot be neglected from GIA models as they will have a dominant effect upon present-day uplift rates in regions of low viscosity mantle, such as West Antarctica (Morelli and Danesi, 2004) and particularly the Antarctic Peninsula (Ivins et al., 2000). Omitting recent ice history from GIA models may lead to errors in the predicted uplift rates and geoid change rates, which in turn may result in inaccuracies in predictions of ice-mass change from GRACE.

The primary aim of this thesis is to investigate deficiencies in millennial-scale GIA models arising from omission of Late Holocene and present-day ice-mass change in the Antarctic Peninsula and Siple Coast regions of West Antarctica. To achieve this aim, three specific problems are addressed.

1. The effect of recent (centennial) ice loading in the Antarctic Peninsula on the present-day GIA uplift signal is investigated. A doubling of accumulation in the south-western Antarctic Peninsula since the 1850s has been recorded in ice cores (e.g. Thomas et al., 2008), and may be significant enough to cause a present-day GIA response.
2. GPS records in the northern Antarctic Peninsula (Thomas et al., 2011) offer a unique opportunity to constrain Earth parameters by capturing velocities before and after the collapse of the Larsen B ice shelf in early 2002. Since this time, glaciers flowing into the Larsen B embayment have experienced increased mass loss, leading to uplift of the solid Earth. Model-predicted uplift in response to a high resolution dataset of ice-mass loss north of 66°S is compared with GPS-observed uplift in order to constrain a regional Earth model.
3. Ice build-up due to the recent stagnation of Kamb Ice Stream and its potential effect on the present-day GIA signal is investigated. This stagnation occurred rapidly approximately 165 years ago (Retzlaff and Bentley, 1993) and a present-day thickening in this region has been observed by ICESat (Pritchard et al., 2009). Furthermore, these recent ice-mass changes are considered in the context of an LGM deglacial history and results are compared with and empirically-derived GIA model.

1.5 Thesis Outline

Chapter 2 of this thesis focuses on the theory of GIA modelling and the main equations used in predicting solid Earth deformation and perturbation of the geoid. The two main inputs to a GIA model – the Earth model and ice history – are also described in more detail. A description of the two GIA models used in this study is given, as well as an outline of the main Antarctic GIA models used to correct GRACE data.

Chapter 3, 4, and 5 detail the work undertaken for each of the aims stated above. The work contained in Chapter 3 and Chapter 4 has been published in Nield et al. (2012) and Nield et al. (2014), respectively, but is described here in detail. Chapter 3 focuses on the recent increase in accumulation observed in ice cores since the 1850s and predicts the GIA response for a range of Earth models. Chapter 4 investigates a smaller region of the Antarctic Peninsula and uses high resolution data of recent ice loss and GPS records to constrain a viscoelastic model of deformation. The Siple Coast is the subject of Chapter 5, where present-day GIA predictions of recent stagnation-related ice thickening on Kamb Ice Stream are made. Ice loading changes related to ice stream stagnation and reactivation over the past 2000 years are then considered in the context of LGM deglaciation and resulting GIA model estimates are compared with an empirical GIA model. Finally, the main conclusions from this work are summarised in Chapter 6 and some suggestions are made for areas of potential future work.

1.6 Contributions to the Thesis

This section describes all the contributions to the work included in this thesis from collaborative researchers. All parts of the work other than those detailed in this section have been undertaken by me. The two GIA models were provided by Glenn Milne, Valentina Barletta and Andrea Bordoni (Section 2.2), along with the input Earth models and Love numbers. Specifically in Chapter 4, the load Love numbers were computed by Andrea Bordoni using VE-CL0V3RS v1.4 (see Section 2.2.2 for more details). The ice-sheet model (Glimmer, Section 2.4.2) is open source and a template input file was provided by Anne Le Brocq based on the modelling described by Le Brocq et al. (2011). This input file controls how the ice-sheet model runs, and was updated for the Antarctic Peninsula and the specific modelling requirements described in Chapter 3. In Chapter 4, GPS time series from seven sites were used to constrain modelling. All of the GPS processing was undertaken by Matt King and is described by Nield et al. (2014)

Many of the datasets used in this work are publically available and cited accordingly in the text. There are some datasets that were provided directly by collaborative researchers and these are described below. The RACMO2.1/ANT SMB dataset (Section 2.4.4) was provided by Michiel van den Broeke and Jan Lenaerts, first for the period January 1989 to May 2010 and then later an updated dataset for the period January 1979 to December 2010 (Lenaerts et al., 2012). Ice core accumulation histories for three of the ice cores used in Chapter 3 (Gomez, Dyer Plateau and James Ross Island) were provided by Elizabeth Thomas. The ice-mass loss data used in Chapter 4 was provided by Ted Scambos and is the ice-loss data described by Scambos et al. (2014), Berthier et al. (2012), Shuman et al. (2011). Finally for Chapter 5, ICESat elevation change data was provided by Hamish Pritchard, and the empirical GIA model used for comparison with model results was provided by Brian Gunter.

Chapter 2. GIA Modelling and Ice-Sheet Modelling

This chapter describes the underlying theory of GIA modelling which is used to calculate solid Earth deformation and geoid perturbation in response to a changing ice load. The two inputs to a GIA model are the ice history, which provides the changing surface load through time, and Earth parameters, which govern how much and how quickly the Earth deforms. As described in the previous chapter, both of these inputs are poorly known in Antarctica. The ice and Earth models are input to the sea-level equation, which calculates solid Earth deformation, geoid perturbation and ultimately relative sea-level change (Section 2.1). The two GIA models that are used in this study are described in Section 2.2. The three main Antarctic GIA models that are most commonly used to correct GRACE data for the GIA signal are reviewed in Section 2.3. Finally, Section 2.4 describes reconstruction of an ice-sheet history for input to a GIA model, including an overview of ice-sheet modelling and a description of the ice-sheet model used in this study.

2.1 Solid Earth Modelling

2.1.1 Sea-Level Equation

The sea-level equation describes the change in relative sea level due to GIA-related processes. Changes in surface loading related to decreasing ice mass and additional water being added to the oceans leads to solid Earth deformation and perturbation of the geoid. Water is redistributed in a gravitationally consistent way, altering relative sea levels due to the rising or falling bedrock elevation and adjustment of the gravity field.

Sea level is defined as the difference between the geoid height and the solid surface at a given location. It follows that *change* in sea level is due to *changes* in geoid height and solid surface height caused by GIA perturbations. The original form of the sea-level equation was presented by Farrell and Clark (1976) for a spherically symmetric, self-gravitating, non-rotating Earth. It has since been updated to include rotational feedback (Mitrovica et al., 2005; Milne and Mitrovica, 1996), which describes how variations in surface mass alter the Earth's rotation, hence deforming the geoid and solid Earth, leading to further mass redistribution. The original equation also neglected the changing area of the ocean as sea level transgresses inland, or falls and migrates towards the ocean, known as shoreline migration (Mitrovica and Milne, 2003).

The sea-level equation in its original form (after equation 2.33 of Spada and Stocchi (2006)) is given by:

$$S(\theta,\lambda,t) = \frac{\rho_i}{\gamma} G_s \otimes_i I \; + \; \frac{\rho_w}{\gamma} G_s \otimes_o S \; - \; \frac{m_i}{\rho_w A_o} \; - \; \frac{\rho_i}{\gamma} \overline{G_s \otimes_i I} \; - \; \frac{\rho_w}{\gamma} \overline{G_s \otimes_o S} \qquad \text{Equation 2.1}$$

In words, the sea-level equation describes relative sea-level changes (S) in space (colatitude θ and longitude λ) and time (t) in response to the ice and ocean loading histories which are also a function of location and time. The first two terms in the equation represent the spatially varying components of sea-level change where the sea-level Green's function (G_s, see Section 2.1.2) is convolved in space and time $(\otimes_i, \otimes_o)$ with the ice load (I) and ocean load (S), respectively. ρ_i and ρ_w are the density of ice and water, respectively, and γ is gravitational acceleration. The third term represents the eustatic component of sea-level rise in which the additional mass of ice (m_i) is divided over the area of the ocean (A_o). The final two terms represent spatially uniform components where the bar represents average over the area of the ocean. The last three terms in the equation ensure mass is conserved. Because the sea-level variation S appears on both sides of the equation it must be solved iteratively.

2.1.2 Green's Functions

The sea-level Green's function, G_s in Equation 2.1, is given by:

$$G_s(\theta',\lambda',t) \equiv G_\Phi - \gamma G_u \qquad \text{Equation 2.2}$$

and represents the offset between the geoid and bedrock topography at a given location θ', λ' relative to the load centre. The Green's functions G_Φ and G_u calculate the gravitational perturbation and vertical deformation of the Earth in response to surface loading and are based on the viscoelastic load Love number theory developed by Peltier (1974). The viscoelastic Green's functions for gravitational potential Φ and vertical deformation u are given (after equation 1.38 of Spada and Stocchi (2006)) by:

$$\begin{Bmatrix} \frac{1}{\gamma} G_\phi \\ G_u \end{Bmatrix} (\theta',t) = \frac{a}{m_e} \sum_{l=0}^{\infty} \begin{Bmatrix} k_l \\ h_l \end{Bmatrix} (t) P_l(cos\theta') \qquad \text{Equation 2.3}$$

This is the sum over harmonic degrees $l = 0$ to infinity of the time-varying Love numbers for gravitational potential k_l and vertical displacement h_l multiplied by the

Legendre polynomial $P_l(cos\theta)$. a is the mean radius of the Earth and m_e is the mass of the Earth.

2.1.3 Love Numbers

The load Love numbers used in the Green's function reflect the structure and rheology of the Earth, one of the two key inputs to a GIA model. Love numbers describe the deformation of the solid Earth and resulting perturbation of the geoid for given Earth properties. A compact form of the viscoelastic Love numbers can be written as (equation 1.37 of Spada and Stocchi (2006)):

$$\begin{Bmatrix} k_l \\ h_l \end{Bmatrix}(t) = \begin{Bmatrix} 1 + k_l^e \\ h_l^e \end{Bmatrix}\delta(t) + \sum_{j=1}^{M} H(t) \begin{Bmatrix} k_{lj} \\ h_{lj} \end{Bmatrix} e^{s_{lj}t} \qquad \text{Equation 2.4}$$

Put simply in words, the load Love numbers k_l and h_l are the sum of the elastic and viscous components multiplied by the loading history. The elastic part contains a local impulsive load (Dirac's delta), $\delta(t)$, which is multiplied by the elastic Love numbers for gravitational potential k_l^e and vertical displacement h_l^e. The viscous response is the sum over the viscoelastic modes M of the viscoelastic Love numbers k_{lj} and h_{lj} multiplied by the Heaviside step function, $H(t)$:

$$H(t) = \begin{cases} 1, & t \geq 0 \\ 0, & t < 0 \end{cases} \qquad \text{Equation 2.5}$$

s_{lj} is defined as $-\frac{1}{T_{lj}}$, where T is the relaxation time of the viscoelastic mode. The number of modes is governed by the stratification of the Earth model. For a full review of viscoelastic normal mode theory, the reader is referred to Peltier (1974).

2.1.4 Earth Models

The structure and composition of the Earth governs how it will respond to changes in surface loading. Knowledge of Earth parameters is limited and can only be inferred rather than measured. Elastic properties and density within the Earth are described by the seismically derived PREM (preliminary reference Earth model) (Dziewonski and Anderson, 1981), a one-dimensional radially stratified model giving average values for layers 20-100 km thick through the Earth. The viscosity structure of the Earth is less well known and for modelling purposes is generally coarsely defined, for example Whitehouse et al. (2012b) and Ivins et al. (2013) derive average viscosity values for

upper and lower mantle layers only, together with the thickness of an elastic lithosphere. The viscoelastic properties govern how much and how quickly the Earth deforms under a load, and the density structure determines the perturbation of the geoid as material of different density moves around.

In addition to the structural properties of the Earth, its modelled response to loading also depends on the rheological model applied. The rheology of the Earth describes how it deforms under stress and there are many rheological models that can be used to describe its response (Ranalli, 1995). The most common rheological model applied to GIA studies is the linear Maxwell model, and is the only model considered in this study. A Maxwell model couples elastic and viscous responses, so that under stress, the immediate elastic response is followed by a linear viscous deformation. When the stress is removed, the elastic strain is recovered but the viscous deformation is not (Ranalli, 1995). Linear Maxwell rheology is not generally regarded as being realistic behaviour for the upper mantle in other studies of the solid Earth, such as post-seismic deformation studies (e.g. Kogan et al., 2013; Freed et al., 2006; Pollitz, 2005). However, the GIA modelling community continue to use it in the absence of data relevant to GIA that shows the need for a more complex rheological model. This point is discussed further in Chapter 4.

Historically, due to the complexities involved in GIA modelling, the Earth models used are generally globally averaged one-dimensional approximations, that is, properties only vary in the radial direction and not laterally. Since 1-D Earth models represent a simplification of Earth structure it is highly likely that parameters in some regions will vary greatly from the global average, for example, Iceland tends to have a thinner lithosphere and lower viscosity mantle (Auriac et al., 2013). Modelling these regions with a globally averaged 1-D Earth model can therefore lead to errors. Implementing 3-D Earth models in GIA modelling is computationally expensive and limited by knowledge of 3-D parameters, although this is an emerging field of research (e.g. A et al., 2013).

2.2 GIA Model Codes

Two GIA models have been used in this study. The first was provided by Glenn Milne (University of Ottawa) and used for the work described in Chapter 3 and Chapter 5. It is capable of modelling large scale ice changes over long time periods, for example modelling global deglaciation from LGM to present-day, thus it was suitable for

modelling the larger regions of the AP and Siple Coast. The second GIA model, "VE-HresV2", was provided by Valentina Barletta (DTU Space) and used for the work described in Chapter 4. This model is only suitable for modelling small load changes over small areas such as the northern AP. The models are described in the following sections.

2.2.1 GIA Model 1: Milne

This GIA code was developed by Glenn Milne, currently at the University of Ottawa, and although it is not publically available, it has been used in numerous studies (e.g. Bradley et al., 2011; Simpson et al., 2011). The numerical algorithm employed by the GIA code is described in detail by Kendall et al. (2005) and follows the theory outlined in Section 2.1. The global sea-level equation is solved so that deformation due to changes in ocean loading in response to ice-mass change is included. The model also includes rotational feedback (Mitrovica et al., 2005) and shoreline migration (Mitrovica and Milne, 2003).

The model is capable of computations at maximum spherical harmonic degrees 256, 512 and 1024, equivalent to a spatial resolution of 78, 39, and 19 km, respectively; although at the higher degrees this is limited by the availability of pre-defined Earth models at these resolutions. In this model, the Earth is represented by a spherically symmetric, self-gravitating Maxwell body comprising three layers; an elastic lithosphere, and a uniform viscosity upper and lower mantle extending to 660 km and 2900 km depths, respectively. Below this is an inviscid core. The range of possible parameters for the Earth models at different degrees is given in Table 2.1. The majority of the Earth models were provided with the code, with an additional Earth model provided by Mark Tamisiea (National Oceanography Centre). The elastic and density structure of the Earth is derived from PREM (Dziewonski and Anderson, 1981).

In addition to defining the Earth model, the ice history that provides the loading on the Earth also needs to be defined. The ice history for this model is defined in spectral form on a spherical harmonic grid corresponding to the degree at which the model is run. Total ice thickness is defined for various time steps and the code takes the difference in ice thickness between adjacent time steps as the loading history.

Spherical Harmonic Degree	Lithospheric Thickness (km)	Upper Mantle Viscosity ($\times 10^{21}$ Pa s)	Lower Mantle Viscosity ($\times 10^{21}$ Pa s)
256	46 71, 96, 120	0.05, 0.3 0.05, 0.08, 0.1, 0.2, 0.3, 0.5, 0.8, 1, 2, 3, 5	10 1, 2, 3, 5, 8, 10, 20, 30, 50
512	46 71 96	0.3 0.1, 0.3 0.5	10
1024	96	0.5	10

Table 2.1: Range of Earth models available.

2.2.2 GIA Model 2: VE-HresV2

The second model used in this study is VE-HresV2 (Visco-Elastic High Resolution technique for Earth deformations) developed by Valentina Barletta and Andrea Bordoni (Barletta and Bordoni, in prep.; Barletta et al., 2006). The software computes elastic and viscous vertical deformation (separately) for a compressible, spherically symmetric, self-gravitating Earth in response to surface loading, but does not solve the full sea-level equation. As such, it is best suited to regional loading studies with load changes that are small enough to produce only small perturbations to Earth's rotation or far-field shorelines.

The ice history is specified as a series of discs, where discs have an assigned value of ice loss (negative values) or gain (positive values). Discs can be any size greater than zero, but typically have a radius in the range 0.5 - 5 km. Loads are treated as a series of point loads at the centre of the discs and Green's functions are spatially convolved with the ice loading discs according to the methods presented in Barletta et al. (2006). Deformation at a given location is computed in one of two ways depending on the distance of the location from the disc. At distances from the load centre of less than 3 times the disc radius, a highly accurate solution is computed using the assumption that at high harmonic degrees the Love numbers are asymptotic. At distances from the load centre of greater than 3 times the disc radius, an approximate solution is computed. Barletta et al. (2006) show that at far field distances (i.e. greater than 3 times the disc radius) the two solutions converge, for discs with radius 1-5 km, and the software is therefore capable of efficiently computing to high harmonic degrees.

Elastic load Love numbers, based on the PREM Earth structure (Dziewonski and Anderson, 1981), are computed up to a specified maximum spherical harmonic degree

using VE-CL0V3RS v1.4 (Visco-Elastic Compressible LOVe numbER Solver) (Barletta and Bordoni, in prep.). The elastic Love numbers become asymptotic to a non-zero value at high harmonic degrees. Above the maximum degree it is assumed that the Love numbers are the same as the asymptotic value (Barletta et al., 2006). The viscous Love numbers rapidly tend to zero for increasing harmonic degrees so that at high degrees the combined Green's function is negligible (Le Meur and Hindmarsh, 2000). The viscous Love numbers tend to zero much faster than the elastic Love numbers tend to a non-zero value and therefore can be truncated at lower degrees. The maximum harmonic degrees for the elastic and viscous models are chosen so that the results do not suffer from effects of truncation and all response is captured at lower degrees.

By making use of these assumptions the software is capable of computing deformation to a very high spherical harmonic degree and so the resolution is only limited by the resolution of the loading discs (Barletta et al., 2006). The software is therefore suitable for a small regional study which requires high resolution modelling, such as the northern Antarctic Peninsula.

2.3 Recent GIA Models

Studies of GIA cover a multitude of geographical regions and timescales, but here the discussion is limited to the three models most relevant to this study, ICE-5G/ICE-6G, IJ05_R2 and W12a, which are commonly used to remove the Antarctic GIA signal from GRACE data (Shepherd et al., 2012).

2.3.1 ICE-5G/ICE-6G

ICE-5G is a global model of deglaciation since the LGM that, when combined with the accompanying Earth model VM2, gives values of uplift and geoid change (Peltier, 2004). The ICE-5G model has recently been updated to ICE-6G, with accompanying Earth model VM5a, although at the time of writing only the Antarctic component of ICE-6G has been published (Argus et al., 2014). The ICE-6G model was developed by adjusting the Antarctic ice loading history in the ICE-5G deglacial model so that the resulting uplift predictions fit GPS-observed uplift from 59 sites around Antarctica. The model was refined iteratively so that the ice history also fit the 62 ice thickness constraints used by Whitehouse et al. (2012a). Both the ICE-5G and ICE-6G deglacial models do not contain any ice thickness changes in Antarctica over the past 4000 years

(see Figure 2 in Argus et al. (2014)). The total post-LGM Antarctic contribution to sea-level rise from ICE-5G is 17.5 m, which has been revised down to 13.6 m in ICE-6G.

The new Earth model, VM5a (Peltier and Drummond, 2008), is a 5 layer approximation of the more complex VM2 model with the introduction of an additional layer below the lithosphere. The Earth model is one-dimensional and takes elastic properties from PREM (Dziewonski and Anderson, 1981). VM5a has a purely elastic 60 km lithosphere above a 40 km high viscosity (10×10^{21} Pa s) layer. The mantle in the earlier VM2 model is stratified into many layers with a viscosity value assigned to each layer, whereas the VM5a model has an average viscosity assigned to a single upper mantle layer and two lower mantle layers (see Figure 3 of Argus et al. (2014) for comparison of Earth models).

Using ICE-5G to correct the GIA signal from GRACE data results in an ice-mass change of -160 ± 34 Gt/yr (Shepherd et al., 2012) over the period January 2003-December 2010, although as yet it is unknown how this may change with the application of ICE-6G.

2.3.2 W12/W12a

Whitehouse et al. (2012a) created a deglacial history for Antarctica that was tuned to fit glaciological and geological evidence of past ice extent. By reconstructing the ice-sheet history with an ice-sheet model, flow dynamics were taken into account thereby making it physically realistic, in contrast to many other ice loading models that omit flow dynamics. The W12 model consists of 5 time slices from 20 ka to present day, and ice thickness was linearly interpolated between time slices for input into a GIA model, although there are no ice thickness changes after 2 ka BP.

Whitehouse et al. (2012b) used this Antarctic ice history, along with the non-Antarctic part of ICE-5G, to run a GIA model. By comparing model-predicted sea-level change with relative sea-level observations around Antarctica they determined the Earth model that provided minimum misfit to the data. The authors then tested the fit of model-predicted present-day uplift against GPS-observed uplift, which had been corrected for elastic effects of contemporary ice-mass loss, to verify the results. When compared with GPS-observed uplift, the GIA model combined with the W12 deglaciation history tends to over-predict uplift throughout West Antarctica, particularly in the Antarctic Peninsula. The authors improved upon this by adjusting the Late Holocene ice history in

the Antarctic Peninsula to reflect ice core accumulation records. Adding an arbitrary uniform thickness of ice during the last 1000 years of the model run reduced the model-predicted uplift rates and improved the fit to GPS-observed rates (see Figure 2.1). The adjusted deglacial history is called W12a. The need for this Late Holocene adjustment highlights the importance of recent ice-mass change in this region, and as suggested by Ivins et al. (2000) the effect of this on present-day uplift in the Antarctic Peninsula is non-negligible.

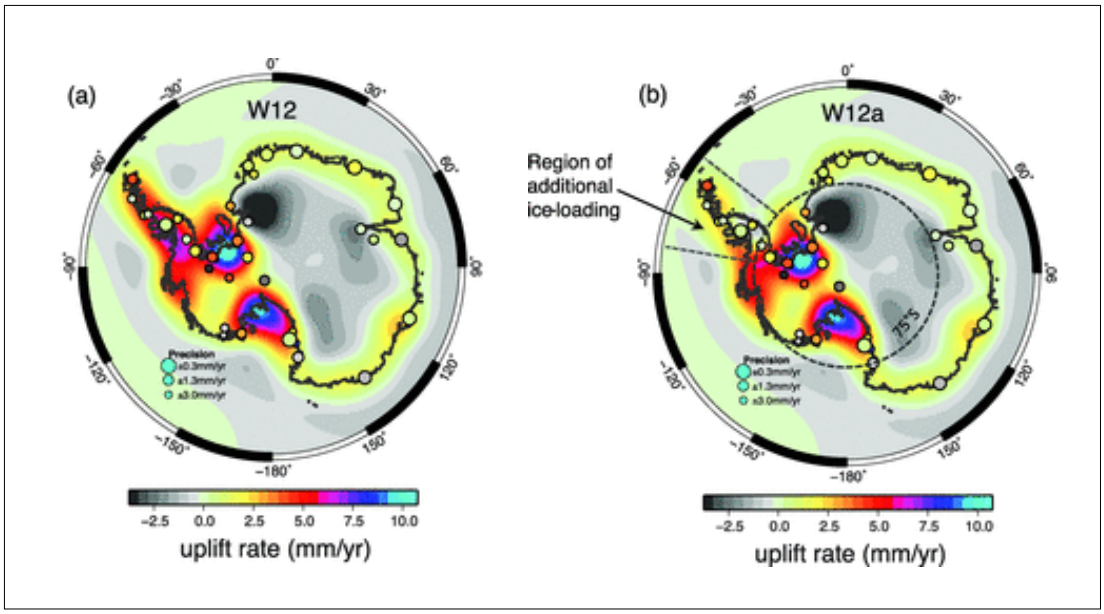

Figure 2.1: Model-predicted uplift rates for (a) the W12 deglacial model and (b) the W12a deglacial model. Circles are elastic corrected GPS rates from Thomas et al. (2011). Figure adapted from Whitehouse et al. (2012b) Figure 10.

Another interesting feature of the W12a model is the large amount of uplift in the Ross Sea, which at 10 mm/yr is the maximum uplift predicted by this model. However, there are no GPS sites located within the high uplift area to verify this result. King et al. (2012a) showed that applying the W12a model to GRACE data over the Ross Ice Shelf resulted in a large surface mass loss of 13 Gt/yr, equivalent to a sea-level fall of 27 mm/yr. This is contrary to an expected mass change of close to zero – as the ice shelf is in hydrostatic equilibrium – and a nearby tide gauge indicates a sea-level change close to zero. King et al. (2012a) therefore concluded that the GIA model was over-predicting uplift, and to obtain the expected mass change of around zero from GRACE data the GIA signal averaged over the entire shelf should be close to zero.

In total, the W12a GIA model predicts a post-LGM Antarctic contribution to sea-level rise of 8 m, much less than that predicted by either ICE-5G or ICE-6G. Applying the W12a GIA model to GRACE data King et al. (2012a) found an estimated ice-mass

change of -69 ± 18 Gt/yr over the period August 2002-December 2010, less than half that of ICE-5G between January 2003 and December 2010.

2.3.3 IJ05_R2

Ivins et al. (2013) produced an Antarctic deglacial history (IJ05_R2) from LGM to present-day, using all available glacial-geological evidence, such as grounding line position data, moraine positions, and rock exposure dating as well as accumulation data from ice cores. This was a modified version of the earlier IJ05 model (Ivins and James, 2005) and incorporated data published after 2005. The data used in IJ05_R2 is largely the same as that included in W12a. The model consists of 10 time slices between LGM and present-day, with linear extrapolation between the time slices, and no changes in ice thickness in the last 2000 years. Whilst they incorporate all observational data of deglaciation, their deglacial history is based on a set of 455 discs that satisfy the observations but do not take into account flow dynamics (see also Section 2.4).

The IJ05_R2 ice history was used to run a model of GIA and output was compared with observed uplift at 18 GPS sites from around Antarctica. They tested the predictions of 240 Earth models and determined two Earth models that can reproduce the GPS uplift well, one with a lithospheric thickness consistent with West Antarctica and the other with a lithospheric thickness consistent with East Antarctica, although both models have the same upper mantle viscosity. When used to correct GRACE data the resulting estimate of Antarctic mass balance is -57 ±34 Gt/yr over the period January 2003 to January 2012, and the Antarctic contribution to sea-level rise since the LGM from this model is 7.5 m, results that are similar to the W12a model.

2.3.4 Comparison of the Models

Although all three Antarctic GIA models described above use largely the same ice thickness constraints and GPS uplift constraints (ICE-5G/ICE-6G, IJ05_R2, and W12a Antarctic Peninsula only), the differences in the methods used result in several key differences in the results. First, the total amount of ice loss from Antarctica over the past 20 ka differs between the models. ICE-6G contributes 13.6 m to global sea-level rise, and whilst this is less than the previous estimate from ICE-5G, still remains >5 m more than either W12a (8 m) or IJ05_R2 (7.5 m) (see Figure 2 of Ivins et al. (2013), and Figure 2 of Argus et al. (2014)). The recent study of Gomez et al. (2013), that uses a

coupled ice-sheet - sea-level model, supports these lower estimates, with estimates of less than 10 m for all model perturbations (Figure 2 of Gomez et al. (2013)).

Second, the models also differ in the manner in which deglaciation occurs. W12a has a smooth and gradual profile of deglaciation/sea-level rise since 20 ka, whereas ICE-5G/ICE-6G contains a stepped approach with large ice losses corresponding to a rapid sea-level rise event at 11.5 ka (Meltwater Pulse 1b (Fairbanks, 1989)). ICE-6G also contains a stepped sea-level rise at ~14.5 ka which corresponds to an earlier sea-level rise event (Meltwater Pulse 1a (Fairbanks, 1989)). IJ05_R2 contains large rapid deglaciation in the past 7 ka and is similar to ICE-5G over this period (see Figure 2 of Argus et al. (2014) for a comparison of the deglaciation from different models).

Finally, the preferred Earth model for each study is different. Both W12a and IJ05_R2 generate an ice loading history independently of an Earth model, and then determine the Earth model that best fits the relative sea-level data (W12a) and GPS-observed uplift data (IJ05_R2) based on the fixed ice history. Conversely, Argus et al. (2014) use a fixed Earth model (VM5a) and alter the ice thickness to produce uplift that matches with GPS observations, whilst ensuring that ice thickness change is also consistent with observations. The upper mantle viscosity for VM5a (0.5×10^{21} Pa s) is only half that of W12a (1×10^{21} Pa s), but more than twice that of IJ05_R2 (0.2×10^{21} Pa s for both models derived).

The magnitude and spatial pattern of present-day uplift predicted by the three models is significantly different (see Figure 2 of King (2013)). In East Antarctica, W12a predicts a large amount of subsidence (up to 2 mm/yr) across much of the interior in contrast to IJ05_R2 that predicts less than 1 mm/yr subsidence over a much smaller area. ICE-5G/ICE-6G predict uplift across much of East Antarctica. In West Antarctica, large uplift centres are present in similar locations in both W12a and ICE-5G/ICE-6G but demonstrate different magnitudes. W12a predicts around 10 mm/yr uplift for two uplift centres in the Ross Sea and Weddell Sea, whereas ICE-6G predicts slightly higher values of 11 mm/yr in the Ross Sea and 13 mm/yr in the Weddell Sea. IJ05_R2 predicts much lower uplift across the whole of West Antarctica of around 2-3 mm/yr with a maximum uplift of 5 mm/yr over the southern Antarctic Peninsula. When applied to GRACE data, the three GIA models result in different estimates of Antarctic ice-mass change. The W12a and IJ05_R2 models produce similar values of -69 ± 18 Gt/yr and -57 ±34 Gt/yr, respectively, whilst applying the ICE-5G model results in a much larger

ice-mass loss of -160 ± 34 Gt/yr. Additional constraints are clearly required to further improve models of GIA.

2.4 Ice-Sheet Reconstruction

Ice-sheet reconstructions form the basis of ice loading histories that are input to GIA models. The requirements for an ice model depend on the GIA model used, but in general tend to be in the form of loading discs, where the height of a given disc is the change in ice thickness over a specified time period and across a specific region. The size of the discs used represents the resolution. Alternatively, ice loading change may be interpolated onto a spherical harmonic degree grid at the resolution of the GIA model.

The simplest type of model does not include consideration of physics related to ice flow. They are derived directly from observations of ice history, where records of ice thickness and/or extent are used to construct a set of loading discs. The limitation of not including ice-sheet physics is that models may not provide a realistic ice history in regions where few observational constraints exist. However, no knowledge of palaeo-climate or other datasets is needed and hence this kind of model provides a simple way of reproducing an ice history for input into a GIA model. This simple method of reconstructing an ice loading history was used in the work described in Chapters 4 and 5 of this thesis.

Ivins et al. (2011) used this approach to model ice loss in the Antarctic Peninsula from the mid-Holocene to present-day. They used one cap, or disc, for each glacier. The radius of each disc remained constant with time, between 5.5 and 50 km, whereas the height of the disc changed with time, according to how much ice mass was being lost from the glacier. Similarly, in their Antarctic GIA model IJ05_R2, described in Section 2.3.3, Ivins et al. (2013) used 455 spherical caps of varying size to represent ice height change from observations.

The recent ICE-6G ice loading history (Argus et al., 2014), described in Section 2.3.1, was also constructed using this approach. Ice thickness was adjusted iteratively to satisfy observational constraints and then the ice-thickness changes were smoothed onto a spherical harmonic grid. The authors unconvincingly argue that attempting to include ice-sheet dynamics into an ice loading model would inappropriately restrict the possible deglaciation histories that can be derived from observations.

In contrast to the simple models described above, ice-sheet models take account of ice-sheet physics and are an important tool in predicting the response of ice sheets to environmental changes and external forcing, such as rising temperatures. Ice-sheet models can be constrained with geological evidence when reconstructing past ice history, but also provide a valuable tool to fill in the gaps where observational data are lacking. As described in Section 2.3.2, Whitehouse et al. (2012b) successfully used an ice-sheet model to reconstruct Antarctic ice history from LGM to present day. The main limitation of ice-sheet model reconstructions is that detailed knowledge of palaeo-climate and ice-sheet boundary conditions is required in order to set up and run a model, and inevitably assumptions are made where this knowledge is lacking (e.g. Whitehouse et al., 2012a).

When using models to represent complex systems, simplifications and assumptions need to be made in order to make computation feasible. The degree to which computations in an ice-sheet model are simplified depends on factors such as the length of time being simulated (e.g. years to millennia), the scale of the model (e.g. regional or continental) and the grid resolution. The most accurate ice-sheet models solve full stress equations but are very computationally expensive (Kirchner et al., 2011). A common method for reducing computational burden when modelling entire ice sheets, such as the Antarctic Ice Sheet, is to make a shallow ice approximation (SIA), which allows large regions to be modelled over long timescales while still being computationally efficient. The discussion here is limited to describing the shallow ice approximation and the ice-sheet model used in Chapter 3 of this study.

2.4.1 Shallow Ice Approximation

This approximation assumes that the thickness of an ice sheet is very small compared with its horizontal extent, and that the ice surface slope and bedrock slope are both small. Hence it is suitable for modelling the behaviour of large ice sheets such as the Antarctic Ice Sheet. Studies have shown that results using SIA models compare well with results using full equations (Leysinger Vieli and Gudmundsson, 2004), although there is some debate about how capable they are of simulating ice stream behaviour (Whitehouse et al., 2012a; Kirchner et al., 2011). At the grounding line, the SIA does not hold as the surface slopes become large and errors may also be introduced when the ratio between the ice thickness and horizontal extent becomes too large.

The ice sheet is modelled as a slab of uniform thickness which flows under gravity and basal shear stress is the driving stress. The only stresses approximated in this method are the shear stresses in the horizontal plane (see Figure 2.2), all other stresses are neglected (Greve and Blatter, 2009).

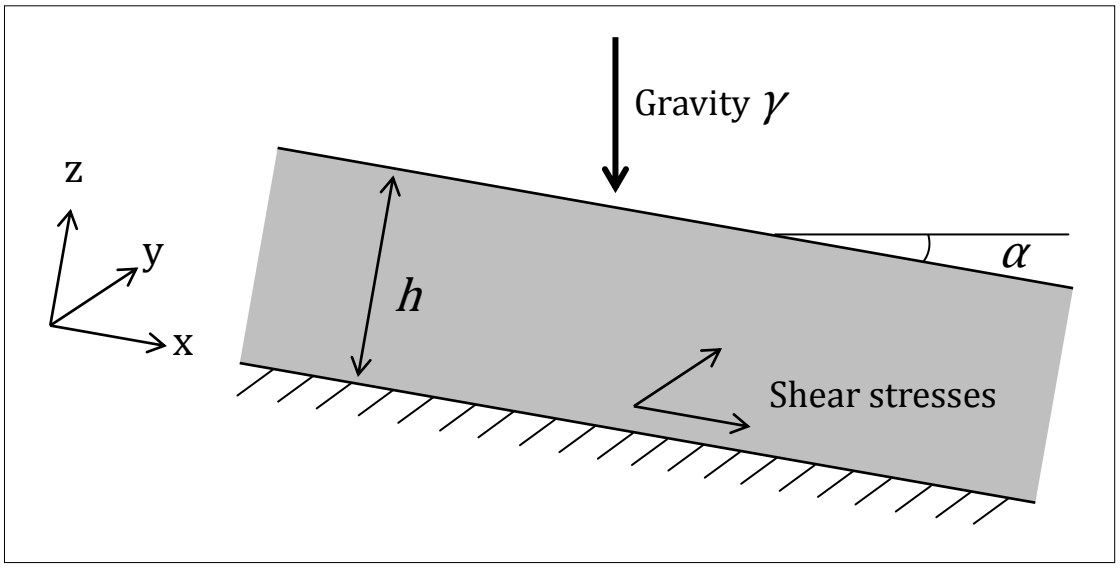

Figure 2.2: Gravity driven ice sheet, with shear stresses in the horizontal plane (adapted from Figure 3.11 of Greve and Blatter (2009)).

The basal shear stress is approximated by (Benn and Evans, 1998):

$$\tau_b = \rho_i \gamma h \, sin\alpha \qquad \text{Equation 2.6}$$

Where τ_b is basal shear stress, ρ_i is the density of ice, γ is acceleration due to gravity, h is ice thickness, α is surface slope. $\rho_i \gamma h$ is essentially the weight of the ice sheet.

2.4.2 Glimmer

The ice-sheet model used in this study is the Glimmer community ice-sheet model (Rutt et al., 2009), a three dimensional thermomechanical model that uses the SIA as described above. It performs well in benchmarking against several tests, EISMINT-1 (Huybrechts et al., 1996), EISMINT-2 (Payne et al., 2000), and the solutions of Bueler et al. (2005), giving confidence in results output from the model. Glimmer has successfully been used to study the Antarctic Ice Sheet in a number of studies (Whitehouse et al., 2012a; e.g. Le Brocq et al., 2011). The limitations of Glimmer are that it uses simple models of basal hydrology and basal sliding meaning processes such as ice streaming are not accurately represented. It also does not include an ice shelf model so calving at the marine margin is not reproduced. The main limitation that is relevant to this study is the spatial resolution that can be used for modelling. For

modelling the AIS, a maximum resolution of 20 km makes computation time feasible, but by limiting the model domain to smaller regions such as the Antarctic Peninsula this increases to 5 km. The full description and equations solved are outlined in Rutt et al. (2009), and a summary is given below.

Glimmer solves for conservation of mass, conservation of momentum and the diffusion equation. Assuming that ice is incompressible, i.e. the density does not change with time, the conservation of mass is given by:

$$\nabla \cdot \boldsymbol{u} = 0 \qquad \text{Equation 2.7}$$

where $\boldsymbol{u}$ is velocity. Momentum is conserved so that the forces acting on a system equal the rate of change of momentum within a system. How the ice flows under gravity depends on the bedrock topography and the rheology of the ice, as described by Glen's flow law (the constitutive equation for ice). Glen's flow law relates stress to strain rate ε in ice and can be written as (Benn and Evans, 1998):

$$\varepsilon = A\tau^n \qquad \text{Equation 2.8}$$

where τ is shear stress, and A and n are constants. The flow law coefficient A depends on temperature as warm ice deforms more easily than cold ice. Glimmer solves the diffusion equation to determine the temperature distribution through the ice sheet to feed into this equation. The flow law exponent n is usually taken to be 3 (Rutt et al., 2009). Strain rates within the ice are thus calculated (see also Equation 5 of Rutt et al. (2009)). Glimmer calculates changes in ice-sheet thickness and flow according to the initial and boundary conditions of the system, as described in Section 2.4.3.

For use in this study, Glimmer has been slightly modified by altering how the sliding velocity is calculated, as described by Le Brocq et al. (2011). This modification allows velocity to be adjusted based on whether the bed is above or below sea level. Below sea level, marine sediments are soft and deform more easily resulting in faster flowing ice than above sea level where the bed is much harder. The use of a hard bed sliding parameter below sea level results in errors in the shape of the ice-sheet surface.

2.4.3 Glimmer Input

To set up a model of the Antarctic Ice Sheet in Glimmer, bedrock topography and initial ice thickness are required, along with boundary conditions from three sources: 1)

climate forcing (surface temperature and mass balance), 2) isostasy, which is a basic model of solid Earth deformation to the changing ice load and hence provides the bedrock elevation, and 3) geothermal heat flux, which provides heat to the lower surface.

Temperature is specified at the top (surface temperature) and bottom (geothermal heat flux) of the ice and the temperature distribution through the ice is calculated using the diffusion equation. Changes in ice surface elevation may also cause changes in surface temperature and these are taken into account through an altitudinal lapse rate describing the change in temperature with elevation. The mass balance model adopted (see Section 2.4.4) defines the flux of additional mass into the system which may further alter ice-sheet thickness and flow.

Isostatic rebound may affect the gradient of the bedrock slope, and also the height of the ice-sheet surface and in turn the temperature at the surface. Glimmer can model four simple approximations of isostasy following the approach of Le Meur and Huybrechts (1996). The lithosphere can either be a "local lithosphere" where flexural rigidity is ignored, or an "elastic lithosphere" which includes flexural rigidity. Implementing the elastic lithosphere model affects only the geometry of the deformation. The asthenosphere can be treated as "fluid" where isostatic equilibrium is reached instantaneously, or "relaxing" where it relaxes like a viscous fluid. The timescale over which the asthenosphere relaxes is specified by the user. In this study the combination of elastic lithosphere and relaxing asthenosphere was used with a relaxation time of between 1000 and 3000 years.

Geothermal heat flux provides the lower boundary condition and describes heat flux from the bedrock into the lower ice surface. If the temperature of the ice at the lower surface reaches the pressure melting point, any excess heat provided by the geothermal heat flux is used to calculate a melt rate. If the ice is frozen to the bed, the heat flux at the surface of the bedrock is the same as the heat flux at the base of the ice while if there is no ice present, the bedrock temperature is set to be the same as the surface temperature.

For Antarctica there are two datasets of geothermal heat flux that are commonly used, that of Shapiro and Ritzwoller (2004), which uses a global seismic model to extrapolate heat-flow measurements, and that of Fox Maule et al. (2005), which is derived from satellite magnetic data. The two datasets have a different spatial pattern of geothermal

heat flux as they have been derived from different methods. Both of these datasets are included in ALBMAPv1 (Le Brocq et al., 2010), a collection of Antarctic datasets. A constant value of geothermal heat flux may also be used, which is suitable for smaller, regional ice-sheet models; for example Le Brocq et al. (2011) used 70 mW/m^2 for their ice-sheet model of the Weddell Sea embayment.

2.4.4 Surface Mass Balance Model

Surface mass balance (SMB) is the net balance between surface processes of accumulation and ablation, and represents mass input to an ice sheet. Measurements and observations of SMB come from ice and firn cores, snow pits, and stake data (e.g. Turner et al., 2002), although measurements are sparse so climate models are increasingly used to estimate recent SMB. The surface mass balance model used for the work in this thesis is RACMO2.1/ANT (Lenaerts et al., 2012), a regional atmospheric climate model of the Antarctic Ice Sheet at 27 km resolution. The modelled SMB includes mass gain from precipitation, and mass loss from sublimation, meltwater runoff, as well as drifting snow erosion. The model SMB values were compared against 745 in-situ SMB observations from around Antarctica and shows that the model performs well with a correlation coefficient of R=0.88.

2.5 Summary

This chapter has outlined the main theory of GIA modelling and the equations used by many GIA models. By solving the sea-level equation, the full system of GIA related processes and feedbacks and their effect on relative sea level can be estimated for a given ice loading history and Earth structure. For small regional loads, vertical deformation and geoid perturbation may still be solved for by just computing Green's functions, as the perturbations to Earth's rotation or far-field shorelines are small.

The two GIA models used in this thesis have been described in Section 2.2. The first solves the full sea-level equation and is suitable for large scale surface load changes where a present-day elastic response is not considered. The second, VE-HresV2, is capable of modelling elastic and viscous deformation at very high resolutions and is suitable for modelling regional deformation where high resolution observations of ice-mass change exist.

The three main Antarctic GIA models have been described in Section 2.3. Comparison of these models shows large differences in the deglacial histories as well as the Earth

models, which result in large differences in the magnitude and spatial pattern of uplift. The main limitation of these models is that they neglect ice-mass changes over the past 2 ka (W12a and IJ05_R2) to 4 ka BP (ICE-5G/ICE-6G), and do not capture recent changes such as those in the Antarctic Peninsula and Siple Coast (Section 1.2). In regions of high mantle viscosity, such as East Antarctica, ice-mass changes over the past few thousand years will not significantly affect the present-day GIA signal. However, in West Antarctica where the mantle viscosity is considered to be much lower, these recent changes may dominate the present-day GIA uplift and therefore cannot be neglected.

The W12a model highlights the potential misfits caused by neglecting Late Holocene ice-mass changes in the Antarctic Peninsula (Figure 2.1), an issue which is investigated in Chapter 3. As the Earth structure and particularly the upper mantle viscosity, remains uncertain, Chapter 4 seeks to place bounds on the likely Earth parameters in the northern Antarctic Peninsula by using GPS-observed uplift since 1998 and a high resolution dataset of ice-mass loss. In the Siple Coast region, it has been shown that the W12a model over-predicts uplift where there are few GPS observations to provide constraints. King et al. (2012a) used GRACE data in this region to suggest the GIA signal should be close to zero. Perturbations to the present-day GIA signal due to loading and unloading over the past 1-2 ka BP is investigated in Chapter 5.

Finally, Section 2.4 outlined the methods used in reconstructing an ice loading history for input to a GIA model. Simple models based on ice thickness change observations provide an effective way to represent ice loading changes for the purposes of GIA modelling, although the lack of ice flow physics is a limitation. The use of dynamic ice-sheet models may provide more realistic ice loading histories and they are able to make predictions where data are lacking, however, they require knowledge of palaeo-climate and ice-sheet boundary conditions in order to set up and run the model. Both methods are used in the work in the following Chapters.

Chapter 3. Accumulation Increase in the Antarctic Peninsula since the 1850s

3.1 Introduction

As discussed in Chapter 1, it is important to consider recent ice-mass changes in regions of possible or known weak Earth structure, such as the Antarctic Peninsula, as they have the potential to contribute substantially to the present-day GIA signal. Global or continent-wide GIA models may not correctly reproduce the present-day signal in these regions when using a 1-D Earth model with a high mantle viscosity.

The recent Antarctic GIA model of Whitehouse et al. (2012b) found an over-estimation of present-day GIA uplift in the Antarctic Peninsula when compared with GPS observations. This mismatch was improved upon by adding a uniform thickness of ice during the last 1000 years of modelling, where changes in ice thickness were otherwise zero in the 2000 years before present. This resulted in lower present-day uplift rates and thus a closer match with GPS observations (Thomas et al., 2011). Similarly, the Antarctic GIA model IJ05_R2 (Ivins et al., 2013) has an ice history that does not include any changes in ice loading in the last 2000 years. The subsequent model-predicted uplift is compared with GPS-observed uplift in order to constrain Earth parameters. Not including recent ice-loading changes could lead to significant errors in model-predicted uplift rates in regions of weak Earth structure, which then cannot be directly compared with GPS observations.

The work described in this chapter investigates the potential GIA signal from a recent (centennial) increase in accumulation in the Antarctic Peninsula as observed in ice core records, a signal which is missing from other Antarctic GIA models. The magnitude of this signal may produce subsidence of sufficient magnitude to counteract uplift due to deglaciation since the LGM, potentially explaining the low rates of present-day uplift observed by GPS (Thomas et al., 2011). Evidence from several ice cores was used to examine the magnitude and spatial pattern of accumulation since 1855. This accumulation history was then used to drive an ice-sheet model to predict the change in ice thickness. The resultant effect of the ice-mass change upon the present-day GIA uplift rates was estimated for a range of Earth models, and the impact on GRACE-derived rates of present-day ice-mass change investigated.

3.2 Accumulation History

3.2.1 Ice Cores

Evidence exists for a significant accumulation increase in the Antarctic Peninsula over the past few decades. The Gomez ice core from Palmer Land demonstrates a doubling of accumulation over the past 150 years (Thomas et al., 2008), and this increase is also seen to a lesser extent in other ice cores (e.g. Dyer Plateau and James Ross Island (Thomas et al., 2008)). This increase in accumulation is not uniform across the region with warmer conditions on the western side resulting in more precipitation than the colder, drier east (Miles et al., 2008).

In this study, accumulation data from five ice cores (Table 3.1) was used to reconstruct an accumulation history for the Antarctic Peninsula. The accumulation time series for Gomez, Dyer Plateau and James Ross Island (Thomas et al., 2008) is presented in Figure 3.1 as a running decadal mean, for Dolleman Island (Peel, 1992) as a 5 year, binomially-weighted average, and for Siple Station (Mosley-Thompson, 1992) a 10 year unweighted average. An error in the published location of the Gomez ice core was identified (originally reported as 73.59°S, 70.36°W (Thomas et al., 2008)) and the correct location is listed in Table 3.1. An updated accumulation time series was used, which includes a field-based strain rate correction (E. Thomas, personal communication, 2012).

Ice Core	Reference	Location (°)		Dates available	Dates used in analysis
		Lon	Lat		
Gomez	(Thomas et al., 2008)	-70.61	-73.99	1854 – 2001	1854 – 2006
James Ross Island	(Thomas et al., 2008; Aristarain et al., 2004)	-57.68	-64.22	1850 – 1992	1854 – 1992
Dyer Plateau	(Thomas et al., 2008; Thompson, 1994)	-64.88	-70.67	1850 – 1984	1854 – 1984
Dolleman Island	(Peel, 1992)	-60.93	-70.58	1794 – 1985	1854 – 1985
Siple Station	(Mosley-Thompson, 1992)	-84.25	-75.92	1505 – 1985	1854 – 1985

Table 3.1: Location and dates of ice cores used in this study.

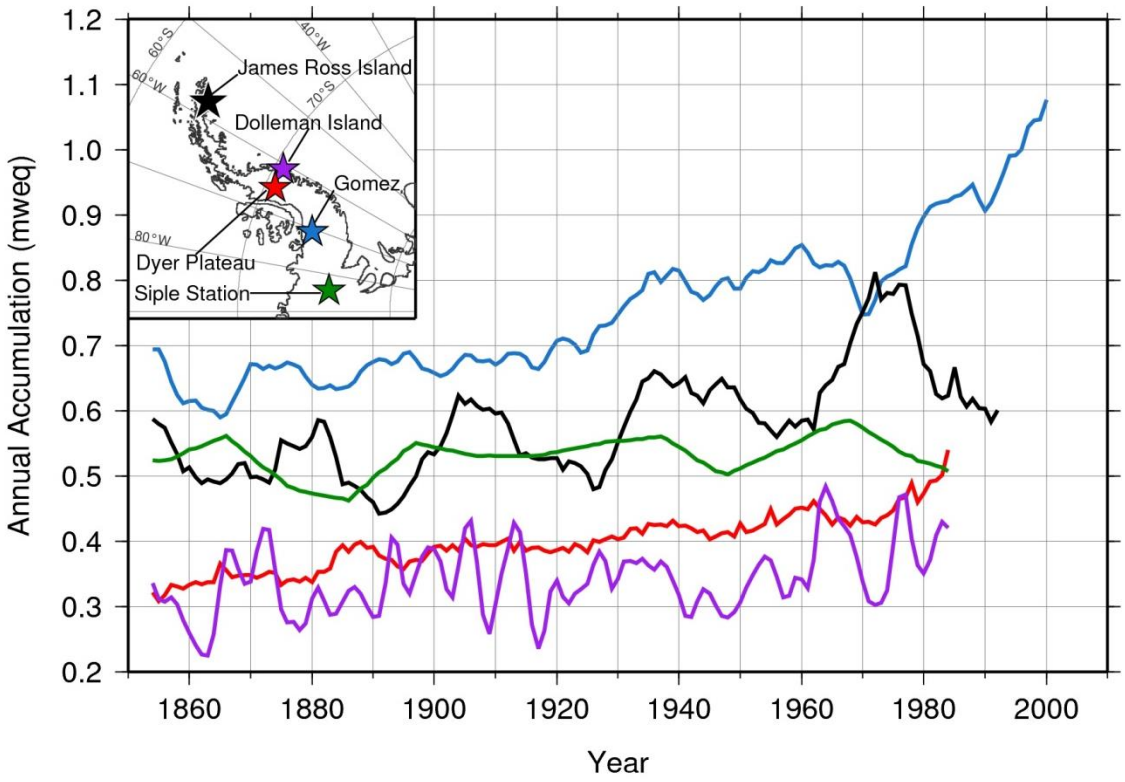

Figure 3.1: Annual accumulation in meters water equivalent (m_{weq}) derived from ice core records: Gomez (blue), James Ross Island (black), Dyer Plateau (red), Siple Station (green), Dolleman Island (purple). Ice core locations are shown in the inset.

3.2.2 Surface Mass Balance Data

In order to reconstruct an accumulation history for the Antarctic Peninsula, the spatial pattern of surface mass balance (SMB) was required. This was taken from a regional atmospheric climate model of the Antarctic Ice Sheet, RACMO2.1/ANT (Lenaerts et al., 2012) (see Section 2.4.4). The modelled SMB includes mass gain from precipitation, and mass loss from sublimation, meltwater runoff, as well as drifting snow erosion. Values of SMB were provided every month from January 1989 to May 2010 on a 27 km grid. The dataset has since been extended to include the period January 1979 to December 2010, although due to the timing of this release, the extended dataset was not used in the analysis described in this chapter.

3.2.3 Empirical Orthogonal Functions (EOFs)

The ice core records presented in Section 3.2.1 show some variability in the magnitude and spatial pattern of increasing accumulation in the Antarctic Peninsula. These records are sparse however, so in order to create an accumulation history for the whole region, an empirical orthogonal function (EOF) technique was used. Empirical orthogonal function analysis is a way of identifying statistical patterns in datasets and is widely

used in climate studies. For example, Miles et al. (2008) used EOFs to determine annual and seasonal accumulation variability on the Antarctic Peninsula to understand the variability in recent climate changes.

EOFs can be used to reconstruct long term data by combining the spatial patterns derived from spatially dense short term data, with long term but relatively sparse observations. Kaplan et al. (2000) used an EOF technique (the reduced space optimal interpolation method (Kaplan et al., 1997)) to estimate the spatial patterns of sea-level pressure anomalies from a dense dataset of observations 1951-1992. They then reconstructed the sea-level pressure anomalies using observations dating back to 1854 in order to compare them with long barometric records at four land stations. There are also several studies that combine altimeter data and tide gauge data to study sea-level rise. Church et al. (2004) estimated EOFs from global satellite altimeter data between January 1993 and December 2001 and then combined them with spatially less dense long term tide gauge data (1950-2000) to estimate sea-level change and regional variability. Calafat and Jorda (2011) apply similar methods to study regional sea-level change in the Mediterranean Sea whilst focussing on quantifying sources of error in the method.

In this study, the spatial patterns (or EOFs) of accumulation were estimated from the relatively short, but spatially dense modelled SMB dataset (Section 3.2.2). By combining these spatial patterns with the ice core data, which covers a much longer time period, an accumulation history for the Antarctic Peninsula was reconstructed.

3.2.4 Method

The method used in this study is the reduced space optimal interpolation method presented in Kaplan et al. (2000) and is the same method followed by Church et al. (2004) and Calafat and Jorda (2011) in the studies described above. The method is summarised below, and all equations have been reproduced from Kaplan et al. (2000).

The first step is to calculate the EOFs for the RACMO2.1/ANT SMB data, which first required some pre-processing. As the model includes data for the whole Antarctic Ice Sheet, a sub set was extracted for the Antarctic Peninsula region (longitude 40°W to 100°W; latitude 60°S to 80°S). This region was selected so that it covered an area slightly larger than the domain of interest. The monthly SMB data were then summed

per calendar year to obtain 21 complete years of annual data 1989-2009. By considering annual SMB, any semi-annual seasonal signals were removed from the data.

The covariance matrix, C, of the modelled SMB data (containing 21 years for 6595 grid points) was found and then the eigenvalues and eigenvectors of the covariance matrix were calculated:

$$C = E\Lambda E^T + E'\Lambda' E'^T \qquad \text{Equation 3.1}$$

where E is a matrix of eigenvectors, and Λ is a matrix of eigenvalues, the prime notation represents omitted values in the reconstruction, and superscript T indicates matrix transposition.

The eigenvectors represent a map (with no time dimension) for each spatial pattern of SMB and are the EOFs. These are ordered according to the size of the eigenvalues with the largest first, and show how much of the variance can be explained by each eigenvector. In other words the first eigenvector, corresponding to the largest eigenvalue, explains the biggest percentage of variability in the SMB data and is termed EOF1. The second is termed EOF2, and explains the second largest spatial pattern in the SMB data, with each subsequent EOF describing a decreasing variance. The largest eigenvalues correspond to large-scale patterns in the data, those that are included in the reconstruction, and the smallest can be considered to be noise, those that are omitted from the reconstruction.

The second step in the method was to reconstruct the data, that is, to project the ice core accumulation records onto the spatial patterns derived from the analysis to get a resulting time series for all grid locations. The EOFs must be truncated to those explaining the largest variance. The largest five EOFs, explaining around 99% of the variance, were used. The large amount of variance explained by the first five EOFs is due to the relatively small region under consideration and the lack of seasonal variations in the data. Commonly, more than 5 EOFs are used in reconstructions, e.g. Church et al. (2004) use 20 and Kaplan et al. (2000) use 80. However, as Calafat and Jorda (2011), who use 4 EOFs, point out, this number is limited by the number of observation points available. As most of the variance is explained by the included EOFs, truncating at 5 is more than sufficient in this case.

For each time step in the ice core data the full grid reconstruction is given by:

$$T = E\psi \quad \text{Equation 3.2}$$

where E is the included first 5 eigenvectors (or EOFs) and ψ is a time series of amplitudes of the EOFs. ψ can be found by minimising the cost function:

$$S[\psi] = (HE\psi - T^0)^T R^{-1}(HE\psi - T^0) + \psi^T \Lambda^{-1}\psi \quad \text{Equation 3.3}$$

where H is the diagonal operator matrix containing ones at grid points where observations are available and zeros otherwise. Each ice core was assigned to a grid cell based on its location. T^0 is a vector of available observations for each time step of the ice core data.

The error is given by:

$$R = \Sigma + HE'\Lambda' E'^T H^T \quad \text{Equation 3.4}$$

where Σ is a diagonal matrix representing the instrumental error, in this case the error on the SMB model data. Although no standard error bounds were given with the RACMO2.1/ANT data, this is set to 100 mm/yr, and sensitivity tests showed varying this value did not make a significant difference to the reconstruction. The second term in the error equation accounts for the omitted EOFs.

Minimising the cost function gives the optimal interpolation solution (Kaplan et al., 2000):

$$\psi = PE^T H^T R^{-1} T^0 \quad \text{Equation 3.5}$$

with:

$$P = (E^T H^T R^{-1} HE + \Lambda^{-1})^{-1} \quad \text{Equation 3.6}$$

When ψ is found for a given time step, T is calculated as per Equation 3.2 and then T is collated for all time steps giving an accumulation time series for each grid point in the domain between 1854 and 2010.

The length of each ice core record varies with some records dating back to ~1500, and all terminating before 2010. As the aim of this study is to examine increase in accumulation since the 1850s, only data after this time (from the start of the Gomez record – 1854) was included in the reconstruction. Sensitivity studies showed that

reconstructing different periods of time with different numbers of EOFs/ice cores led to anomalies in the reconstructed time series. To overcome this, all ice core records were linearly extrapolated beyond their termination to 2010 using the same average rate of change as observed between 1930 and the end of the ice core record. This period was chosen because 1930 marks the onset of annual accumulation increase in the Gomez record (Thomas et al., 2008), and based on the available data it is reasonable to assume that this increase continues beyond the end of the record. As the extrapolation is applied to the end of the ice core records, over a maximum of 15 years for Dyer Plateau and less for the other ice cores, the resulting effect on the subsequently modelled GIA signal is minimal given the limited amount of time over which the mantle would need to respond to produce a present-day signal. To verify this, a sensitivity study was carried out (see Sections 3.3.8 and 3.4.6) by varying the extrapolated rates by ±50%. This results in three variations of the accumulation time history, a best estimate, and lower and upper bounds.

3.2.5 Assumptions and Limitations

The main assumption inherent in this method is that the spatial patterns of accumulation derived from the EOF analysis for the period 1989 – 2009 are stationary throughout the whole period of the reconstruction (1854-2010), i.e. that the covariance remains the same (Calafat and Jordà, 2011). While this may not be the case, the main pattern picked up by the EOF analysis is the east-west divide in precipitation (Figure 3.2), which is due to the mountain chain forming a barrier between east and west (Turner et al., 2002). This east-west divide is therefore likely to be a long term climate regime and consistent for the period of time covering the ice core records.

A limitation of the method is the number of EOFs used in the reconstruction, which is restricted by the number of observation points. However, as ~99% of the variance is explained with the first five EOFs this is not a large source of error. The resolution of the SMB data (27 km) may be a limitation as it is somewhat coarse compared to the steep topography of the Antarctic Peninsula (Cook et al., 2012) and smaller spatial patterns of accumulation may not be picked up. However, the 27 km resolution is an improvement on previous studies such as Miles et al. (2008) who used EOF analysis on model data at 120 km to successfully determine patterns of spatial accumulation variability on the AP. The effect of not picking up the smaller spatial variability of

accumulation on the net ice-sheet thickness change and hence GIA modelling is likely to be small.

3.2.6 Results

The spatial patterns of the first five EOFs used in the reconstruction are shown in Figure 3.2. EOF1, explaining the largest variance, shows a strong east-west gradient in accumulation on the Peninsula. This reflects the different climate regimes which prevail on the western and eastern sides of the mountain chain running down the spine of the AP (Turner et al., 2002). There is a strong positive signal in the northern Peninsula reflecting the high accumulation rates observed here (Zagorodnov et al., 2012).

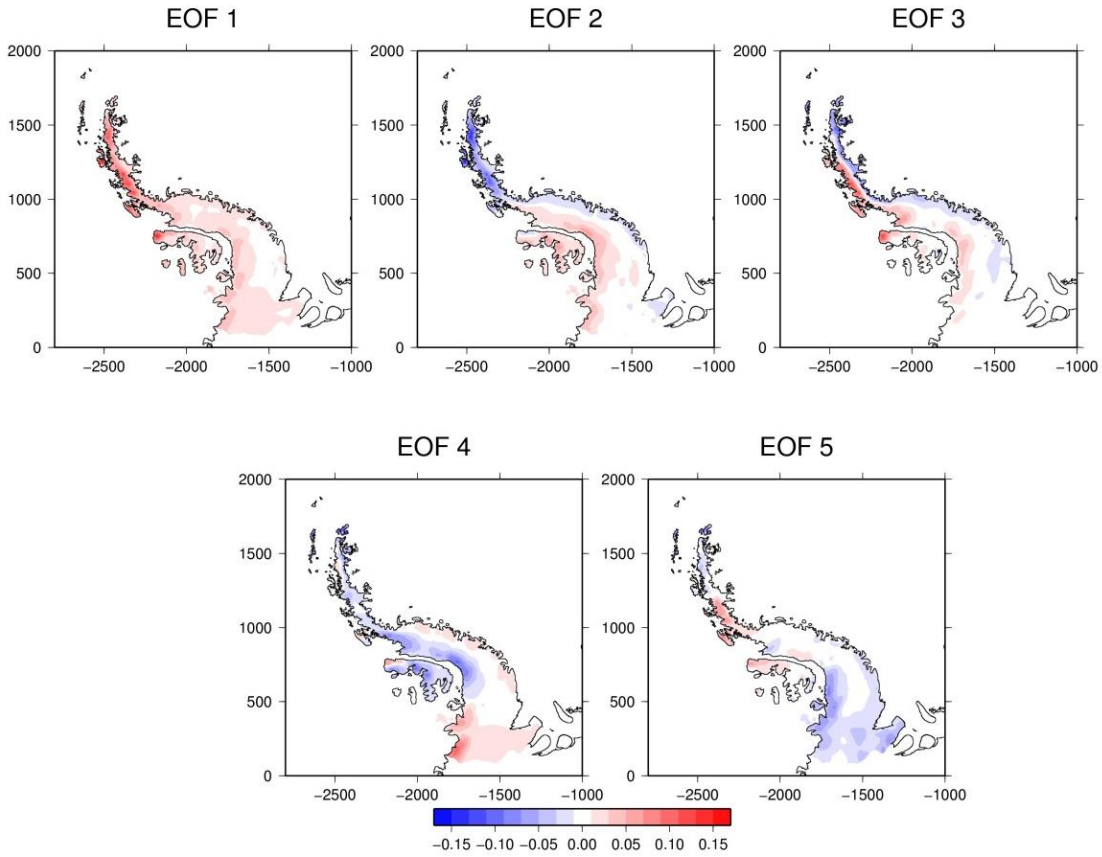

Figure 3.2: Patterns of the first five EOFs, the scale is dimensionless. Only patterns of accumulation in grounded regions are shown. Projection is Polar Stereographic.

To evaluate how well the EOFs are able to reproduce ice core records, the reconstructed accumulation time series for each ice core location is plotted with the original ice core data and the extrapolated part of the record in Figure 3.3a. Gomez, Dyer Plateau and Dolleman Island are particularly well reproduced, although reconstruction of James Ross Island and Siple Station performs less well. To confirm that the method is robust, the reconstruction was recomputed omitting each ice core in turn, so that only data from

the other four ice cores were combined with the first four EOFs. Figure 3.3b indicates that Gomez, Dyer Plateau and Dolleman Island ice core data can be well reproduced using the EOF technique. The ~30 year oscillation at James Ross Island is not well reproduced; however, the general trend, which is most important for this study, is robust. The trend at Siple Station, at the southern extremity of the study domain, is also not well reproduced, and this ice core does not show the same accumulation increase as those in the northern AP. The misfits in these reconstructions are likely due to the ice cores not being representative of the wider area, i.e. that they represent very small scale accumulation features which are not captured in the large-scale patterns of the included EOFs, or that RACMO2.1/ANT model does not represent the spatial pattern accurately in these regions.

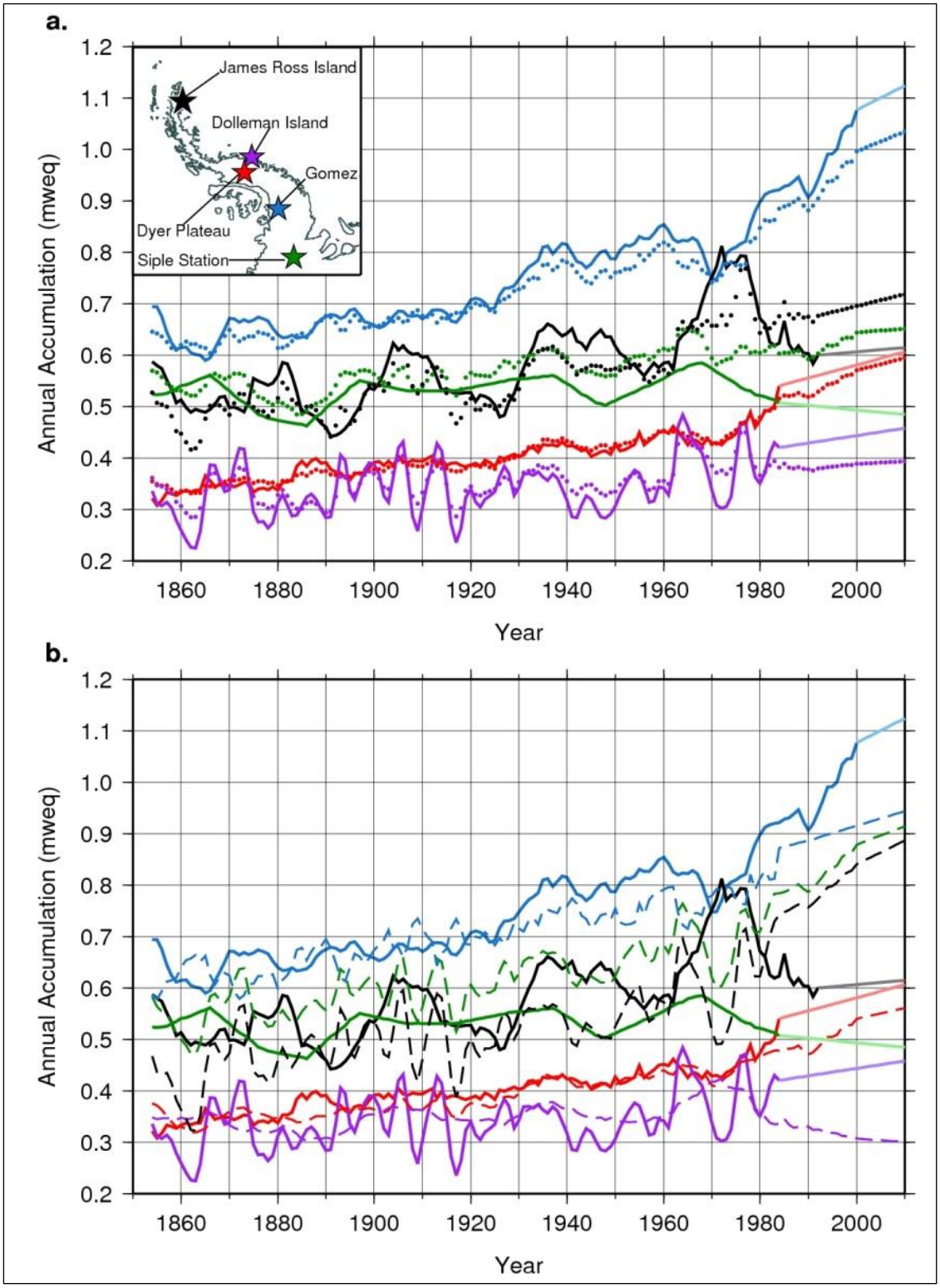

Figure 3.3: Annual accumulation in meters water equivalent (m_{weq}) derived from ice core records (dark solid lines) and extrapolated to 2010 (light solid lines). EOF-reconstructed accumulation time series are shown for each location using data from all ice cores (a, dotted lines), and data from all ice cores except the one being reconstructed (b, dashed lines). Ice core locations are shown in the inset.

3.3 Ice-Sheet Modelling

The reconstructed accumulation history described in Section 3.2 was used to drive an ice-sheet model. A sustained increase in accumulation can lead to changes in the ice sheet as glaciers move towards a new steady state. Additional mass into the system leads to thickening of a glacier, but at the same time, an increase in load has the effect of increasing velocity, transferring ice to the ablation zone thus discharging some of the additional ice. An ice-sheet model can be used to predict net changes in ice-sheet thickness in response to the increasing accumulation. It is the net changes in ice thickness which constitute surface loading/unloading and form the input to the GIA model.

The ice-sheet model used in this study is the Glimmer community ice-sheet model version 1.0.18 (Rutt et al., 2009), as described in Section 2.4.2. Several datasets were required to set up the model, along with the three sources of boundary conditions needed to run the model, climate forcing (surface temperature and mass balance), an isostatic model, and geothermal heat flux. The model configuration and inputs are described in the following sections.

3.3.1 Model Resolution and Domain

Continent-wide Antarctic ice-sheet models generally use a relatively coarse resolution of 20-40 km (e.g. Gomez et al., 2013; Whitehouse et al., 2012a), which is due to a lack of data in some areas and computation time. However, a high resolution is desirable for the Antarctic Peninsula due to its complex topography and steep slopes (Cook et al., 2012) so a 5 km resolution was used for the modelling in this study. As this work concerns the Antarctic Peninsula only, the model domain was truncated along an ice divide at the southern end of the Peninsula, as shown in Figure 3.4, speeding computation time. Ice flow across this boundary was set to zero following the method adopted by Le Brocq et al. (2011) when modelling the Weddell Sea embayment.

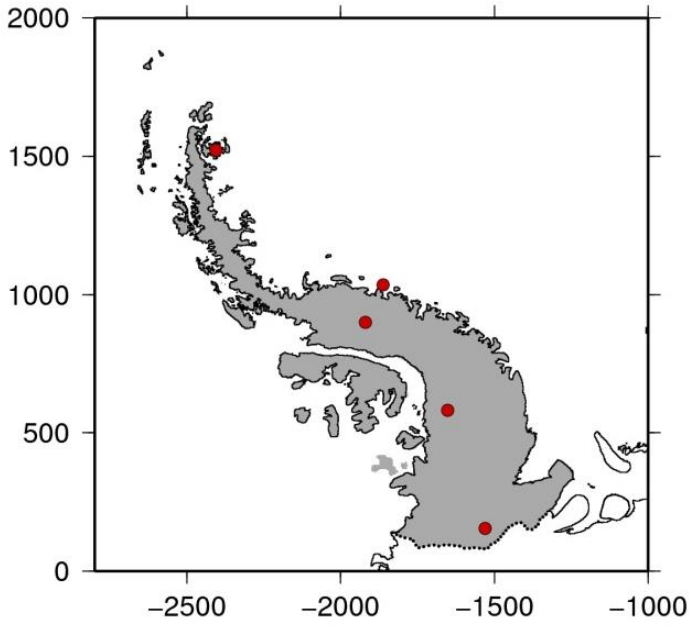

Figure 3.4: Ice-sheet model domain shaded in grey. Ice core locations are shown as red circles. Axes are Antarctic Polar Stereographic X, Y (km).

3.3.2 Model Configuration

Several of the input datasets for the initial model configuration were taken from the ALBMAP v1 dataset (Le Brocq et al., 2010), a collection of present-day datasets for Antarctica, presented in polar stereographic projection on a 5 km grid. Bedrock topography, ice-sheet thickness (derived from upper and lower ice surface datasets) and the grounding line mask were used.

The bedrock topography dataset is a modified version of BEDMAP (Lythe and Vaughan, 2001) (see Le Brocq et al. (2010) for details of the modifications). More recently, Bedmap2 (Fretwell et al., 2013) has become available which shows localised differences in bedrock topography in the AP compared with the ALBMAP topography dataset (see Figure 13 in Fretwell et al. (2013)). Although Bedmap2 is an updated and more complete dataset than that in ALBMAP, much of the fine (1 km) detail captured in Bedmap2 would be lost in the 5 km resolution of the ice-sheet model and so it is unlikely to make significant differences to the results.

3.3.3 Climate Forcing

The climate forcing needed to run a Glimmer model is surface temperature and mass balance. The surface temperature was taken from ALBMAP. Whilst running the model, changes in ice-sheet thickness and isostatic response of the bedrock may cause elevation changes for the ice surface. To account for these changes, the surface air temperature

must be adjusted accordingly through the specification of an altitudinal lapse rate, a relationship describing how temperature changes with elevation. Zagorodnov et al. (2012) report an average altitudinal lapse rate of 0.60 °C/100m from the LARISSA Site Beta in the northern Antarctic Peninsula, and is the value adopted in this study. A similar value of 0.68 °C/100m reported by Martin and Peel (1978) for the west and central Peninsula verifies this result.

The mass balance that drives the ice-sheet model is the output from the EOF reconstruction with values of annual accumulation between 1854 and 2010. This was converted from meters water equivalent to ice equivalent using a density of 917 kg/m^3, and interpolated onto a 5 km polar stereographic grid from the original latitude/longitude 27 km resolution grid. The method for how this changing accumulation was implemented in the model is detailed in Section 3.3.6. A sensitivity study was undertaken using the upper and lower bounds of the EOF reconstruction to test the effect of varying the extrapolation of the ice core data to the present day.

3.3.4 Isostatic Model

Glimmer models a simple isostatic response of the Earth governed by the flexural rigidity of the elastic lithosphere and the relaxation time of the underlying viscous mantle following the approach of Le Meur and Huybrechts (1996). The flexural rigidity of the elastic lithosphere is set to 10^{25} Nm following Whitehouse et al. (2012a) and the relaxation time is 1000 years, slightly lower than that in Whitehouse et al. (2012a) to reflect the weaker mantle viscosity in the Antarctic Peninsula compared with the rest of Antarctica (Ivins et al., 2011). The model assumes that the initial bedrock topography is in isostatic equilibrium with the initial ice loading conditions. Sensitivity analyses were also undertaken to test the effect of increasing the relaxation time to 3000 years and decreasing the flexural rigidity to 10^{24} Nm, which are consistent with the limits tested by Whitehouse et al. (2012a).

3.3.5 Geothermal Heat Flux

Geothermal heat flux is used to calculate the temperature at the base of the ice. As the model domain is relatively small, a spatially constant value of 88 mW/m^2 was used. This value was derived from the LARISSA Beta borehole (Zagorodnov et al., 2012). A sensitivity test was undertaken to investigate the effect of varying this value, using an average global continental value of 65 mW/m^2 (Pollack et al., 1993).

3.3.6 Method

The aim of running the ice-sheet model was to predict changes in ice-sheet thickness in response to an accumulation increase. In order to determine net changes there must be a reference ice thickness to compare the results to. To determine this reference ice thickness the model was first run to equilibrium with the input parameters and datasets described above, in other words the model was run to a stable state where the ice-sheet thickness did not significantly change. Present-day data sets, e.g. bedrock topography and ice thickness, were used as initial conditions; however, by running the model to equilibrium the conditions were allowed to change according to the applied climate forcing. The climate forcing applied to the model to run it to an equilibrium state was present-day temperature and the accumulation for 1854, the first year of the reconstruction, which was held constant through time. Sensitivity studies showed the model was approaching steady state after 10000 time steps (one time step is equivalent to one year), so all models were run for 30000 time steps to ensure equilibrium was achieved.

The ice temperature profile is a function of the temperature conditions under which the ice built up, and affects how the ice flows with colder ice being stiffer. By using present-day temperature to run the model to equilibrium, the model is being forced to build up ice only under these conditions and hence it may not be representative of the true ice temperature profile. However, analysis of an ice core recently drilled to bedrock on James Ross Island (Mulvaney et al., 2012) suggests that temperatures have only been colder than present between ~2500 and 600 years ago with stable temperatures slightly warmer than present prevailing between 9200 and 2500 years ago. This suggests that using the present-day temperature profile to stabilise the model is a reasonable approximation.

Once the model was at equilibrium the variable climate forcing was introduced. For each subsequent year of the model run the reconstructed accumulation time history was used as input, from 1855 to 2010. A second model run was performed which continued to run with the 1854 accumulation forcing. Total ice-sheet thickness was output every five years of each model run from 1855 to 2010, and differenced with each other to obtain the cumulative ice-sheet thickness change due to the reconstructed accumulation history. A median filter over a 50 km width was applied to the output to remove any grid cells with anomalous ice thickness changes.

3.3.7 Results

In response to the increasing accumulation between 1855 and 2010, the ice-sheet model predicts ice thickness increases of up to 45 m, with the greatest increases seen in the west and north of the AP Figure 3.5a. Examining this increase over 50 year time periods (Figure 3.5(b-d)) it is clear that the majority of the ice-sheet thickness increase occurs during the past 50 years, with little increase occurring before 1910. This reflects the ice core records where annual accumulation is general constant for the first 50 years, and increasing significantly from 1930 onwards.

As described previously, using the ice-sheet model is necessary to take account of any change in ice-sheet dynamics caused by the increase in load. The importance of this can be demonstrated by comparing the difference (Figure 3.6c) between the ice thickness increase predicted from ice-sheet modelling (Figure 3.6a) and the sum of the reconstructed accumulation history (Figure 3.6b). Much of the accumulation increase over the narrow northern AP predicted by the accumulation reconstruction is offset by ice discharge into the ocean during the experiment, reducing peak accumulation from 120 m to 45 m. This discharge is due to a velocity increase during the model run (Figure 3.7). At most other locations where glaciers flow more slowly, the difference between the summed accumulation history and ice-sheet model output is less than 10 m.

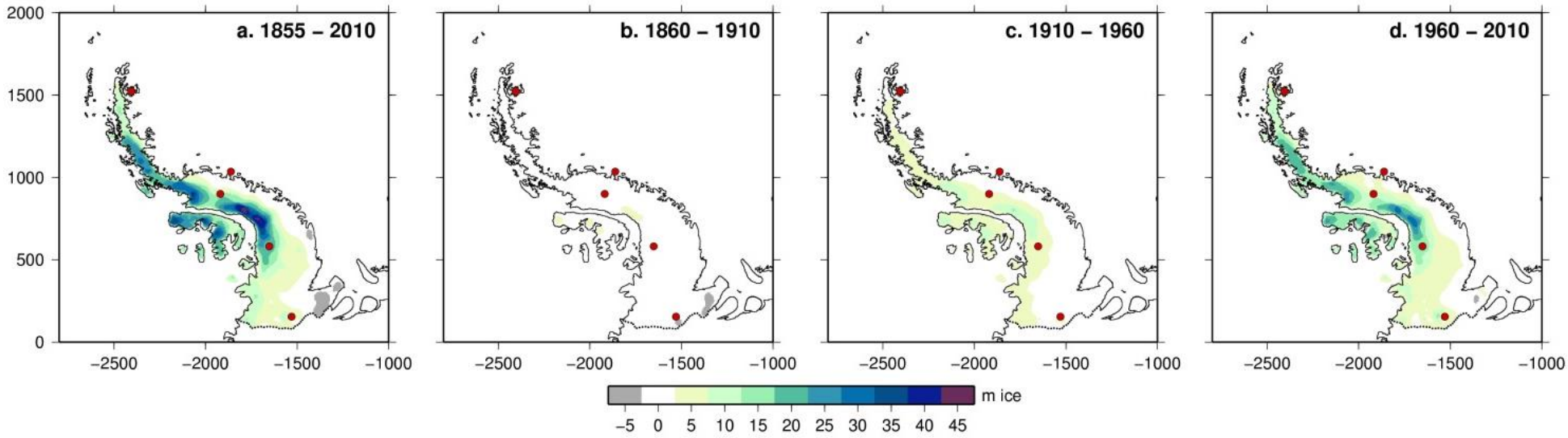

Figure 3.5: Ice-sheet model output showing net ice thickness change between (a) 1855 and 2010; (b) 1860 and 1910; (c) 1910 and 1960; and (d) 1960 and 2010. Ice core locations are shown as red circles. The southern boundary of the ice-sheet model domain is shown as a black dotted line. Axes are Antarctic Polar Stereographic X, Y (km).

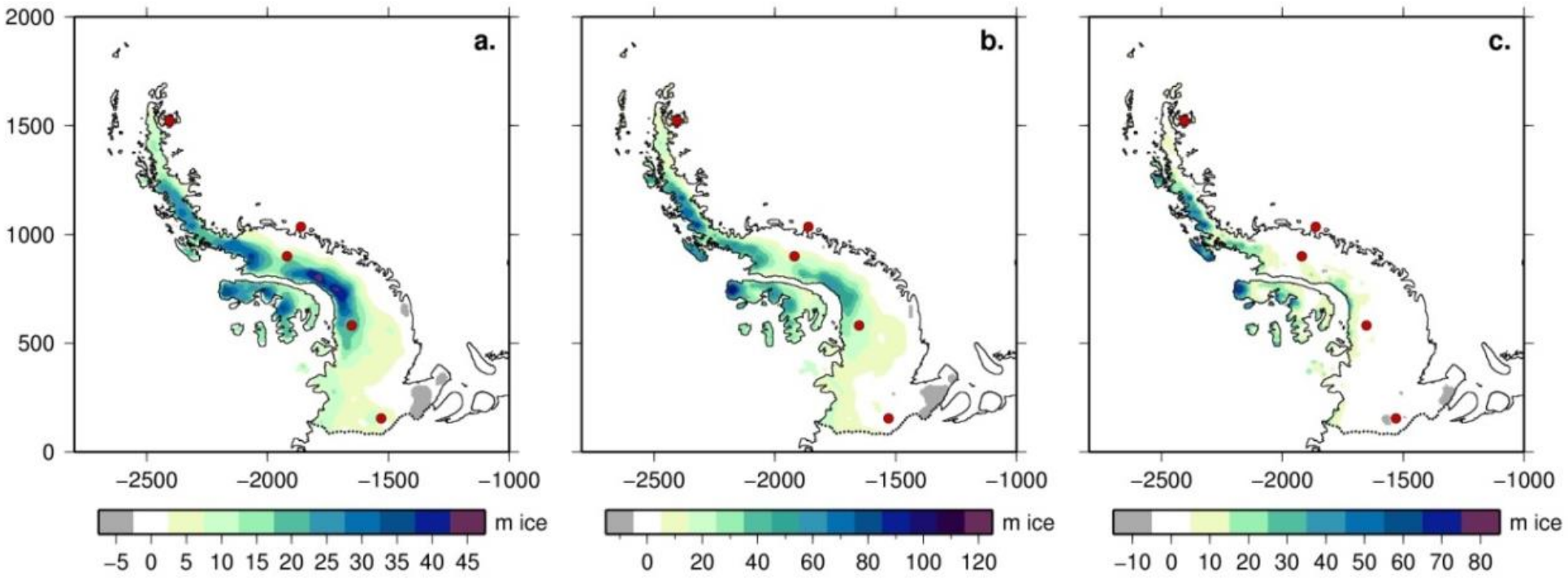

Figure 3.6: (a) Ice-sheet model output showing net ice thickness change between 1855 and 2010; (b) Sum of the reconstructed accumulation history between 1855 and 2010; (c) Effect of ice flow, i.e. (b) minus (a). Ice core locations are shown as red circles. Note that a different colour scale is used in each plot. The southern boundary of the ice sheet-model domain is shown as a black dotted line. Axes are Antarctic Polar Stereographic X, Y (km).

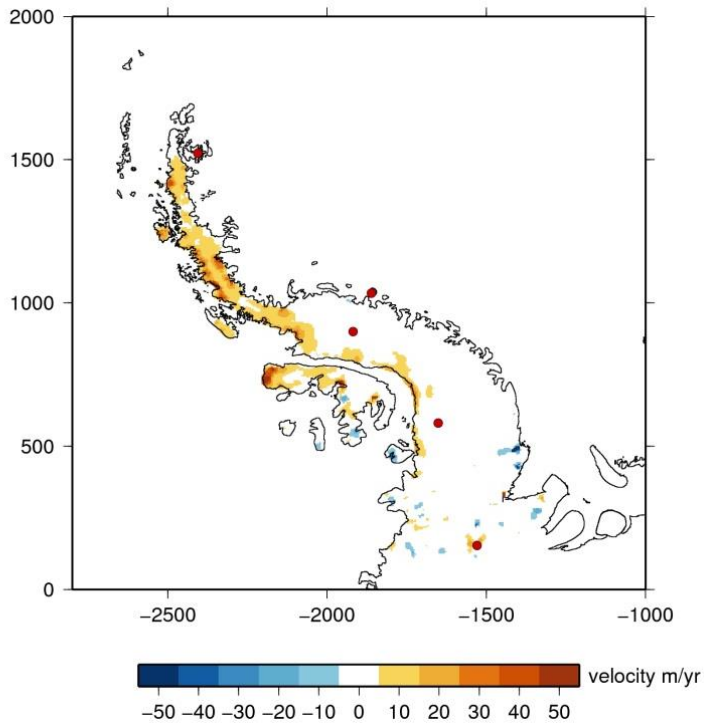

Figure 3.7: Velocity increase during the model run. Ice core locations are shown as red circles. Axes are Antarctic Polar Stereographic X, Y (km).

3.3.8 Sensitivity Analyses

The results of the sensitivity analyses are presented below. The upper and lower bound accumulation histories reconstructed from the EOF analysis, corresponding to the different extrapolated ice core rates, were used as climate forcing input. The difference in total ice thickness change at 2010 when compared with the best estimate model run is ±0-3 m (Figure 3.8), around 10% of the best estimate thickness, and is concentrated in the areas of high accumulation on the west and north of the Peninsula.

The sensitivity test for the isostatic model allowed investigation of the effects of increasing the relaxation time to 3000 years and decreasing the flexural rigidity to 10^{24} Nm. The results are shown in Figure 3.9a and Figure 3.9b, respectively. For the majority of the model domain there is no difference in the ice thickness change predicted by the model. However around the periphery of the domain there are small areas of differences up to ±20 m, with no distinct pattern.

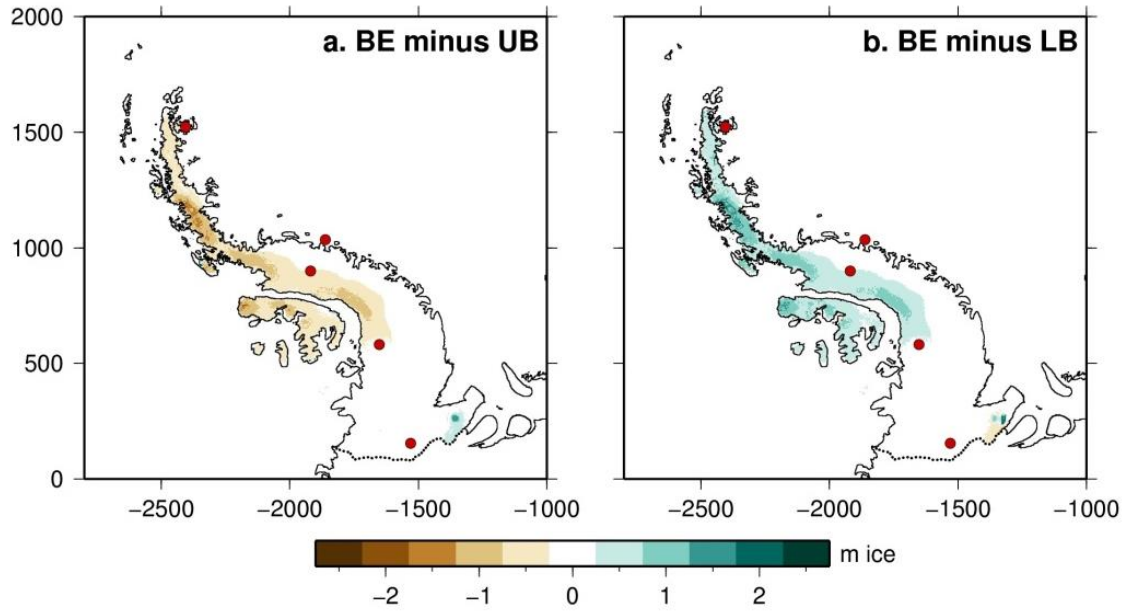

Figure 3.8: Difference in total ice thickness change at 2010 between the original model and model runs using a) the upper bound, and b) lower bound reconstructed ice histories.

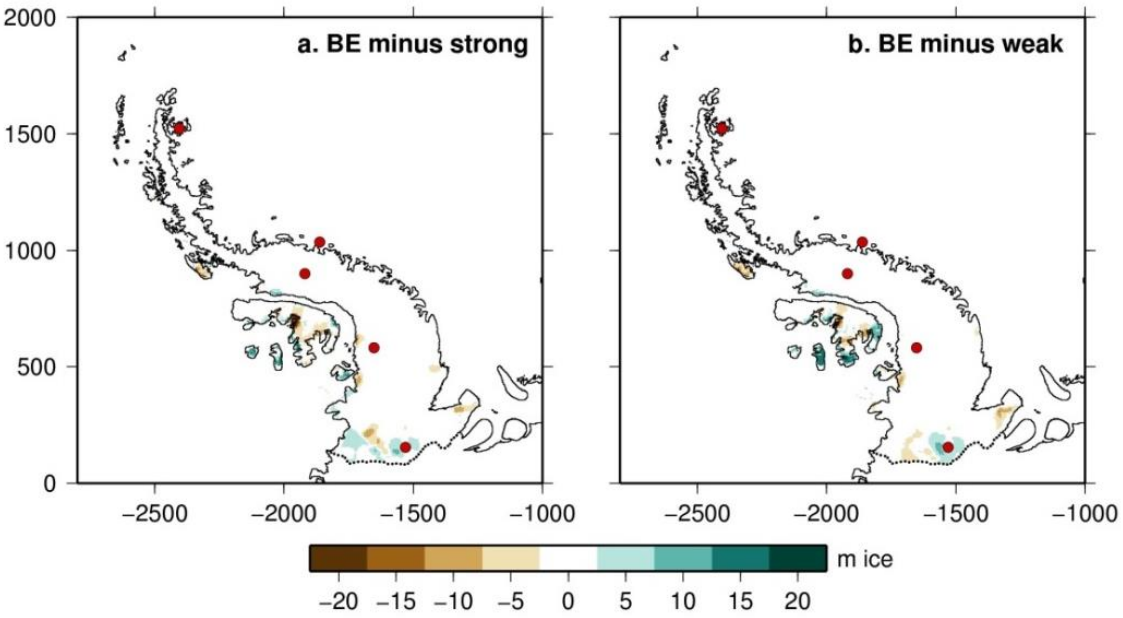

Figure 3.9: Difference in total ice thickness change at 2010 between the original model and model runs with a) a relaxation time of 3000 years, and b) a flexural rigidity of 10^{24} Nm.

Changing the value of the geothermal heat flux to 65 mW/m^2 from that of 88 mW/m^2 used in the original model has a similar effect. Figure 3.10 shows that for the majority of the model domain the difference in ice-sheet thickness change when compared with the best estimate run is negligible. However several small pockets of differences up to ±20 m are present around the edge of the domain.

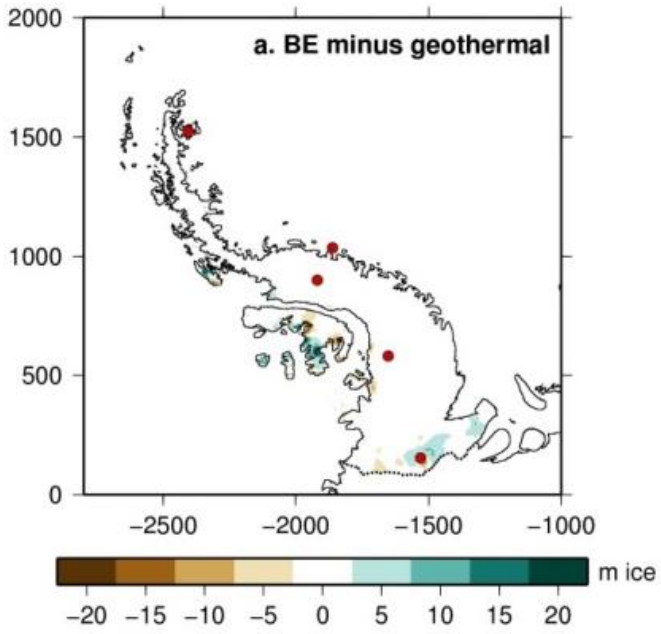

Figure 3.10: Difference in total ice thickness change at 2010 between the original model and model runs with a geothermal heat flux of 65 mW/m^2.

The differences in net ice-sheet thickness change shown in the results of the sensitivity tests are remarkably similar when testing the isostatic model and the value of geothermal heat flux, both in terms of magnitude and spatial pattern. Since there is no obvious reason why these different tests would produce such similar results, it is concluded that varying the isostatic model and geothermal heat flux makes a negligible difference to the overall net ice-sheet thickness change, but reveals locations where the model is unstable, or more susceptible to changes in boundary conditions.

The areas of instability are all located where the ice sheet is grounded below sea level, and there are several factors which may be influencing the results. The basal sliding parameter is derived based on whether the ice sheet is grounded above or below sea level. If the ice sheet is grounded below sea level, the basal sliding parameter is a function of the thickness above buoyancy, therefore changes in ice-sheet thickness may lead to increase or decrease in the basal sliding parameter. Changes in velocity will also result from a change in basal sliding or may occur as a result of the changing boundary conditions, meaning more or less may build up in these local areas. Finally, errors in the basal topography, or limitations in the model resolution compared to the steep topography of the Peninsula may also cause localised ice-sheet thickness changes when the boundary conditions are altered.

Nevertheless, as the magnitude of the differences shown in Figure 3.9 and Figure 3.10 are generally less than ±20 m and confined to small localised areas, it is concluded that

varying the isostatic model and geothermal heat flux boundary conditions has little effect on the overall net ice-sheet thickness increase, and any differences will have a negligible effect on the GIA model predictions.

3.4 GIA Modelling

The net changes in ice-sheet thickness were used as loading input to a GIA model (Section 2.2.1) to predict present-day uplift and geoid rate perturbation. Although the model is global, only ice-load changes in the Antarctic Peninsula were modelled in order to isolate the response in this region. Ice outside of the model domain was therefore set to zero. The inputs are described in the following sub-sections.

3.4.1 Ice History

The net ice-sheet thickness changes described in Section 3.3.7 were interpolated onto a global spherical harmonic grid of degree and order 256, representing a smoothing of the 5 km output. The resolution was limited by the Earth models provided as part of the GIA code (see also Section 2.2.1). When running the model, loading is defined as the change in ice thickness between time steps. The model was run from 3000 years before present to present day, where present-day is defined as the year 2012, including a spin up of the model with zero ice thickness change before 1855. There was also no change in ice thickness in the final five time steps (2010 – 2014), eliminating the elastic effects of a changing load from the calculated present-day uplift rate. Ice loading changes were input on 10 year time steps between 1860 and 2010, with an initial 5 year time step between 1855 and 1860. The time steps and ice-sheet model output used for each time step in the GIA model are listed in Table 3.2.

Time-step (years before present)	Ice-sheet model output used
3000	1855
2000	1855
1000	1855
500	1855
157	1855
152	1860
142	1870
132	1880
122	1890
112	1900
102	1910
92	1920
82	1930
72	1940
62	1950
52	1960
42	1970
32	1980
22	1990
12	2000
2	2010
1	2010
0	2010
-1	2010
-2	2010

Table 3.2: GIA model time steps and the ice sheet output used for each time step.

3.4.2 Earth Model

As described in Section 2.2.1, the three-layer Earth model can have values of 46, 71, 96, 120 km for lithospheric thickness; 0.05, 0.08, 0.1, 0.2, 0.3, 0.5, 0.8, 1, 2, 3, 5×10^{21} Pa s for upper mantle viscosity; and 1, 2, 3, 5, 8, 10, 20, 30, 50×10^{21} Pa s for lower mantle viscosity. The upper mantle extends to 660 km depth and the lower mantle extends to 2900 km depth (the core-mantle boundary).

The GIA model was run with a range of different Earth models within the parameters stated above to investigate the effects on the present-day uplift rate. For comparison, results are presented with three different Earth models (Table 3.3). The first within the range of values suggested by Ivins et al. (2011) which is appropriate for the northern AP, a slightly stronger Earth model which is likely to be suitable for the southern AP, and finally the preferred Earth model of Whitehouse et al. (2012b) which was derived

for the whole of Antarctica. The lower mantle viscosity has little effect on the results and was set to 1×10^{22} Pa s for all three models.

Earth Model	Lithospheric Thickness (km)	Upper Mantle Viscosity (Pa s)	Lower Mantle Viscosity (Pa s)
Northern AP (Ivins et al., 2011)	46	5×10^{19}	1×10^{22}
Southern AP	71	1×10^{20}	1×10^{22}
All Antarctica (Whitehouse et al., 2012b)	120	1×10^{21}	1×10^{22}

Table 3.3: Parameters for the three different Earth models used.

3.4.3 Sensitivity Analyses

Uncertainties in the GIA model output relate to the ice history and Earth model. First, sensitivity analyses on the ice sheet-model output show there are small variations in total ice thickness change due to the upper and lower bound accumulation histories, but that other modelling factors (e.g. choice of isostatic model and values of geothermal heat flux) make no significant difference. Therefore two further ice loading scenarios were modelled to investigate the effect on the GIA signal. Second, the results are sensitive to the spherical harmonic degree of the Earth model. Very few Earth models are available at degree and order 512, although the southern AP model (Table 3.3) is. This Earth model was used to compare GIA results for the different resolutions.

3.4.4 Correction to GRACE

GIA corrections applied to GRACE data will be biased as a result of omitting the signal from recent accumulation. To examine the effect on GRACE-determined rates of ice-mass change the geoid rate perturbation for each GIA model run was calculated and used to estimate the resulting change in surface mass density, using the method described by Wahr et al. (1998) (equations 9 and 13). The surface mass density was then integrated over the area of the grounded ice sheet with an additional 100 km offshore buffer to obtain the total mass contribution for each GIA prediction. This provides realistic values for the correction to GRACE data as a ~100 km buffer would be included in the GRACE processing to capture any leakage from onshore ice-mass change (King et al., 2012a). It is worth noting that the magnitude of the correction will be dependent upon the chosen width of the buffer.

3.4.5 Results

Present-day (2012) GIA model-predictions are presented in Figure 3.11(a-c) for the three Earth models described in Table 3.3, respectively. As expected, the modelled ice loading causes subsidence concentrated on the region of peak ice-sheet thickness increase, with an east-west pattern as seen in the ice-sheet model output. The results are highly sensitive to the adopted Earth model, particularly the upper mantle viscosity. The weakest Earth model, suitable for the northern AP (Figure 3.11a) predicts up to 7 mm/yr subsidence, with the greatest subsidence predicted in the western AP, whereas the strongest Earth model predicts only 0.3 mm/yr.

Calculating the correction to GRACE data due to the geoid perturbation for each GIA model results in an increase in GRACE-determined rates of ice-mass change of +6.2 Gt/yr for the weakest Earth model, and +0.5 to +3.2 Gt/yr for stronger Earth models (see Figure 3.11). Previous mass balance estimates derived using GRACE data will therefore be biased low in the Antarctic Peninsula as a result of neglecting the signal from the recent increase in accumulation. King et al. (2012a) report GRACE-determined rates of ice-mass change of -33 Gt/yr for the northern AP but +28 Gt/yr for Palmer Land, suggesting that net ice-mass loss from these regions combined is marginal at -5 Gt/yr. Further south in the Peninsula, King et al. (2012a) predict ice-mass loss, however their drainage basins extend beyond the study domain used here so the regions cannot be directly compared. Shepherd et al. (2012) report a mass balance estimate of -36 Gt/yr from the AP between 2005 and 2010. It is clear from these studies that the potential +6.2 Gt/yr predicted from recent accumulation-related changes may be significant and brings the AP closer to being in balance. Note that this correction only considers the GIA response to the recent accumulation increase described in this study, and will be additional to corrections for the long term GIA signal and the response to ice-mass loss from ice shelf break-up in the late 20th century.

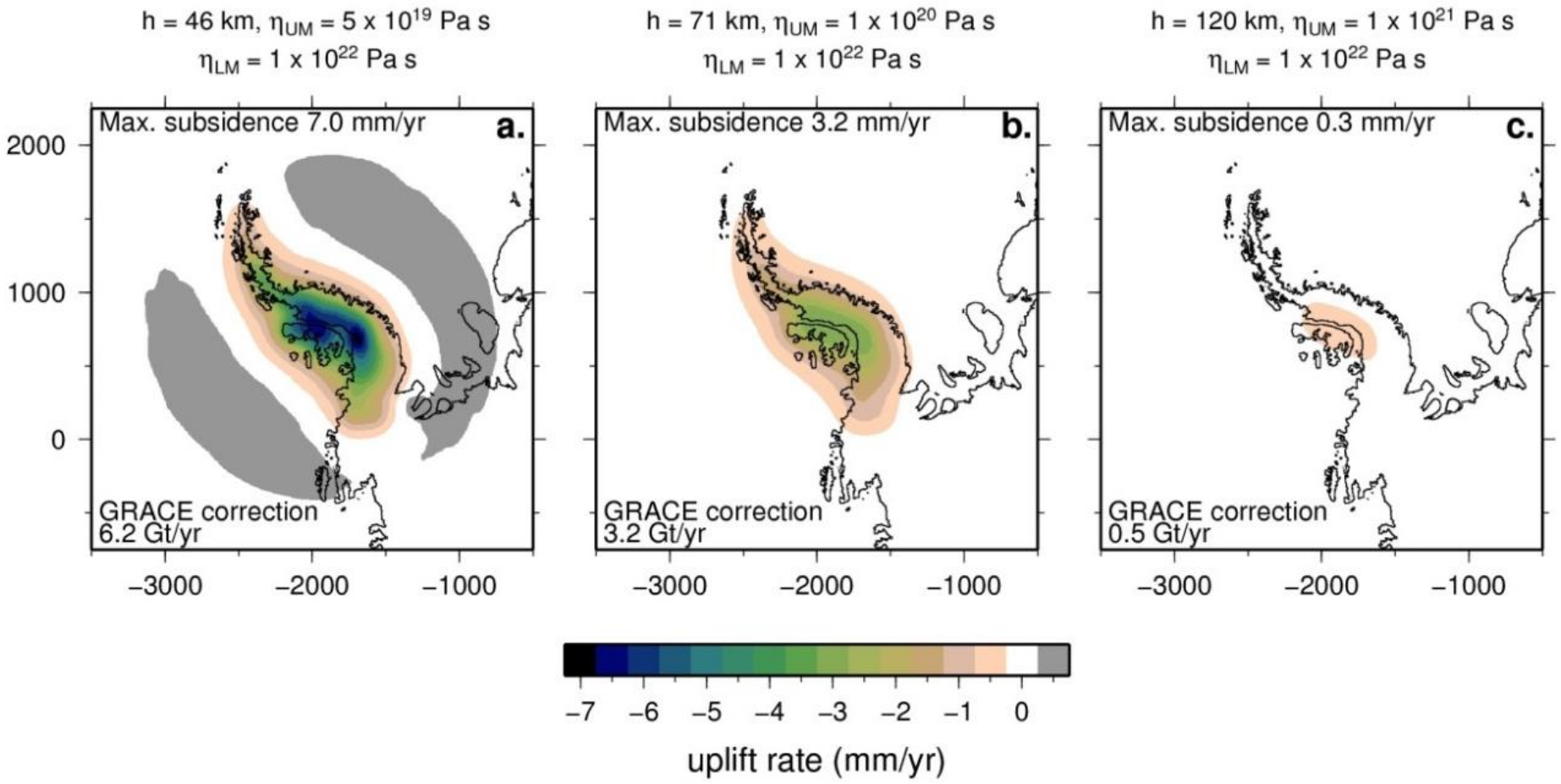

Figure 3.11: Present-day GIA uplift rates for Earth models (lithospheric thickness h, upper mantle viscosity η_{UM} and lower mantle viscosity η_{LM}): (a) appropriate for the northern AP; (b) appropriate for the southern AP; and, (c) *Whitehouse et al.* (2012b) preferred Earth model. Axes are Antarctic Polar Stereographic X, Y (km).

3.4.6 Sensitivity Analyses

The upper and lower bound accumulation histories relating to how the ice cores were extrapolated to present-day were used as input to the GIA model with the three Earth models in Table 3.3. The results show that these different ice histories result in no more than ±0.2 mm/yr difference to the predicted GIA uplift rates, and ±0.2 Gt/yr to the GRACE correction (±0.01 Gt/yr for the Whitehouse et al. (2012b) Earth model).

The Earth model appropriate for the southern AP was used to investigate the difference in GIA signal between spherical harmonic degree 256 and 512. The subsidence signal for each Earth model is shown in Figure 3.12a and Figure 3.12b respectively. The degree 512 Earth model shows slightly more subsidence than the degree 256 model, however Figure 3.12c confirms this is no more than 0.5 mm/yr for the whole domain. As the majority of the Earth's response is from the upper mantle and the lithosphere acts to smooth out this signal, higher spherical harmonic degree models do not produce a significantly different signal.

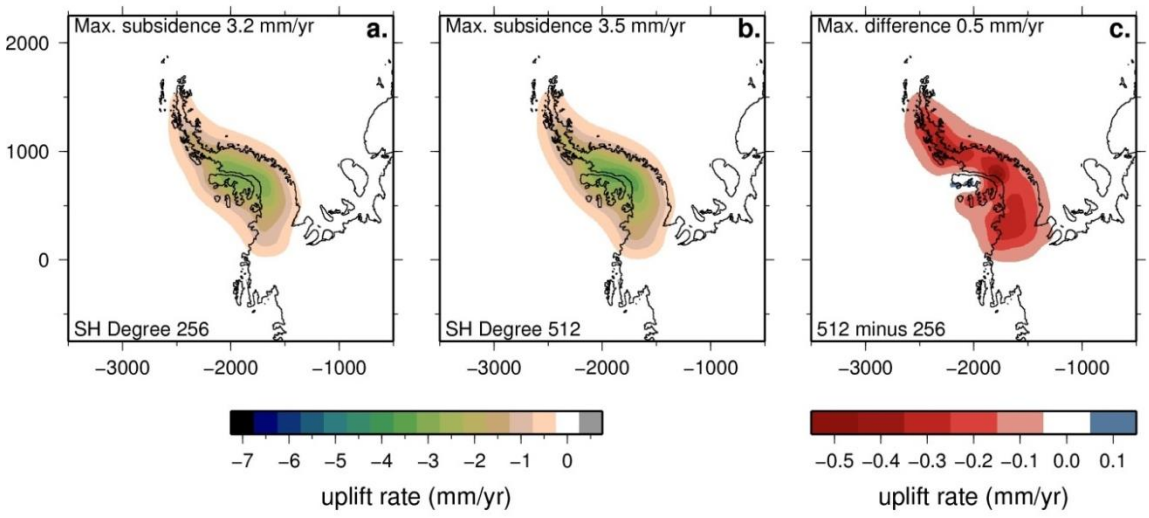

Figure 3.12: Present-day GIA uplift rates for the Earth model in Figure 3.11b at (a) degree 256, (b) degree 512, and (c) the difference, i.e. (b) minus (a).

3.5 Discussion and Conclusions

GIA models tend to over-predict GIA in the Antarctic Peninsula when compared with the low rates of uplift observed in GPS records (Thomas et al., 2011). Whitehouse et al. (2012b) attempted to improve the fit between modelled GIA uplift and GPS-observed uplift by adding an arbitrary, uniform thickness of ice to the AP, and found that this significantly improved the fit at all GPS sites on the AP but resulted in predicted subsidence on the eastern AP for which there is no clear observational evidence. The

work presented in this chapter investigated the possibility that recent accumulation in this region could cause a GIA-related subsidence signal of sufficient magnitude to explain this misfit.

An accumulation history from 1854 to present-day was reconstructed using the spatial pattern of SMB data between 1979 and 2010 and five ice core records from 1854 to 2010 to capture an increase in accumulation. Ice-sheet models using the reconstructed accumulation history as climate forcing predict up to 45 m of ice-sheet thickening over the past 155 years, which may cause significant GIA-related subsidence. GIA model results are highly sensitive to the upper mantle viscosity of the adopted Earth model (Figure 3.11). The weakest Earth model tested, which is appropriate for the northern AP, predicts subsidence rates of 3-4 mm/yr in this region (Figure 3.11a). The Earth model which is likely to be appropriate for the southern AP predicts subsidence rates of up to 3.2 mm/yr in the southern AP (Figure 3.11b). Current GIA models, which do not account for this loading, predict peak uplift rates of between 3 mm/yr (Whitehouse et al., 2012b) and 15 mm/yr (Ivins and James, 2005) for the AP. The results presented in Figure 3.11 demonstrate that an east-west gradient in accumulation can generate a spatially variable GIA response and hence would not result in subsidence on the eastern AP as seen in W12a from a uniform thickness of ice.

If added to an existing ice-loading history such as the W12 ice history (Whitehouse et al., 2012a), the extra ice loading modelled here may explain the low rates of GIA-related uplift observed in the AP from GPS measurements (Thomas et al., 2011). However, using the Earth model derived by Whitehouse et al. (2012b) would result in very little difference to the present-day uplift, as shown in Figure 3.11, and using a weaker Earth model for the W12 deglacial history would not preserve the fit to relative sea-level data. This suggests that either the W12a Earth model is incorrect in the AP region, or a different source of ice-mass change is needed to explain the differences between modelled uplift and GPS-observed uplift. Alternatively, errors in the W12a Late Holocene ice-history may result in too much uplift at present day. If the Earth structure in the Antarctic Peninsula is significantly different to Earth models used in Antarctic-wide GIA models, as suggested by Ivins et al. (2011), rigorous modelling would only be possible using a 3-D Earth model.

GRACE-determined rates of ice-mass change are biased low for this region as a result of omitting the accumulation-related signal which is not currently included in Antarctic

GIA models. A correction of up to ~6 Gt/yr may be needed, depending on the Earth model used, which is around 10-20% of current estimates of mass balance for the AP (-36 Gt/yr (Shepherd et al., 2012)).

In the future, this work could be improved upon when improved models and data become available. A higher resolution modelled SMB dataset could provide more accurate spatial patterns of accumulation and additional ice core records would provide spatially more dense measurements of accumulation. One such ice core has been drilled at a high accumulation site on Bruce Plateau in the northern Antarctic Peninsula (LARISSA Site Beta ice core (Zagorodnov et al., 2012)), although analysis of accumulation has yet to be published. Putting this ice loading into the context of a continent-wide GIA model would also be useful, once 3-D GIA models become more widely used.

This work addresses the importance of Late Holocene ice loading in the modelling of GIA, an issue which is relevant throughout Antarctica, but particularly important for regions of weak Earth structure. An important implication of this work is that accumulation-driven subsidence will significantly perturb GPS velocities which are used to validate or constrain models of GIA (e.g. IJ05_R2 (Ivins et al., 2013)), which could be incorrect if they do not also consider Late Holocene ice-mass change. Applying these models to GRACE data may also lead to inaccurate estimates of present-day ice-mass change. This highlights the need for more constraints on Late Holocene ice-sheet evolution to drive high resolution ice-sheet and GIA modelling.

Chapter 4. Recent Ice Unloading in the Northern Antarctic Peninsula

4.1 Introduction

In regions of low viscosity mantle it is important to consider ice-mass changes over the past few hundred to thousand years as they could dominate present-day uplift (Ivins et al., 2000). The work presented in Chapter 3 showed that ice loading on a centennial scale in the Antarctic Peninsula could contribute significantly to the present-day GIA signal, given a weak Earth model; however, it remains uncertain what the Earth model in this region is. In order to be able to constrain a regional Earth model, good observations of uplift and ice-mass change are required. In this chapter a regional Earth model for the northern Antarctic Peninsula (NAP) is estimated from GPS-observed uplift and a high resolution dataset of present-day ice-mass loss on a decadal scale.

As described in Chapter 1, there have been rapid changes in climate in the Antarctic Peninsula over the past 50 years which have led to the retreat and eventual collapse of several major ice shelves. In the most northern Peninsula Prince Gustav and Larsen A collapsed in 1995 (Rott et al., 1996), and Larsen B collapsed in 2002 (Rack and Rott, 2004) (Figure 4.1) (see Cook and Vaughan (2010) for a complete summary of ice shelf breakup). In response to ice shelf collapse, tributary glaciers have exhibited acceleration and thinning (e.g., Rignot et al., 2004; Scambos et al., 2004; De Angelis and Skvarca, 2003) and this dynamic ice loss induces a solid Earth response which may be observed in GPS records.

The study of Thomas et al. (2011) identified markedly-increased uplift in GPS coordinate time series from the NAP that they associated with ice unloading related to the breakup of Larsen B Ice Shelf in 2002. This uplift was best captured in the near-continuous GPS record at Palmer station which exhibited an increase in uplift rate from 0.1 mm/yr prior to 2002.2, to 8.8 mm/yr thereafter. Thomas et al. (2011) suggested that the effect was due to the elastic response of the solid Earth but they were not able to satisfactorily reproduce the increased uplift rates with an elastic model, which they suggested was at least partly due to the weakly defined magnitude and spatial pattern of ice-mass loss in their model.

The NAP lies in a complex tectonic setting which passes from active subduction along the South Shetland Trench, located north of the South Shetland Islands, to passive margin west of 65°W at the intersection of the Hero Fracture Zone with the Shetland

Platform (Figure 4.1). The volcanically active Bransfield Basin separates the South Shetland Islands from the NAP and is presently extending (Taylor et al., 2008), suggesting a back arc tectonic setting (Barker et al., 2003; Barker et al., 1991). The mantle below a back arc setting such as this would likely contain water and volatiles (Wiens et al., 2006), and temperature anomalies, as has been shown by Park et al. (2012) for the Bransfield Basin. These factors would contribute to a low viscosity upper mantle, as demonstrated by Dixon et al. (2004) for the upper mantle in the western United States.

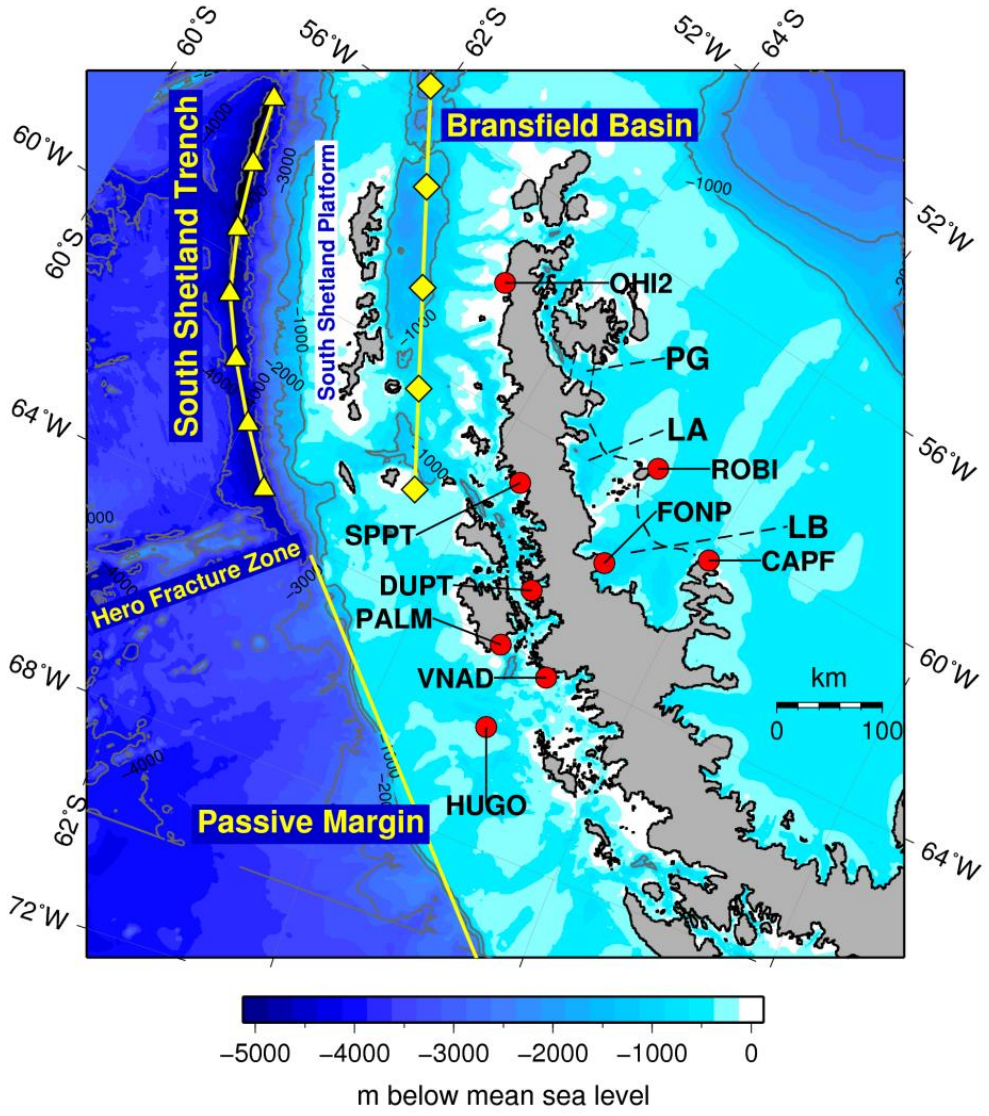

Figure 4.1: Bathymetry (Willis et al., 2012) of the study region showing the location of the active subduction zone (South Shetland Trench), the Bransfield Basin and the Passive Margin (Barker, 1982). GPS locations are shown as red circles and former ice shelf locations as dashed black lines (Prince Gustav (PG), Larsen A (LA) and Larsen B (LB)).

Due to the active tectonic setting of the region, the mantle is likely to have a relatively low viscosity compared with other locations undergoing deformation in response to

ice-mass changes e.g. East Antarctica or Fennoscandia. Ivins et al. (2011) suggested this region has a relatively thin lithosphere (20-45 km) and a low viscosity upper mantle (3-10 × 10^{19} Pa s) which they estimated using a combination of inferred ice history, GPS and GRACE data. Due to the low viscosity nature of the upper mantle, the Earth's viscous response to ice-mass change in the AP is much more rapid than in other regions of Antarctica, and post-1995 unloading events may hence be contributing to the observed uplift in the NAP through viscoelastic rebound. Likewise, there may be very little, to no, residual response of the NAP to unloading events associated with recession from the Last Glacial Maximum.

The aim of the work described in this chapter is to use GPS data from the NAP to constrain a local model of solid Earth response to a high resolution present-day mass-loss field (Scambos et al., 2014). First, the modelled elastic uplift time series was compared with the GPS-observed uplift time series from Palmer Station to verify that elastic uplift alone is not able to reproduce the non-linear GPS observations. A viscoelastic model was then used to predict uplift, and results were compared with the Palmer record to obtain the range of best-fitting models. Finally, the Earth model was further refined using six shorter GPS time series from the NAP (see Table 4.1).

Site	Latitude (°)	Longitude (°)	Observing Period	GPS Observed Uplift (mm/yr)
Palmer (PALM)	-64.78	-64.05	1998.5 - 2013.0	1998.5 - 2002.2: 0.7 ± 1.6 2009.0 - 2013.0: 6.6 ± 2.1
Cape Framnes (CAPF)	-66.01	-60.56	2010.1 - 2013.0	4.5 ± 2.9
Duthier's Point (DUPT)	-64.81	-62.82	2009.3 - 2013.0	12.8 ± 2.1
Foyn Point (FONP)	-65.25	-61.65	2010.1 - 2013.0	14.9 ± 2.7
Hugo Island (HUGO)	-64.96	-65.67	2009.3 - 2013.0	1.7 ± 3.3
Robertson Island (ROBI)	-65.25	-59.44	2010.1 - 2013.0	7.8 ± 2.9
Vernadsky (VNAD)	-65.25	-64.25	2010.1 - 2013.0	5.8 ± 2.4

Table 4.1: Location of GPS stations, observing period, and observed uplift velocities.

4.2 Data

4.2.1 GPS Data

Figure 4.1 shows the locations of available GPS sites in the NAP. Of these, the seven sites closest to the region of ice-mass change were used in this study (see Table 4.1). Palmer is a long-term station with in excess of 15 years of data, and the remaining six sites were installed in 2009-2010 as part of the LARISSA project (LARsen Ice Shelf System, Antarctica) (http://www.hamilton.edu/expeditions/larissa). The record from O'Higgins (a compilation of three records from two adjacent stations, OHIG, OHI2, OHI3; labelled OHI2 on Figure 4.1) was not used as a constraint as it lies far from the region of largest mass loss and as such may be affected by potential lateral heterogeneity in Earth structure. Campaign data from Spring Point (Bevis et al., 2009) (SPPT on Figure 4.1) was also excluded due to the lack of data at this site; however, model results are compared with both of these records later. A further LARISSA site was installed within a few tens of metres of SPPT in 2013, although this data was not used in this thesis, and another is due for installation further south in 2014.

The GPS data from 1998 through to the end of 2012 were processed as described in Nield et al. (2014). Several large outliers from the DUPT time series were manually identified and removed, and a median filter with a width of 0.02 years (~1 week) was applied to all time series. Only height time series were considered in this work.

Velocities and realistic uncertainties were estimated using the CATS software (Williams, 2008), along with annual and semi-annual harmonics. In addition to white noise, where measurement errors in a time series are assumed to be uncorrelated with one another, GPS time series contain time-correlated noise, (also known as power-law noise) (Williams, 2003). Both of these types of noise need to be taken account of when estimating GPS velocity uncertainties otherwise they can be significantly under-estimated. A common approach to modelling noise in GPS time series is to use a white noise plus flicker noise model (Williams, 2008), and this is the method applied in this study to determine velocity uncertainties using the CATS software. These were scaled to represent 2-sigma uncertainties for subsequent use. Velocities and 2-sigma uncertainties for each GPS site are given in Table 4.1. Below, model output is compared with both the height time series and vertical velocities derived from the time series. For consistency, all model-predicted uplift rates were estimated over the same time period as the GPS-observed uplift rates were estimated.

4.2.2 Ice-Mass Change Data

The input ice load model is based on a dataset of elevation change derived from Digital Elevation Model (DEM) differencing and ICESat data covering the NAP region north of 66°S (Scambos et al., 2014), as shown in Figure 4.2 and Figure 4.3. The time span of the data varies for different sub-regions. For the Larsen B tributary glaciers data is available for two time periods, 2001-2006 (Figure 4.3a) (Shuman et al., 2011) and 2006-2011 (Figure 4.3b) (Berthier et al., 2012). Comparing the two time-periods reveals differences in spatial patterns of elevation change but the overall estimated mass loss during these two periods differs by less than 10% (Berthier et al., 2012). For the areas north and west of Larsen B, including Prince Gustav and Larsen A tributary glaciers, the dataset spans the period 2001-2010 (Scambos et al., 2014), and the original data is shown in Figure 4.2. In all cases the rate of ice-mass change is assumed to be constant throughout the respective data periods; extrapolation to other time periods is discussed later.

The data were converted to a set of 17,846 loading discs for input to the model with areas between 0.9 and 1.1 km^2. The height of each disc represents a loss or gain, using a density of 900 kg/m^3 to convert from ice to equivalent water height following Berthier et al. (2012). Data gaps over large glaciers were infilled using an inverse distance weighting algorithm (inpaint_nans for Matlab: http://www.mathworks.co.uk/matlabcentral/fileexchange/4551-inpaint-nans), and away from large glaciers infilling of the data gaps does not have any effect due to the sparse data. Ice-mass change in non-grounded regions was discounted as it has no effect on solid Earth deformation. Discs with very small mass change in the range ±0.5 m_{weq}/yr have a negligible effect on deformation at sites tens to hundreds of km distance from the source of loading and were discounted from the ice load model to speed computation time. This was verified using the best-fitting Earth model and resulted in no more than ±0.2 mm/yr difference in uplift rates at the GPS sites. The resulting ice-mass change model is shown in Figure 4.4a with the two periods of mass change for Larsen B glaciers, 2001-2006 and 2006-2011, shown separately in Figure 4.4b and c, respectively. The 2-sigma uncertainty on the elevation change dataset is ±1 m/yr (personal communication, T. Scambos to M. King 04/04/2013), and this error bound was used to create upper and lower limits on the input ice load model.

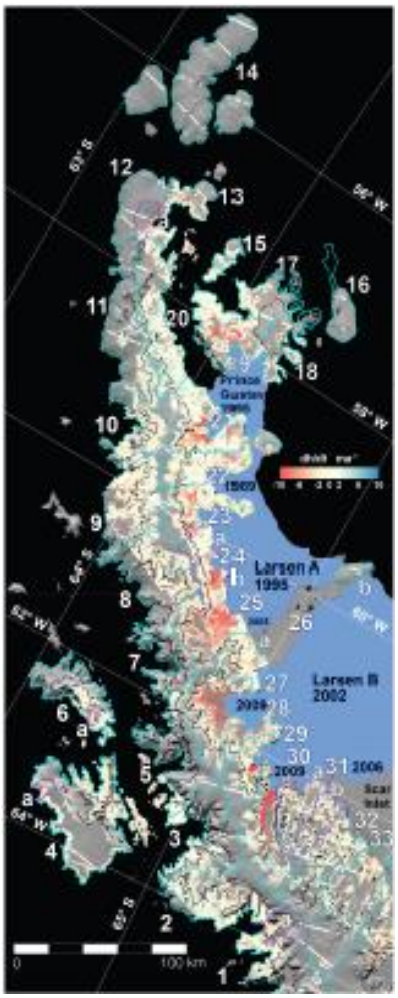

Figure 4.2: Elevation change rate in meters per year for 2001-2010 taken from Scambos et al. (2014) (Figure 2). Elevation change for Larsen B glaciers is for 2001-2006, as shown in Figure 4.3a.

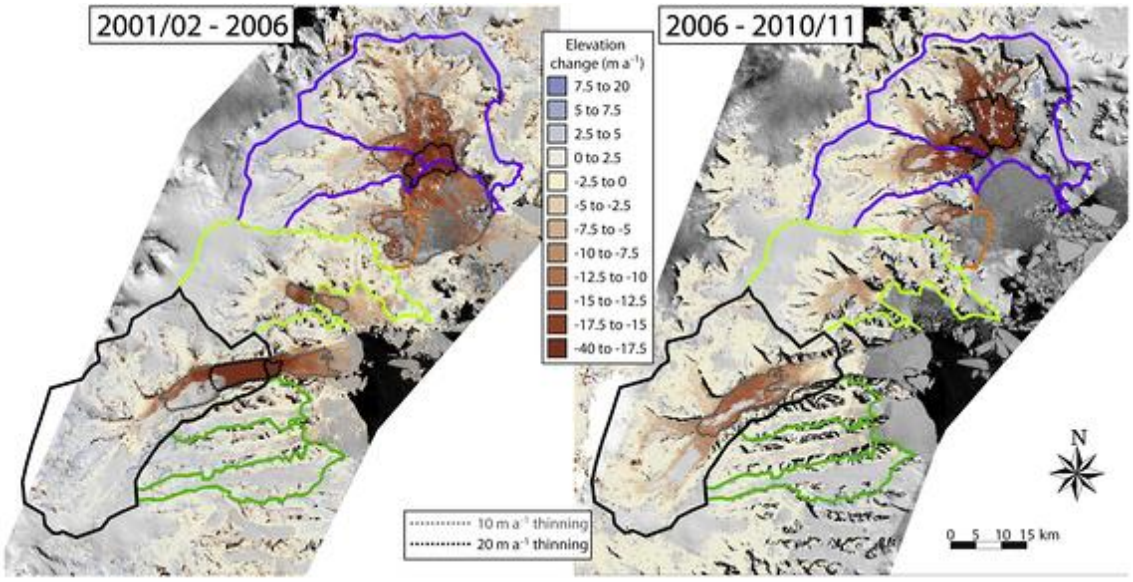

Figure 4.3: Elevation change rate in meters per year for Larsen B glaciers for 2001-2006 and 2006-2011. Figure has been taken from Berthier et al. (2012)Figure 2), and the data in the left panel is from Shuman et al. (2011).

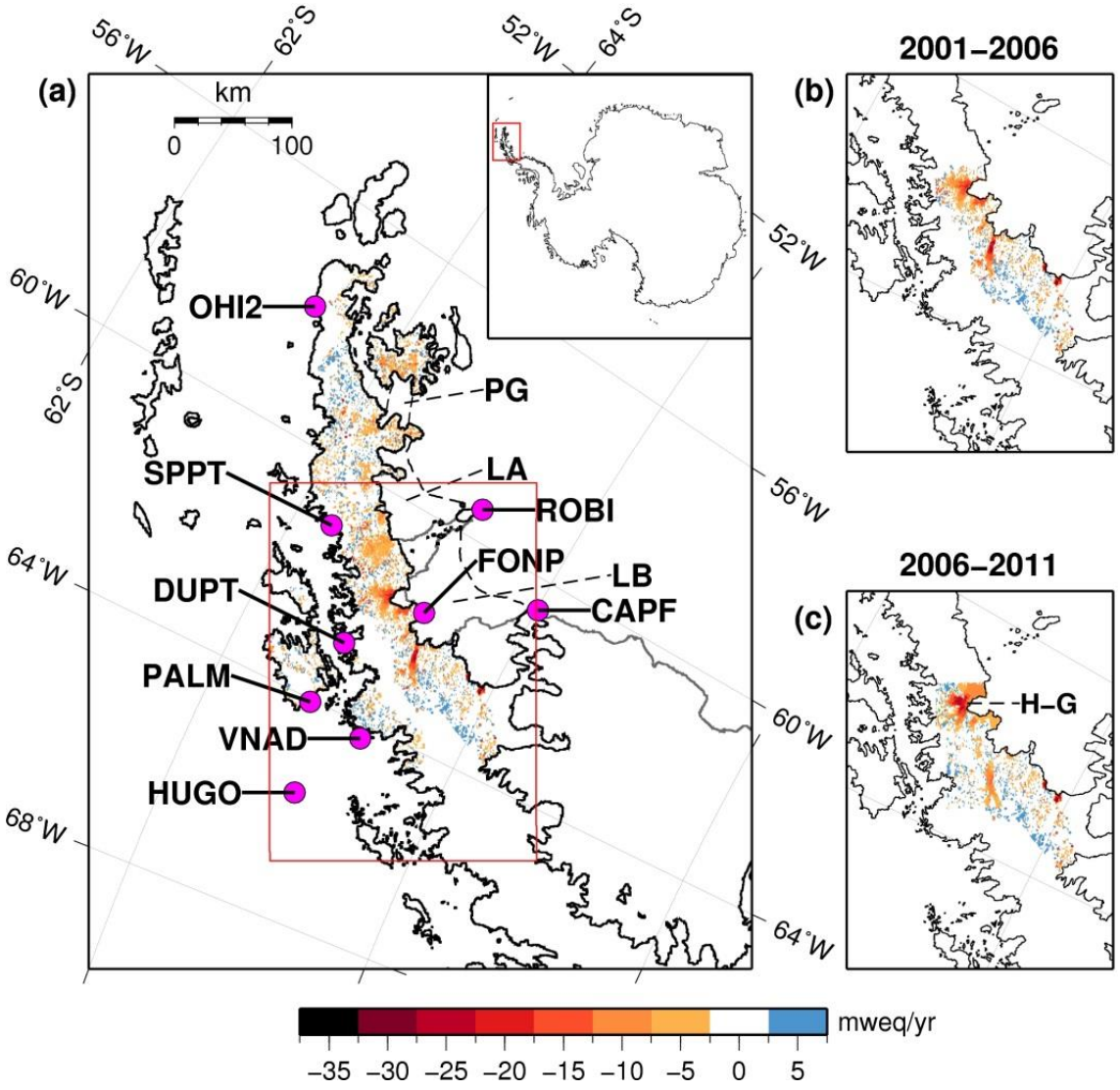

Figure 4.4: Infilled ice-mass change rate given in meters water equivalent per year. a) The full study area with GPS locations shown as pink circles and former ice shelf locations as dashed black lines (Prince Gustav (PG), Larsen A (LA) and Larsen B (LB)). Values in the Larsen B area (see panel b) represent the mean rate of change for the period 2001-2006, values elsewhere represent the mean rate of change for the period 2001-2010. Inset shows location of the study area. b) Ice-mass change for Larsen B only using 2001-2006 data. c) Ice-mass change for Larsen B only using 2006 2011 data. H-G is the Hektoria-Green drainage basin.

The aim of this study is to model the Earth's response to ice-mass loss related to the collapse of Prince Gustav, Larsen A and Larsen B ice shelves in 1995 and 2002, up to the present-day in order to compare model results with GPS data. However, ice-mass loss data is not available before 2001 or after 2011, so in order to extrapolate the ice loss data backwards and forwards in time several key assumptions were made.

1. It was assumed that ice-mass loss in a region began at the half year mark after the collapse of the corresponding ice shelf (i.e. 1995.5 for Prince Gustav and Larsen A glaciers, and 2002.5 for Larsen B glaciers), and continued to present-day (2013.0). For the Larsen B glaciers this is justified, as Scambos et

al. (2004) show glacier acceleration and thinning commenced a few months after ice shelf collapse.

2. It was assumed that observed mass changes for the northerly regions (glaciers feeding the former Prince Gustav and Larsen A ice shelves) are representative of ice-mass loss from 1995.5 to the present-day, and that the mass loss occurs at the same rate for this time period. There is evidence that these glaciers reached their current velocities within a few years of the breakup in 1995 (Rott et al., 2008), and this velocity has been maintained 15 years after ice shelf collapse (Rott et al., 2011). Observations of the glaciers feeding the more southern former Wordie Ice Shelf (Wendt et al., 2010), which disintegrated in a series of events between 1966 and 1989, also suggest that high rates of mass loss are sustained over decades.
3. It was assumed that the Larsen B tributary glaciers were not losing significant mass before 2002.5 and these discs were set to zero change between 1995.5 and 2002.5 accordingly.
4. Any elevation changes that occurred away from former ice shelf regions were assumed to be part of a multi-decadal trend and associated mass changes were applied for the full modelling period. These were generally small and have little effect on the modelling. Although widespread glacier retreat is seen on the western Peninsula (Pritchard and Vaughan, 2007; Cook et al., 2005), thinning appears to be generally limited to a small section at the front of the glaciers and, importantly for this study, the pattern is changing relatively slowly with time (Kunz et al., 2012).
5. Ice history before 1995 was not modelled, but any ongoing deformation related to ice-mass changes before this time was taken into account by estimating a linear background rate from the Palmer GPS observations (see Section 4.3.1). This assumes that the uplift rate was linear prior to these recent changes.

4.3 Modelling

4.3.1 Elastic Modelling

The elastic uplift was computed with the elastic component of the software VE-HresV2 (see Section 2.2.2) (Barletta and Bordoni, in prep.; Barletta et al., 2006). Load Love numbers, based on the PREM Earth structure (Dziewonski and Anderson, 1981), were computed up to a maximum spherical harmonic degree of 3700 using VE-CL0V3RS

v1.4 (see Section 2.2.2) (Barletta and Bordoni, in prep.). It is assumed that after the maximum degree the elastic Love numbers become asymptotic so the solution does not suffer from effects of truncation. The software implementing the High Resolution technique can therefore capture the loading concentrated on glaciers a few km wide (Barletta et al., 2006).

A time series of modelled elastic uplift was computed at the location of Palmer and compared with the GPS observations (Figure 4.5). As the GPS observations are recorded relative to an arbitrary reference height and the model output is relative to zero uplift at the start of the modelled time period, the GPS observations have been offset accordingly based on their pre-2002 mean. To account for the effects of centennial- or millennial-scale glacial isostatic adjustment in the GPS record, a 'background' vertical rate was estimated by subtracting the modelled elastic uplift rate from the GPS uplift rate over the linear part of the Palmer record (1998-2002). This gives the uplift rate due to any ice-mass changes prior to the start of the ice loading model, assuming an elastic-only response to post-1995 events. This rate was then included in the model-predicted time series so that model output could be directly compared with GPS observations.

4.3.2 Viscoelastic Modelling

The viscous uplift of the Earth in response to the ice-mass loss was computed using the viscous component of the software VE-HresV2 (described in Section 2.2.2), which uses VE-CL0V3RS v1.4 to compute load Love numbers up to degree 1195. At higher degrees it is assumed that the Love numbers tend to zero and therefore the combined Green's function is negligible. The maximum degree was chosen so that the results do not suffer from effects of truncation and all viscous response is captured at lower degrees. This study is limited to a Maxwell rheological model. It is worth noting that models with alternative and more complex rheologies may also sufficiently explain the observations, however at present the dataset is too sparse to resolve or require them.

A four-layer viscosity structure is adopted consisting of an elastic lithosphere, and a viscoelastic upper mantle, transition zone and lower mantle, as shown in Table 4.2. The density structure of the model consists of 31 finer layers with densities from the PREM Earth structure (Dziewonski and Anderson, 1981). A simple four-layer viscosity model was chosen as the limited data do not allow a more complex model to be resolved. This is discussed further in Section 4.5.4.

	Depth to base (km)	Viscosity (Pa s)
Lithosphere	**20 - 160**	1×10^{51}
Upper Mantle	400	**1×10^{17} - 1×10^{20}**
Transition Zone	670	4×10^{20}
Lower Mantle	-	1×10^{22}

Table 4.2: Earth Model parameters, with those that have been varied underlined.

To search for the range of plausible best-fit Earth models the lithospheric thickness was varied between 20 and 160 km, and the upper mantle viscosity between 1×10^{17} and 1×10^{20} Pa s. Given that Simms et al. (2012) suggest a value of 1-2 $\times 10^{18}$ Pa s for the South Shetland Islands, which lie closer to the active subduction zone than the study region, and typical values of mantle viscosity proposed for Patagonia, Iceland, or Alaska are in the range 1-10 $\times 10^{18}$ Pa s (Lange et al., 2014; Auriac et al., 2013; Sato et al., 2011), mantle viscosities below 1×10^{17} Pa s are not thought to be physically realistic for this region of the Earth. All other parameters remained fixed. Below the upper mantle layer is a transition zone between 400 and 670 km depth with a fixed viscosity of 4×10^{20} Pa s, as suggested by Sato et al. (2011) in their study of the Earth's response to ice-mass change in Alaska; and below this, a lower mantle with a fixed viscosity of 1×10^{22} Pa s. Sensitivity to different mantle layer thicknesses and a more complex Earth structure is discussed in Section 4.5.4.

4.3.3 GPS Constraints

The uplift time series output from the viscous model were added to the modelled elastic uplift and the background rate, which was recalculated as described in Section 4.3.1, this time by subtracting the modelled viscoelastic uplift rate from the GPS uplift rate between 1998 and 2002. The resulting uplift time series for each Earth model in the parameter space was then compared, first of all, with the Palmer GPS observations only. In order to determine the range of Earth models consistent with the GPS data, the root mean square (RMS) misfit between the modelled uplift and the GPS uplift was calculated and is shown in Figure 4.6.

In an attempt to place further constraints on the range of well-fitting Earth models, the viscoelastic modelling was repeated to calculate uplift at the six LARISSA GPS locations (Figure 4.1) for the full range of Earth models. By assuming that any lateral changes in Earth structure are minimal over the distance spanned by the GPS stations (a

maximum of 300 km), all sites can be used as constraints on a 1-D Earth model. The RMS misfit was computed again by comparing the model-predicted uplift (viscoelastic + background) with the GPS-observed uplift at all seven stations. When computing the modelled time series at the LARISSA stations, which were not occupied prior to the Larsen B break-up, it was assumed that the background rate previously calculated for Palmer was representative of the whole region. That is, a spatially constant background rate across all seven GPS sites was assumed; this is supported by the closeness of fit of the initial Palmer-constrained model to most of the LARISSA sites (residual uplift rates in Table 4.3). This assumption implies that the sites would have been uplifting at lower rates prior to 2002 and the time series would be non-linear, similar to that observed at Palmer. The implications of assuming a spatially-constant background rate are discussed later in Section 4.5.2. Geologic constraints on the background uplift rate, such as from marine limits and deglacial chronologies, were not included as most sites (but not all) lack evidence suitable for long-term estimates of glacial isostatic adjustment.

Site	GPS Observed Uplift (mm/yr)	Elastic Modelled Uplift (mm/yr)	Viscoelastic Modelled Uplift (mm/yr)	Residual (GPS minus viscoelastic model) (mm/yr)
PALM	6.6 ± 2.1 (2009.0-2013.0 only)	1.5	7.9	-1.3
CAPF	4.5 ± 2.9	0.4	7.3	-2.8
DUPT	12.8 ± 2.1	1.7	10.4	2.4
FONP	14.9 ± 2.7	6.7	16.4	-1.5
HUGO	1.7 ± 3.3	-0.4	2.8	-1.1
ROBI	7.8 ± 2.9	1.0	9.8	-2.0
VNAD	5.8 ± 2.4	0.01	5.9	-0.1

Table 4.3: GPS-observed uplift velocities with 2-sigma error; model-predicted uplift velocities for the elastic only model and the best-fitting viscoelastic model from Figure 4.6a. Both model-predicted uplift velocities include the estimated background rate. Last column shows the residual between observed and modelled viscoelastic uplift.

4.4 Results

4.4.1 Elastic Modelling

The Palmer GPS record displays significant non-linearity after 2002; however, the results of the elastic modelling (Figure 4.5) show that even within the uncertainty bounds of the ice-mass change data (±1 m/yr), these changes in rate cannot be explained

by elastic uplift only. In fact, more than five times the amount of observed mass loss (i.e. five times the mass loss shown in Figure 4.4, applied to each disc) would be required to reproduce the magnitude of the observed uplift (modelled uplift shown by the green line in Figure 4.5). This is not plausible and could not be caused by missing ice unloading in the model, as the missing mass would not only need to be large, or be very close to Palmer, but also sustained from 2002 to present. Such a large signal would require a major ice shelf collapse or substantial glacier mass loss adjacent to Palmer and neither scenario exists. In summary, less than half of the rapid increase in uplift at Palmer can be accounted for by elastic rebound.

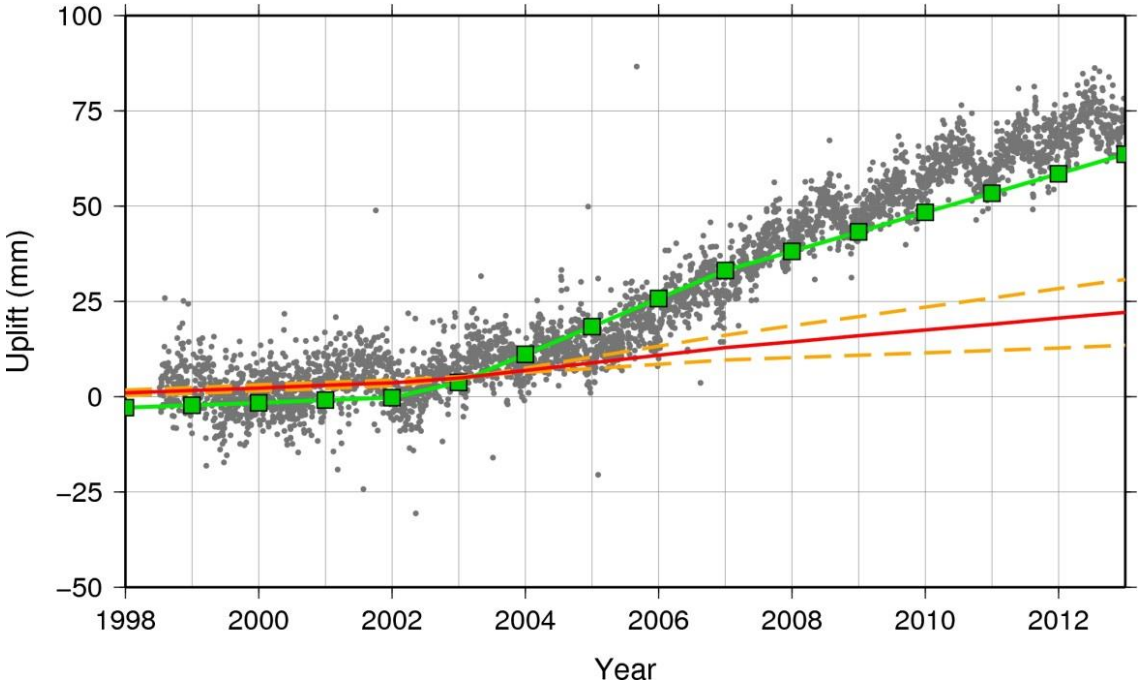

Figure 4.5: Palmer GPS observations (grey dots) compared with uplift time series predicted by the elastic model (red line). Predicted elastic uplift time series for upper and lower bounds on ice-mass loss is shown by the orange dashed lines; and predicted uplift time series assuming 5 times the observed ice-mass loss is shown by the green line with squares.

4.4.2 Viscoelastic Modelling Constrained by PALM

The RMS misfit between the modelled uplift and the Palmer GPS uplift is shown in Figure 4.6a. The best-fitting Earth models, lying within the 95% confidence limit of observational residuals, have a lithospheric thickness in the range 20-160 km and an upper mantle viscosity in the range 1×10^{17} - 2×10^{18} Pa s. There is some trade-off between the two parameters, with thicker lithosphere models accompanying a lower viscosity mantle and vice versa. The Earth model with the lowest RMS misfit (4.67 mm) has values of 130 km and 7×10^{17} Pa s. Computing the RMS again with a shortened time series ending in 2011 to coincide with the ice-mass change data, results

in a best-fitting model with a lithospheric thickness of 20 km. There is a possible offset in the Palmer time series during 1999 and only using data after this time (and recomputing the background rate appropriately) results in a best-fitting model with a lithospheric thickness of 30 km. This highlights that the lithospheric thickness is poorly constrained, although the upper mantle viscosity is robustly found to be less than 2×10^{18} Pa s in all cases.

For the Earth model with lowest RMS misfit to the Palmer time series, the model-predicted velocities at all GPS sites are compared with observed velocities (Table 4.3). The model over-predicts uplift at CAPF by 2.8 mm/yr (compared with a 2-sigma uncertainty of 2.9 mm/yr) and under-predicts uplift at DUPT by 2.4 mm/yr, which is the only significant residual, but the misfit here is only ~23% of the modelled uplift. The model performs well at the other four LARISSA sites with misfits in uplift rate <2 mm/yr and within the 2-sigma observational error.

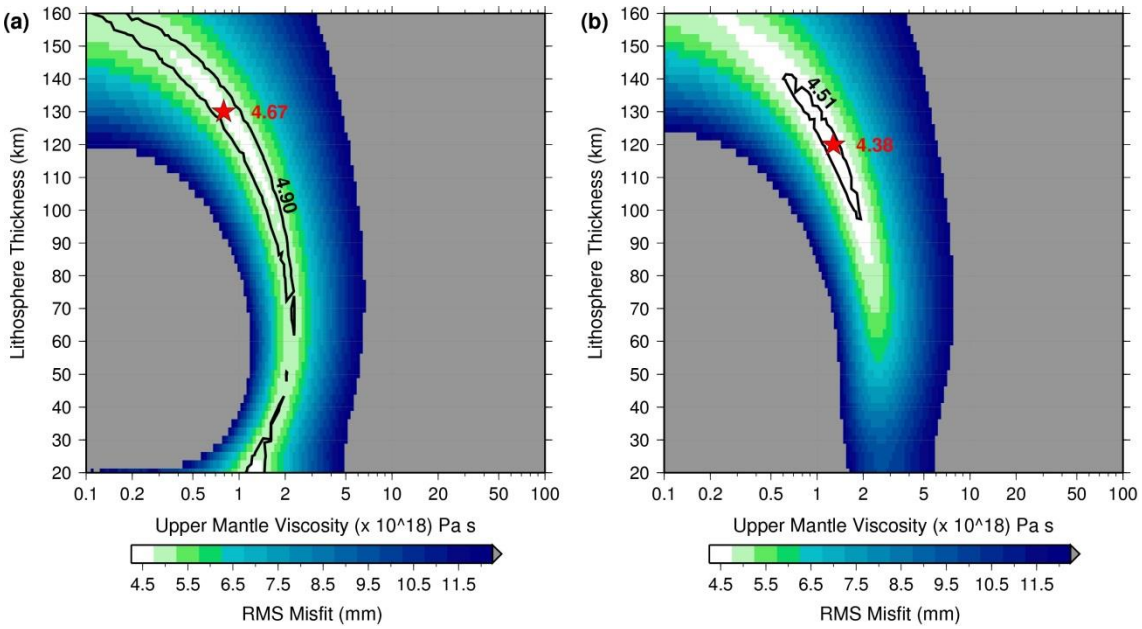

Figure 4.6: RMS misfit between modelled viscoelastic uplift time series and GPS time series for a) Palmer only, and b) Palmer and all stations of the LARISSA network. The 95% confidence limit is plotted as a solid black line, and the best-fit Earth model in each case is plotted as a red star.

4.4.3 Viscoelastic Modelling Constrained with all GPS Records

Constraining the Earth model using uplift data from only one GPS location results in an upper mantle viscosity that is relatively well constrained, but with a broad range of acceptable values of lithospheric thickness. Figure 4.6b shows the RMS misfit between modelled uplift and the GPS-observed uplift for all sites. When using all the GPS data to constrain the Earth models, the range of lithospheric thickness for the best-fitting

models narrows to 100-140 km and the acceptable range of upper mantle viscosity narrows to 6×10^{17} - 2×10^{18} Pa s, as indicated by the 95% confidence limit. The Earth model with the lowest RMS misfit (4.38 mm) has values of 120 km and 1×10^{18} Pa s.

The model-predicted time series for the best-fitting Earth models in Figure 4.6a and b are plotted against the GPS time series in Figure 4.7. For comparison, predicted time series using the "VM2" Earth model, the viscosity structure which accompanies the global ICE-5G GIA model (Peltier, 2004) (see also Section 2.3.1), are also plotted, along with time series calculated using an Earth model within the ranges suggested by Ivins et al. (2011) (an incompressible model as used in Ivins et al. (2011) with 40 km lithosphere and 3×10^{19} Pa s upper mantle viscosity). There is little difference between the two best-fit models from Figure 4.6, whereas both VM2 and the Ivins et al. (2011) model under-predict uplift at all GPS locations. The uplift predicted by the VM2 and Ivins models is dominated by the elastic part of the signal, and the viscous contribution is small. For example, at FONP the viscous part of the total uplift at 2013.0 is 22 mm for the Ivins et al. (2011) model, and only 1 mm for VM2, compared with 123-130 mm for the best-fitting models.

Model-predicted uplift is also compared with GPS records at two further locations: SPPT Figure 4.8 and OHI2 Figure 4.9, which was not corrected for any offsets in the time series. The model-predicted uplift gives a good fit to the observations at SPPT, however the observed uplift at OHI2, much further north (Figure 4.4), cannot be reproduced by the model. This is discussed further in Section 4.5.3.

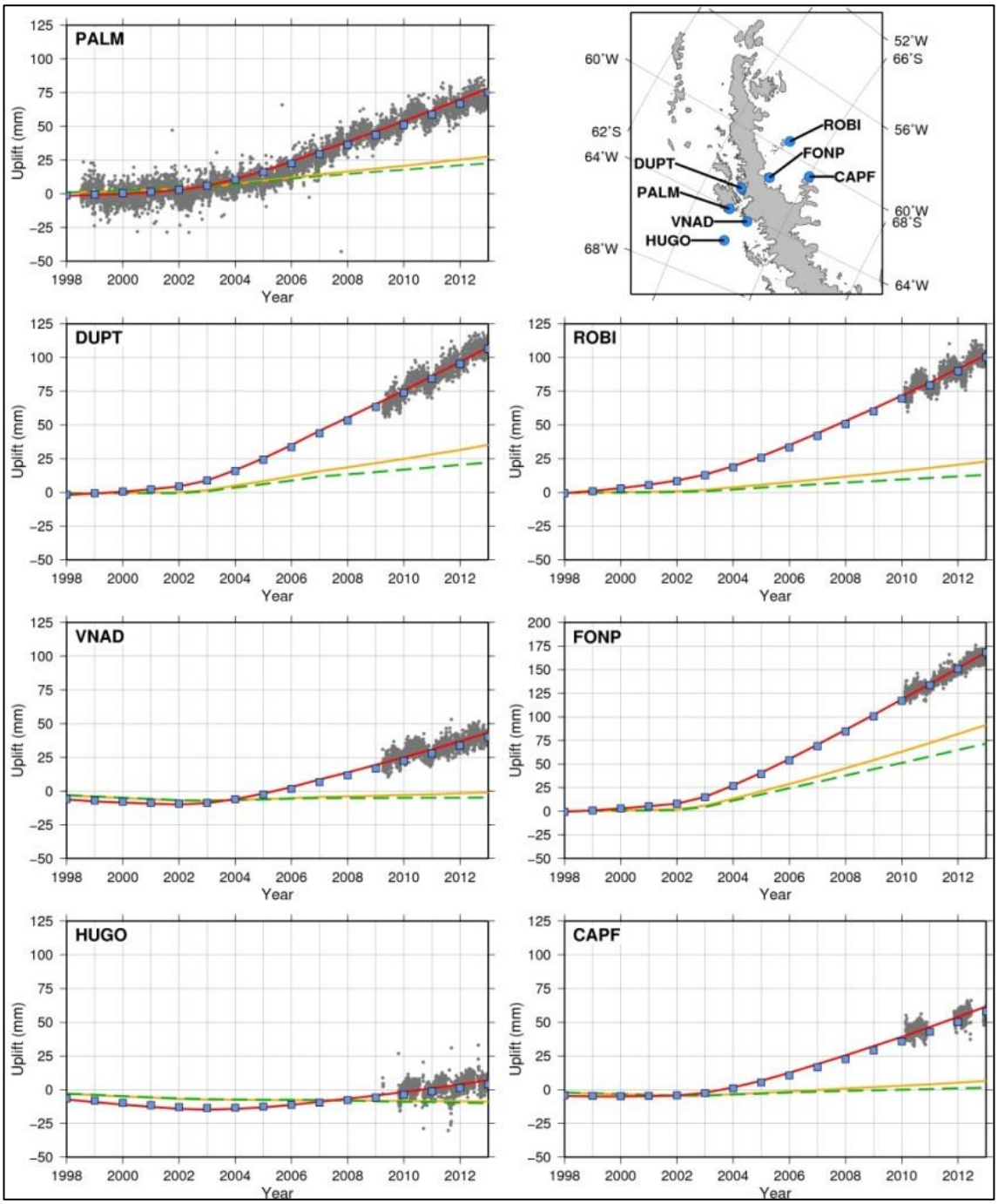

Figure 4.7: GPS observations (grey dots) and model-predicted uplift time series at each GPS location for: the best-fitting viscoelastic Earth model in Figure 4.6a (red line), the best-fitting viscoelastic Earth model in Figure 4.6b (blue squares), the Ivins et al. (2011) viscoelastic Earth model (orange line), and the VM2 viscoelastic Earth model (green dashed line). Map shows GPS locations.

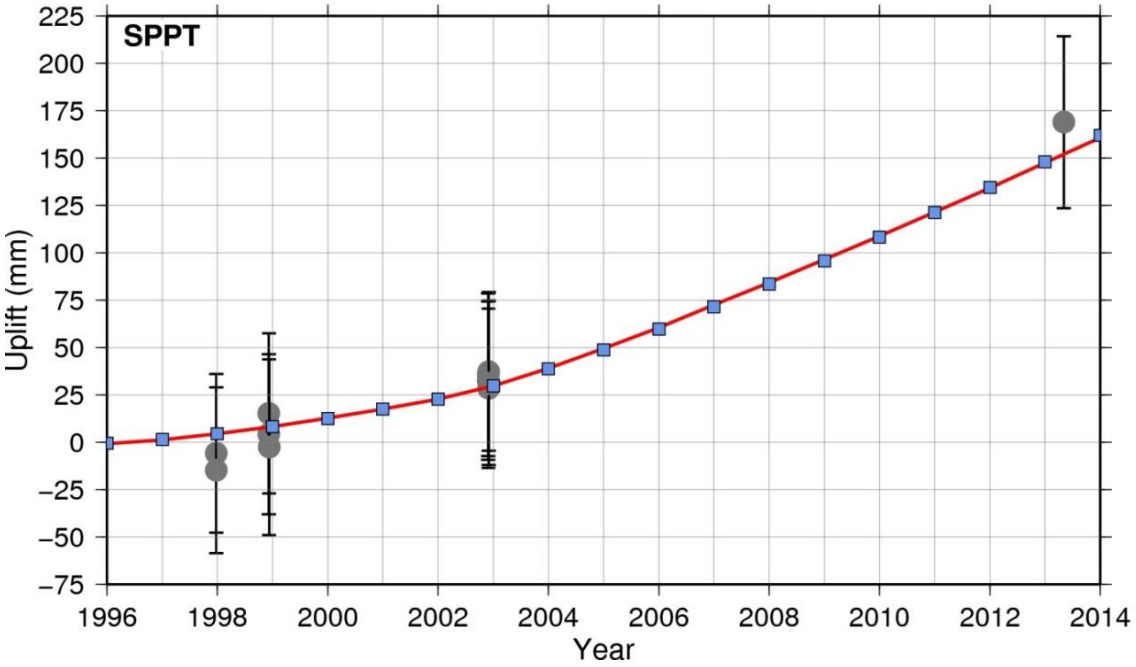

Figure 4.8: Campaign GPS observations (grey dots) with error bars and model-predicted uplift time series at Spring Point (SPPT) for the best-fitting viscoelastic Earth model in Fig. 3a (red line) and the best-fitting viscoelastic Earth model in Fig. 3b (blue squares). The model-predicted uplift includes the background rate derived from Palmer. Note that the Spring Point time series was not used to constrain the Earth model.

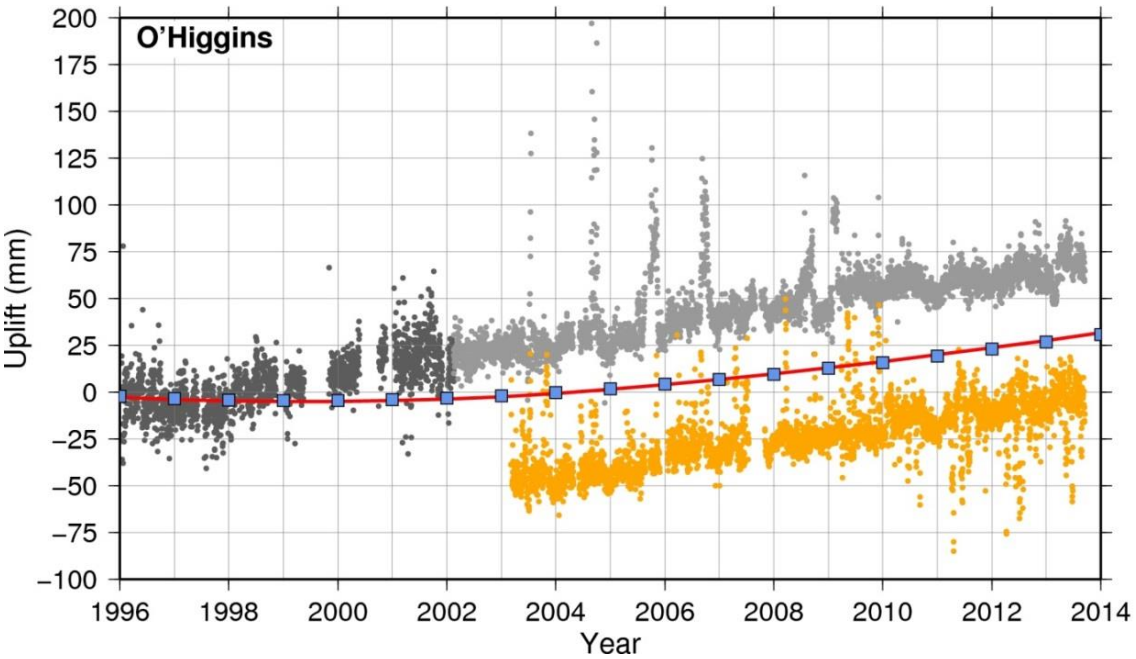

Figure 4.9: GPS observations (dots) and model-predicted uplift time series at O'Higgins for the best-fitting viscoelastic Earth model in Figure 4.6a (red line) and the best-fitting viscoelastic Earth model in Figure 4.6b (blue squares). The model-predicted uplift includes the background rate derived from Palmer. The O'Higgins GPS time series is made up of OHIG (dark grey dots), and its replacement antenna OHI2 (light grey dots). OHI3, from the adjacent station, is also shown (offset) in the orange dots. Note that the O'Higgins time series was not used to constrain the Earth model.

The spatial distribution of model-predicted uplift rates (estimated over the same time period as the GPS-observed uplift rate, i.e. 2009.0-2013.0) for the elastic and viscous components are shown in Figure 4.10a and b, respectively, the latter based on the best-fitting Earth model from Figure 4.6b, as constrained by all seven GPS sites. Figure 4.10c shows the sum of panels a and b and represents the viscoelastic uplift rates including the uniform background rate, with GPS uplift rates over-plotted (as per Table 4.1). The observed GPS uplift rates are well reproduced by the model.

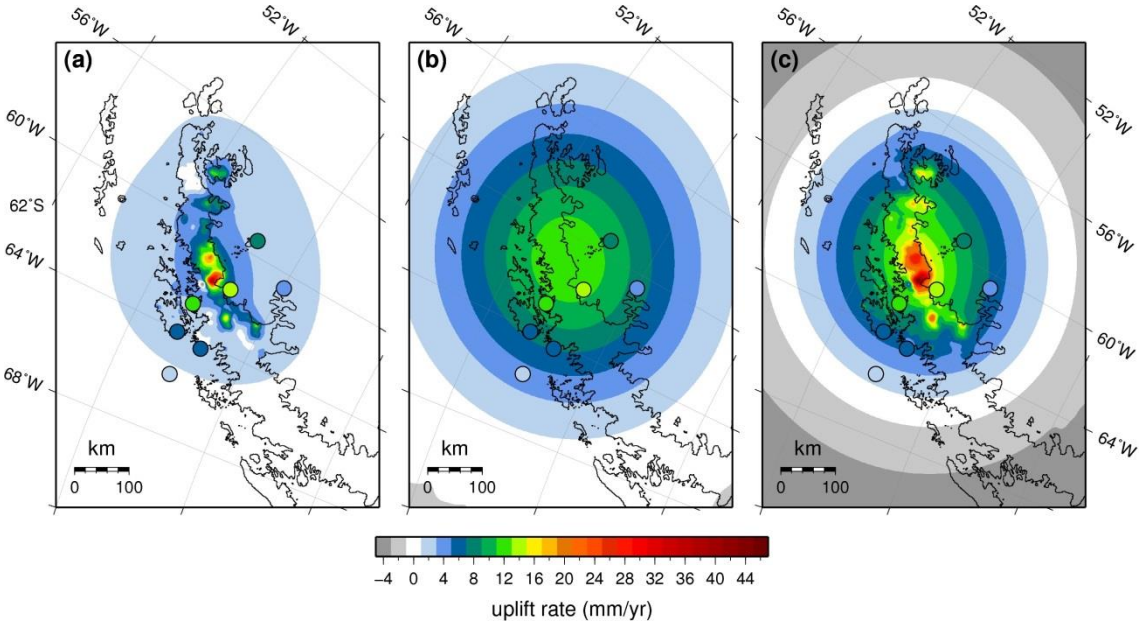

Figure 4.10: Uplift rates at 2011 for the best-fitting viscoelastic Earth model in Figure 4.6b; (a) elastic only, (b) viscous only, and (c) combined viscoelastic and background rate. Post-2009 GPS uplift rates are plotted as circles using the same colour scale.

4.5 Discussion

4.5.1 Earth Model

A range of Earth models for the NAP has been constrained using the ice-mass change dataset and observations from seven GPS stations. First, Palmer station was used to constrain the Earth model finding a poorly constrained lithospheric thickness and an upper mantle viscosity less than 2×10^{18} Pa s. The addition of the six LARISSA GPS sites narrows the overall range of best-fitting Earth models to a lithospheric thickness between 100 km and 140 km and upper mantle viscosity in the range 6×10^{17} - 2×10^{18} Pa s.

The Earth model with minimum RMS misfit in both cases (Figure 4.6a and b) has a thick lithosphere (120-130 km) and a low upper mantle viscosity (7×10^{17} - 1×10^{18} Pa s). However, it is important to note that the solution is non-unique and

within the 95% confidence limit the RMS misfit varies by less than 1 mm, so any model within this limit can provide a reasonable fit to the data. The combination of thick lithosphere and low upper mantle viscosity is somewhat unexpected, as low viscosity regions are commonly accompanied by a thinner lithosphere (Lange et al., 2014; e.g. Auriac et al., 2013; Simms et al., 2012). However, as described in Section 4.4.2, computing the RMS misfit to Palmer using only pre-2011 data gives a best-fitting lithospheric thickness of 20 km, which highlights the poor sensitivity to lithospheric thickness. Similarly, when discounting data before 1999.5, which may be affected by a possible offset in the Palmer time series at 1999.5, the best-fitting lithospheric thickness is reduced to 30 km. In contrast, an upper mantle viscosity of less than 2×10^{18} Pa s (the upper limit of the 95% confidence interval) is required to fit the available data in all scenarios and is a robust finding. Furthermore, comparing the best-fitting model-predicted uplift with campaign GPS observations between 1997 and 2013 at the location of Spring Point, which were not included as constraints on the model, shows a qualitatively good fit and strengthens these conclusions (Figure 4.8).

The range of Earth models predicted here is different to those determined by Ivins et al. (2011) for a larger region encompassing the NAP. Figure 4.7 reveals that the Ivins et al. (2011) Earth model, when combined with post-1995 ice unloading, cannot explain the rapid uplift at Palmer since 2002. There are a number of possible reasons for this. First, Ivins et al. (2011) considered a single Earth model for an area approximately three times larger than the study region considered here, and hence their model is an average for this wider region. Second, the ice unloading scenarios considered by Ivins et al. (2011) are based on relatively few observations and their Earth model may be compensating for ice load errors in poorly constrained regions. Third, Ivins et al. (2011) were limited in their ability to consider the non-linearity in the Palmer record, as their analysis required them to combine it with the GRACE time series which started after 2002, and therefore they treated it as a single linear rate over the post-2002 data period. Finally, it needs to be verified if the Earth model predicted here could satisfactorily fit the observations of the kind used by Ivins et al. (2011); if it cannot, then this may be an indication that a more complex rheological model should be considered, such as one that exhibits non-linear creep (e.g. Ivins and Sammis, 1996).

The peak uplift predicted by the best-fit Earth model is 47 mm/yr located in the Hektoria/Green glacier basin (Figure 4.10), corresponding to the geographical location of the largest mass loss (Berthier et al., 2012). The peak uplift is dominated by the

elastic signal and has a small spatial extent, diminishing to 30 mm/yr or less within ~30 km. The nearest GPS site is located at Foyn Point (FONP), ~40 km away, where the observed uplift rate of 14.9 ± 2.7 mm/yr agrees well with the 16.4 mm/yr predicted by the model. Predicted rates may differ from the true uplift for parts of the model domain if the long-term background uplift rate is substantially different to the spatially constant term adopted here; however, the closeness of the fit between the LARISSA GPS data and model predictions suggests this first approximation is reasonable.

4.5.2 Sensitivity to Background Rate

In the first instance, Palmer station alone was used to constrain the Earth model, as the background uplift rate due to long-term glacial isostatic adjustment is well constrained by the pre-2002 data, available only at this site. Applying a uniform background rate for the whole region may introduce some error in these results if the signal is in fact spatially variable, as indicated by the work in Chapter 3. Nonetheless, using the LARISSA GPS data provides some verification for the inferences from the Palmer dataset. To test the sensitivity to a spatially constant background rate, a new background rate was computed based on that estimated from Palmer, but scaled at the other GPS locations according to the spatial pattern of the W12a Antarctic GIA model (Whitehouse et al., 2012b) (Section 2.3.2). Computing the RMS again for all GPS sites does not change the best-fitting model and reduces the minimum RMS misfit by only 0.01 mm, giving further confidence in the results.

4.5.3 Lateral Variations in Earth Structure

In using a 1-D symmetric Earth model the effects of lateral heterogeneity in Earth structure are not considered in the modelling. The long-term tectonic history of the region suggests that there may be a gradient in Earth structure along the length of the Peninsula (Barker, 2001; Larter et al., 1997). This is supported by the recent study of Simms et al. (2012) who predict a thinner lithosphere (15km) for the South Shetland Islands, which lie 100 km off the northern tip of the AP. At present there is insufficient data to constrain a 3-D Earth model. Due to the likely lateral variations in Earth structure, any GPS data far from the site of largest ice loss were not included as constraints (e.g. O'Higgins which lies 300 km to the north, OHI2 in Figure 4.4). A comparison of the model-predicted uplift to the GPS observations (Figure 4.9) shows that the linear uplift recorded at O'Higgins cannot be explained by the model results, both in terms of the magnitude of uplift and linearity of the time series. This is likely

due to a combination of increased uncertainty in ice unloading near to O'Higgins over 1995-2001, the different Earth structure and the assumption of a spatially constant background rate.

The Earth models inferred here show that the NAP cannot successfully be modelled as part of a continent-wide GIA model, as the Earth structure is too different from that traditionally used for the rest of Antarctica (e.g., Whitehouse et al., 2012b). This work has important implications for forthcoming GIA models which incorporate 3-D Earth structure, and it identifies a location where upper Earth structure may be constrained by observations.

4.5.4 Sensitivity to a Complex Earth Structure

The GPS observations can be explained reasonably well by a simple four-layer viscous model, in which only the lithospheric thickness and upper mantle viscosity parameters were varied. The depth over which the load induces mantle flow was tested by decreasing the depth of the modelled upper mantle-transition zone boundary to 350 km. The RMS of the two best-fit models increased by 6-11% suggesting that mantle flow occurs to at least this depth. Increasing or decreasing the transition zone viscosity by an order of magnitude made less than 1% difference to the RMS for each best-fit model. Consequently, the results are not sensitive to changes in Earth model parameters below 400 km depth due to the small spatial extent of the load and observations. Therefore the implications of an Earth model with a more complex structure in the top 400 km are considered.

Several studies that have used a more complex Earth structure include a low viscosity zone (LVZ) directly beneath the elastic lithosphere (e.g., Sato et al., 2011). Sensitivity tests were performed to investigate whether such a model could provide a better fit to the data. Again the lithospheric thickness and upper mantle viscosity were varied to determine the best-fitting Earth model, but this time the Earth model also included a low viscosity zone with a fixed thickness and a viscosity proportional to that of the upper mantle viscosity. Two thicknesses of the LVZ were tested (100 km and 200 km), along with several different ratios of LVZ viscosity to upper mantle viscosity (1:5, 1:10, 1:20; six experiments in total).

Compared with the best-fitting Earth model in Figure 4.4b, the best fit for each of the six experiments generally has a thinner lithosphere by up to 15 km, and a fairly

consistent LVZ viscosity in the range 3-8 × 10^{17} Pa s. The upper mantle viscosity was found to be much higher than the 1 × 10^{18} Pa s found previously which shows some trade-off between these layers, with the higher viscosities compensating for the lower LVZ values. Whilst these more complex structures can provide alternative and equally plausible Earth models that explain the data, the minimum RMS misfit did not change by more than 1% for any of the experiments, demonstrating that a significantly better fit to the data could not be achieved. In the future a more spatially extensive GPS network might enable a more complex Earth structure and lateral variations to be resolved and this network expansion is currently underway as an extension of the LARISSA project, with a permanent site now installed at Spring Point and a further deployment scheduled for 2014.

4.5.5 Sensitivity to Ice Model Uncertainties

As described in Section 4.2.2, ice-mass change was modelled over a longer time period than is covered by the elevation change data by linearly extrapolating a constant rate of ice loss backwards and forwards in time from a few months after ice shelf break up to the present day, with no ramp up of mass change included. Studies have suggested that glaciers in the NAP that have accelerated following an ice shelf collapse remain at elevated speeds for decades. Rott et al. (2008) showed that Drygalski glacier, feeding the former Larsen A Ice Shelf, did not accelerate between 1999 and 2007, and Rott et al. (2011) state that the increased velocity of the Larsen A and Prince Gustav glaciers has so far been maintained 15 years after ice shelf collapse. The uncertainties in the ice loading model therefore relate to how quickly Larsen B glaciers accelerated to reach the 2002-2006 rates (Figure 4.4b), and the acceleration history of Larsen A and Prince Gustav glaciers between 1995 and 1999.

To investigate this a sensitivity study was performed to simulate acceleration of the glaciers in the ice loading model – linearly increasing the rate of mass loss from 0 m_{weq}/yr at the time of ice shelf collapse, to full rates (as shown in Figure 4.4) one year later for Larsen B and Larsen A/Prince Gustav glaciers separately. For Larsen B glaciers this ramp up scenario of ice-mass loss improved the RMS misfit by less than 2%. Although the parameters of the best-fitting model changed slightly – the lithospheric thickness increased by 5 km, and upper mantle viscosity decreased slightly – the overall range of best-fitting Earth models remaining the same. For Larsen A and Prince Gustav glaciers, ramping up of the mass-loss had a negligible effect on the results, and the RMS

and best-fitting models remained the same. This confirms that the effect of errors in the ice loading assumptions is small.

4.5.6 Elastic Effects of Surface Mass Balance Anomalies

Whilst the model output closely matches the GPS time series overall (Figure 4.7), there are localised misfits. This is likely due to local time variable mass changes which are not included in the ice loading model. It is possible that these fluctuations are caused by an elastic response to variations in SMB over shorter periods of time than the DEMs allow us to resolve and this was investigated.

Using the RACMO2.1/ANT27 dataset of SMB up to 2011.0 (Lenaerts et al., 2012) (Section 2.4.4), the long-term trend between 1979 and the end of 2010 was removed to obtain anomalies to the mean at each grid point, and these were converted to a set of loading discs. The elastic response to the SMB anomalies was calculated at Palmer, and superimposed onto the time series for the best-fit viscoelastic model from Figure 4.6a. This calculation was performed with some caution due to the low resolution of the SMB model (27km) compared with the small valley glaciers that dominate much of this region (Trusel et al., 2013). Nevertheless, Figure 4.11 shows that the additional elastic response improves the fit between the modelled and observed time series and explains much of the short-term variations, which likely reflect seasonal signals and multi-year perturbations in SMB. The RMS misfit, calculated over the shorter time period of the SMB model, reduces marginally from 4.74 mm to 4.56 mm. It is not known how the effect of SMB anomalies could improve the fit at the other GPS sites as the RACMO2.1/ANT27 model output is presently only available up until the end of 2010, providing minimal overlap with the LARISSA time series. A viscous response to SMB load changes would be negligible due to the small and fluctuating nature of the loads.

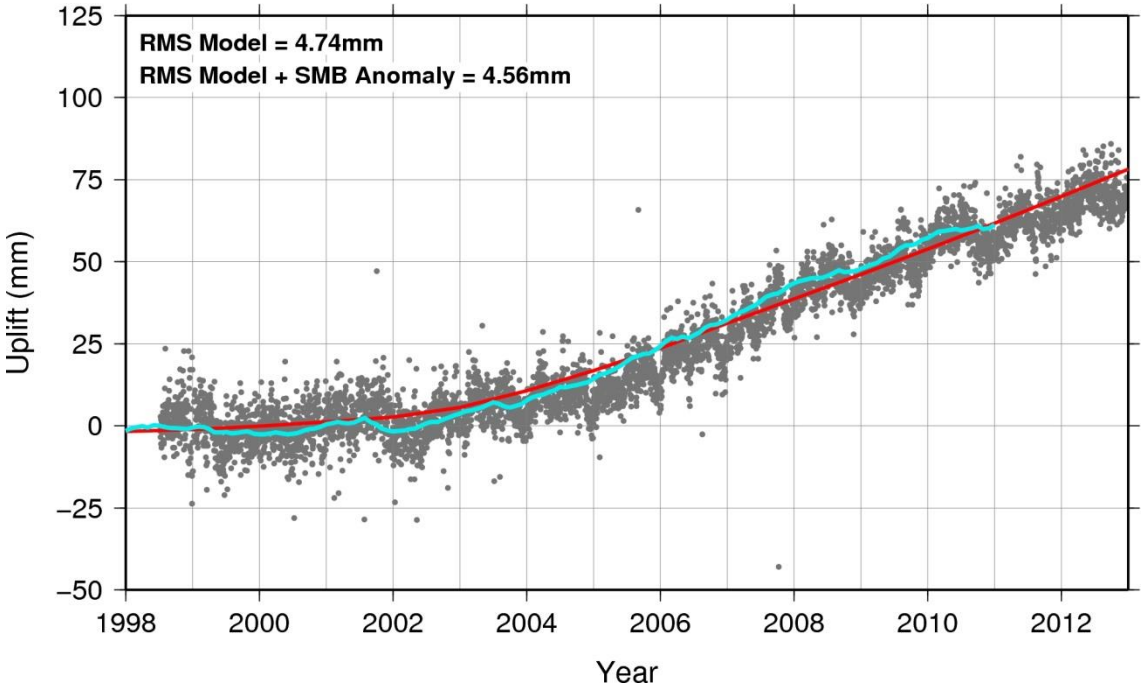

Figure 4.11: Palmer GPS observations (grey dots) and model-predicted uplift time series for the best-fitting Earth model in Figure 4.6a (red line), and the best-fitting Earth model with the addition of the elastic effects of SMB anomalies (pale blue line).

4.6 Conclusions

The breakup of Larsen A, Prince Gustav, and Larsen B ice shelves in 1995 and 2002 led to increased ice-mass loss from the NAP and the solid Earth response can be observed in GPS records. The non-linear uplift observed at Palmer station cannot be explained by an elastic response only, suggesting there is also a viscous response over a short timescale. A linear Maxwell viscoelastic model with a four-layer profile can produce a good fit to the Palmer GPS record, constraining the upper mantle viscosity to less than 2×10^{18} Pa s, but the lithospheric thickness remains poorly constrained. Shorter time series from the six GPS stations of the LARISSA network verify this result, finding a best-fitting Earth model with an upper mantle viscosity of 6×10^{17} - 2×10^{18} Pa s and narrowing the lithospheric thickness to 100-140 km.

The range of values for upper mantle viscosity is much lower than previously suggested for this region but is consistent with the back-arc tectonic setting. A more complex Earth structure, in terms of vertical stratification or lateral variations, could explain the observed data equally well, but additional GPS stations are required to resolve this structure further. Similarly, it is possible that a non-linear rheology could provide an equally good fit to the existing data; however this is not required to explain the existing data.

This work demonstrates that in regions of low upper mantle viscosity and on-going ice-mass change, GPS data cannot be correctly interpreted without considering the viscoelastic response to present-day ice-mass change. Combining the LARISSA time series with the Palmer GPS time series offers a rare opportunity to study the time-evolution of the low-viscosity solid Earth response to a well-captured ice unloading event.

Chapter 5. Late Holocene Ice Loading Changes on the Siple Coast

5.1 Introduction

The Siple Coast region of Antarctica contains many fast-flowing ice streams that transport significant amounts of ice from the interior of West Antarctica to the Ross Ice Shelf. The flow of these ice streams controls the mass balance of the region which is at present considered to be positive (King et al., 2012b; Joughin and Tulaczyk, 2002) due to thickening directly related to ice stream stagnation. Many studies have shown changes in ice stream flow over the past ~1000 years (e.g. Catania et al., 2012; Hulbe and Fahnestock, 2007), where ice streams display century-scale stagnation and reactivation which does not occur synchronously. The ice streams are fast flowing due to the presence of water at the bed and the deformable sediments below. It is thought that stagnation occurs due to an increase in basal resistance related to strengthening of the underlying sediments, which is caused by basal freezing or a decrease in subglacial water pressure (Beem et al., 2014).

The most recent ice stream to stagnate was Kamb Ice Stream (KIS, formerly "Ice Stream C") which stagnated approximately 165 years ago (Retzlaff and Bentley, 1993). ICESat measurements of surface elevation change show that the trunk of KIS is currently thickening by up to 0.6 m/yr (Pritchard et al., 2009) as ice continues to flow into the drainage basin from upstream but no longer flows out (Rignot et al., 2011). GPS observations of neighbouring Whillans Ice Stream (WIS) show it is decelerating and at the long-term (decadal) average rates is expected to stagnate in the next ~50-150 years (Joughin et al., 2005), or possibly sooner if deceleration continues to increase (Beem et al., 2014).

It is not known how the change in ice-sheet thickness related to the stagnation of ice streams on the Siple Coast could affect GIA in this region. Stagnation-related thickening of ice streams may cause an increase in ice-sheet thickness on century scales. Given a sufficient amount of thickening, there may be a GIA-related response depending on the properties of the Earth. Current GIA models neglect ice load changes in Antarctica over the past few thousand years and hence do not include ice thickness changes from ice stream stagnation. GIA models tend to predict a large uplift bulge in this region of 10 mm/yr (Whitehouse et al., 2012b) to 11 mm/yr (Argus et al., 2014), but there are few GPS sites to provide constraints. Furthermore, a recent study by King et

al. (2012b) suggested that the GIA signal in this region should be close to zero and that GIA models over-predict uplift (Section 2.3.2).

The work presented in this chapter investigates the potential perturbations to the present-day GIA signal due to stagnation and reactivation of ice streams, and subsequent thickening and thinning of the ice sheet, over the last ~165 to 2000 years. GIA-related subsidence in response to these processes may explain the discrepancy between GIA model-predicted uplift and GRACE-determined mass change along the Siple Coast (King et al., 2012b). The available observations were used to construct a series of models of stagnation-related thickening on KIS since ~1850 which explore the uncertainties in the timing of stagnation and in the amount of ice that may have built up. Present-day GIA deformation rates were predicted for three ice loading models, the minimum, maximum and best estimate. The best estimate ice loading history for KIS was then combined with the W12 deglacial model (Whitehouse et al., 2012a) and an ensemble of plausible Earth models to investigate the longer term GIA signal in the region. Furthermore, two additional loading scenarios were constructed to investigate stagnation and reactivation cycles of ice streams over the past ~1000-2000 years. The GIA signal was predicted for each of the ice loading histories based on a range of Earth models, and finally, model-predicted GIA was compared with an empirical GIA model (Gunter et al., 2014).

5.2 Ice History and Data

5.2.1 KIS Stagnation

The recent shutdown of KIS is part of a longer term cycle of stagnation and reactivation of ice streams on the Siple Coast. Stagnation is reported to have occurred approximately 165 years ago (Retzlaff and Bentley, 1993) and prior to this, KIS was fast flowing, although the pre-stagnation velocity is uncertain. Ng and Conway (2004) estimate that KIS flowed at an average of 340 m/yr over the 740 years before stagnation. A modelling based study by Hulbe and Fahnestock (2007) used values of 300 and 500 m/yr for lower and upper bound velocities, respectively, for flow ~200 years before stagnation. Approximately 360 years ago, or ~200 years prior to stagnation of KIS, an area known as “Duckfoot” lying on the northern edge of KIS adjacent to the Siple Dome (see Figure 5.1) shut down rapidly (Catania et al., 2012) and this likely took less than 10 years to complete (Catania et al., 2006). Catania et al. (2006) suggest that as a result of this, the trunk of KIS narrowed and consequently slowed to approximately

200 m/yr at the margins, although they note this is likely to be an underestimation of the centreline velocity, before stagnating completely 200 years later.

The timing of stagnation of KIS has been estimated using radar data. Retzlaff and Bentley (1993) describe the acquisition and subsequent analysis of radar data at five profile locations on KIS (see Figure 5.1). The radar data was used to determine timing of stagnation from burial depths of crevasses. A fast-flowing ice stream is heavily crevassed at its surface, however, once it ceases to flow subsequent accumulation buries the crevassed surface. By estimating the burial depth they were able to determine the timing of stagnation at the five profile locations and concluded that KIS stagnated as a wave moving from the grounding line upstream. Stagnation initiated quickly but slowed with time, so the stagnation times at the three profiles closet to the grounding line are indistinguishable from each other. The ice stream took no more than a few decades to stagnate.

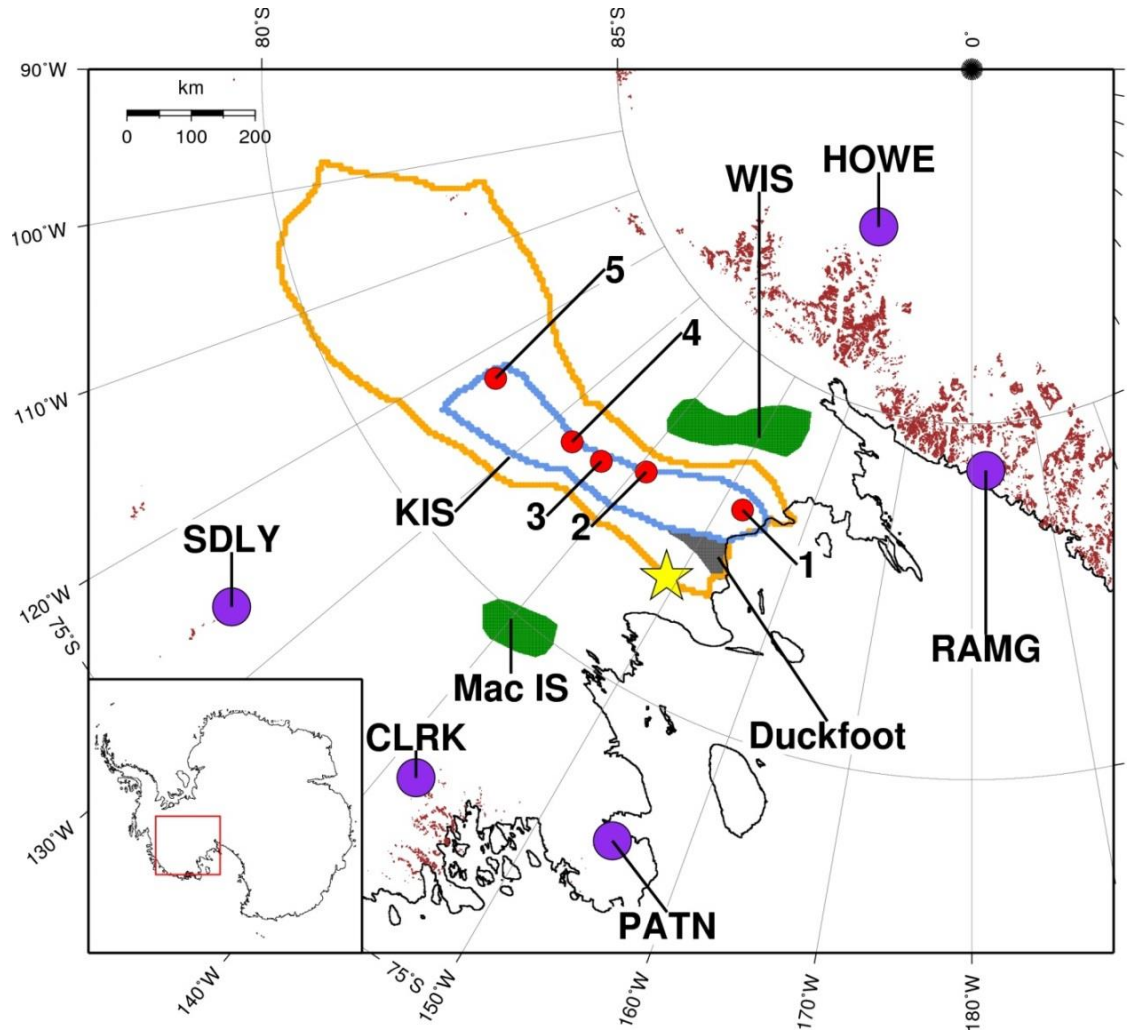

Figure 5.1: Study region with rock outcrops in brown. Profile locations 1-5 from Retzlaff and Bentley (1993) shown as red dots. Masks for the previously fast-flowing KIS (blue outline), the extent of the ice loading calculation (orange outline), and Whillans and MacAyeal (MacIS) ice streams (green shaded areas). GPS locations are shown as purple circles and the location of the Siple Dome ice core is shown as the yellow star. The Duckfoot region is shaded in grey.

5.2.2 Accumulation Data

The Siple Dome ice core drilled around 100 km to the north of KIS (see Figure 5.1) reveals an accumulation history over the past 30 ka (Price et al., 2007). There is a period of variable accumulation rate between approximately 10 ka and 2 ka BP varying by up to 0.04 m/yr, although accumulation appears to remain constant to within 0.01 m/yr during the past 1-2 ka (Figure 2 in Price et al. (2007)). The mean accumulation rate recorded in the Siple Dome ice core between 1890 and 1994 is 0.12 m/yr (water equivalent) (Kaspari et al., 2004). Average accumulation rates over the past few centuries are revealed in a further seven ice cores from the region (Kaspari et al., 2004), as shown in Table 5.1 and Figure 5.2a.

Ice Core	Longitude (°)	Latitude (°)	Time Period	Mean Accumulation Rate (mweq/yr)
00-1	-111.239	-79.383	1653-2001	0.22
00-4	-120.08	-78.083	1799-2000	0.19
00-5	-123.995	-77.683	1716-2000	0.14
99-1	-122.63	-80.62	1724-1998	0.14
RIDS A	-116.33	-78.73	1831-1995	0.24
RIDS B	-118.05	-79.46	1922-1995	0.15
RIDS C	-119.43	-80.01	1903-1995	0.11
Siple Dome	-148.998	-81.653	1890-1994	0.12

Table 5.1: Location and mean accumulation rate in meters water equivalent per year for ice cores near the study region, taken from Kaspari et al. (2004).

For a more recent time period, surface mass balance (SMB) data is available from regional atmospheric climate model RACMO2.1/ANT (Lenaerts et al., 2012). RACMO2.1/ANT provides monthly SMB values between January 1979 and December 2010 on a ~27 km grid (see also Section 2.4.4). The average SMB rate from this dataset was used when calculating the ice loading history (Section 5.3.5) and is shown in Figure 5.2a. It is assumed that the magnitude and spatial pattern of the accumulation rate is constant for the whole time period of the stagnation, a maximum of 192 years, and it is unlikely that large fluctuations in accumulation occurred over this time period. This is justified, as RACMO2.1/ANT model output suggests relatively constant accumulation rates during this period, as shown by the small standard deviation to the mean in Figure 5.2b. Moreover, the accumulation rate recorded in ice cores in the region demonstrates that the long-term average accumulation is within 0.1 m/yr of the RACMO2.1/ANT SMB values (see Table 5.1 and Figure 5.2a).

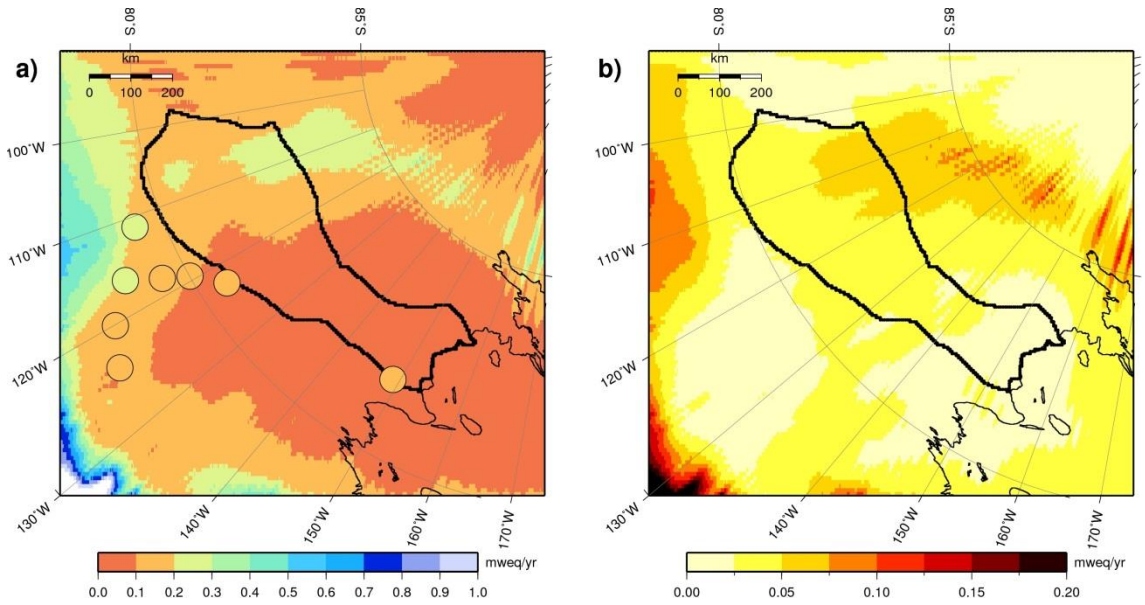

Figure 5.2: a) Mean yearly SMB from RACMO2.1/ANT for the period 1979-2010 in metres water equivalent per year. Mean accumulation from ice cores (see Table 5.1) is shown by the circles on the same colour scale. b) Standard deviation to the mean of yearly SMB over the same period.

5.2.3 Elevation Change

Surface elevation change data is available from ICESat laser altimetry measurements between February 2003 and November 2007 (Pritchard et al., 2009) and is reproduced in Figure 5.3. This dataset shows thickening of up to 0.65 m/yr on the trunk of KIS. More recently, Antarctic surface elevation change has been derived from CryoSat-2 radar altimetry data between November 2010 and September 2013 (McMillan et al., 2014). CryoSat-2 is an improvement over ICESat as it covers a greater area, notably nearer the pole, and has denser measurements in steep terrain and coastal areas (McMillan et al., 2014), although this dataset is unavailable for use in this study.

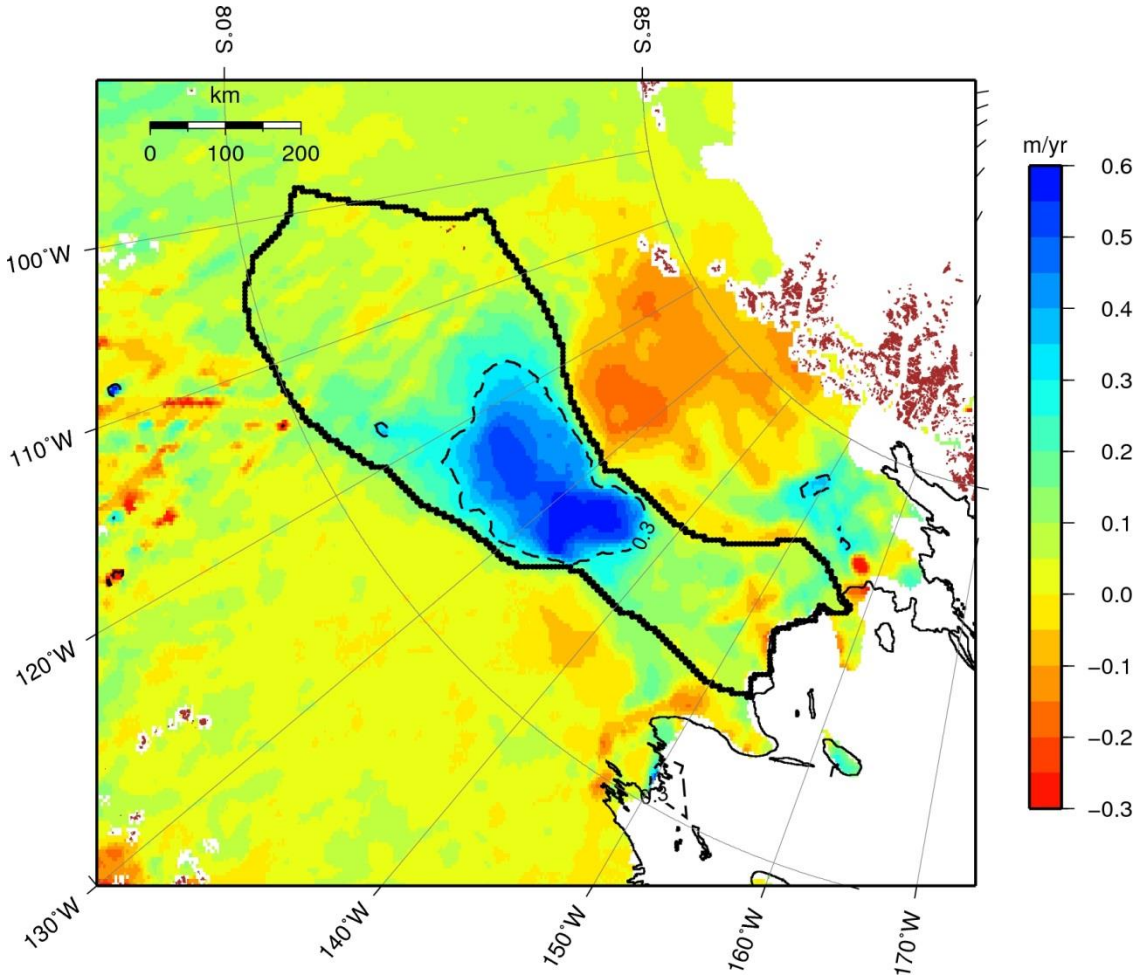

Figure 5.3: Elevation change data from ICESat, adapted from Figure 4 of Pritchard et al. (2009). The extent of the study region is shown by the solid black line, while the dashed contour delineates elevation change higher than 0.3 m/yr.

5.3 Ice Loading History Reconstruction on KIS since ~1850

This section describes how the century-scale ice loading history was calculated for input to the GIA model. An ice-sheet model was not used to generate the loading history due to the limitations of most ice-sheet models in representing ice streams. Instead, a simple approach was used based only on available observations. There are uncertainties associated with the timing of stagnation and the speed at which KIS was flowing prior to stagnation. To take account of these uncertainties, several stagnation histories were constructed to explore the parameter space of the variables. The assumptions and limitations of the method are described in the following sections and discussed further in Section 5.5.1.

5.3.1 Pre-Stagnation Conditions

Prior to stagnation, KIS was fast flowing, but the velocity had decreased slightly due to the stagnation of the Duckfoot region, as described above. The uncertainty in the velocity is taken into account by using several different values that capture the full range of plausible velocities (see Section 5.3.4). It is also assumed that all ice streams in the region are in balance. Whilst this is unlikely, it allows the signal from the KIS stagnation and associated ice build-up to be isolated from any mass changes on the other ice streams.

5.3.2 Timing and Speed of Stagnation

The timing of stagnation has been based on the estimated age of buried crevasses reported by Retzlaff and Bentley (1993). The authors estimate the time of stagnation for the five profiles shown in Figure 5.1, as well as the uncertainty bounds on these timings. They refer to the timing of stagnation as "years ago"; here timings are reported in calendar years, where "years ago" is taken to be the number of years prior to the data collection from that study in 1988. The timings are given in Table 5.2.

Profiles 1-3 located closest to the grounding line have the same estimated age of stagnation, so the uncertainty bounds of ±30 years are used to create three ice loading histories with different timings. The total time it takes for stagnation between the grounding line and profile 5 remains the same for all loading histories, but stagnation commences earlier (upper bound) and later (lower bound) than the best estimate, allowing more or less ice to build up, respectively. The ice history is calculated in one year time steps.

The speed at which stagnation propagates upstream is taken from the distance between the profiles and the timings in Table 5.2. Since Retzlaff and Bentley (1993) report that stagnation occurred rapidly and the first three profiles have the same stagnation age, the rate of stagnation through time is kept the same for all variations of the ice loading history. The speed decreases upstream, as shown in Table 5.2.

Profile	Timing of Stagnation from Retzlaff and Bentley (1993) (Years before 1988)	Timing of Stagnation (calendar years)	Distance from previous profile location (km)	Stagnation Timings			Time taken to stagnate from previous profile location (years)	Speed of stagnation (km/yr)
				Lower Bound (LB)	Best Estimate (BE)	Upper Bound (UB)		
Grounding Line	-	-	-	1863*	1843*	1823*	-	-
1	130 ± 30	1858 ± 30	<=25*	1868	1848	1828†	5*	5*
2	130 ± 30	1858 ± 30	150	1878	1858	1838	10	15
3	130 ± 30	1858 ± 30	100	1888†	1868	1848	10	10
4	100 ± 30	1888 ± 30	60	1900	1880	1860	12	5
5	30-100**	1888-1958	140	1928	1908	1888	28	5

*Values not taken from Retzlaff and Bentley (1993), it is assumed that it took 5 years to stagnate from the grounding line to profile 1, see Section 5.3.5.

**Uncertainty not given.

†LB, BE and UB timings explore the maximum range 1828-1888, because the timing of stagnation is the same for profiles 1-3.

Table 5.2: Timing of stagnation of ~1850 KIS based on information given in Retzlaff and Bentley (1993).

5.3.3 Spatial Extent

When calculating the ice loading history since ~1850, the spatial extent is limited to KIS only. Neighbouring WIS is currently thinning in its upstream areas and thickening near the grounding line (Pritchard et al., 2009), but these present-day changes were not included in this study. Ice streams to the north of KIS appear to be in balance, with present-day elevation change rates less than ±0.1 m/yr, which can be attributed to variations in SMB (McMillan et al., 2014). By limiting the study region to the KIS basin only for the past ~165 years, any GIA-related deformation due to thickening or thinning of neighbouring ice streams will be omitted from the model results. However, this is likely to be minimal as KIS is the only ice stream experiencing significant thickening in the past ~200 years (Catania et al., 2012), and ice-sheet thickness changes on WIS have occurred only recently (Joughin et al., 2005) meaning the GIA-related signal will be small or non-existent. Neighbouring ice streams are included in a longer term (~2000 years) ice loading history, which is discussed later in Section 5.4.6.

The area over which the ice loading history was calculated is shown by the orange outline in Figure 5.1. This outline was created manually by expanding the drainage basin from Rignot et al. (2008) to include the tributaries still flowing into KIS and encompassing the region of present-day thickening shown by Pritchard et al. (2009). The drainage basins derived by Zwally et al. (2012) were also considered but not used as the drainage basin for KIS also includes a part of WIS in that study. The area of pre-stagnation flow was defined based on Figure 3 of Catania et al. (2012), and is shown in blue on Figure 5.1. It is assumed that fast-flowing ice extended upstream to the location of profile 5, which coincides with the extent of fast flow in neighbouring ice streams (Rignot et al., 2011) (see Figure 5.4). It is noted that ice is still flowing into the basin from upstream, and this is discussed in the following Section.

5.3.4 Pre-Stagnation Velocity of KIS

To calculate the build-up of ice due to stagnation of KIS, the velocity before and after stagnation is required. As described in Section 5.2.1, Catania et al. (2006) suggest that in the ~200 years prior to stagnation the ice stream was flowing at ~200 m/yr at the margins, stating that this is likely to be an underestimation of centreline velocity. Three values of pre-stagnation velocity were used in the calculations: 100, 200, and 300 m/yr. 300 m/yr was used as a lower bound velocity in a modelling study undertaken by Hulbe and Fahnestock (2007), which referred to the time before the Duckfoot region stagnated

and KIS was flowing faster. 300 m/yr was therefore taken as the maximum pre-stagnation velocity for KIS as it had already narrowed and slowed as a direct result of Duckfoot stagnation. It is assumed that these values are constant for the whole ice stream and therefore they represent an average value across stream.

It is reported that stagnation of the ice stream occurred quickly (Retzlaff and Bentley, 1993) which is also supported by evidence suggesting the Duckfoot region stagnated in less than 10 years (Catania et al., 2006). It is likely that at a given location the ice stream velocity decreased over a number of years, however, for ease of computations it is assumed that stagnation occurred in one year (one time step). The set of reconstructed loads should capture the full range of loading scenarios due to the conservative bounds used in the calculations, and furthermore, the effect of this assumption on the GIA signal is likely to be negligible. After a section of the ice stream has stagnated, it is assumed that velocity is zero, so that no ice flows downstream of the stagnation.

In the upstream reaches of the ice stream, observations of present-day velocity show that tributaries are still flowing into the trunk of KIS at a velocity of approximately 50 m/yr (Rignot et al., 2011) as shown on Figure 5.4. Ice is flowing up to the location of profile 4, so the ice build-up calculation between profile 4 and 5 is treated differently to the downstream sections (see Section 5.3.5).

All velocities described here are surface velocities and it is not known how ice velocity varies with depth through the ice streams. However, Catania (2006) and Ng and Conway (2004) suggest that KIS flowed as “plug-flow”, meaning the ice velocity is the same at all depths. Due to the deformable sediment and the presence of water at the base of the ice stream it is likely that sliding occurs at the base. Furthermore, Rignot et al. (2011) suggest that basal slip occurs at velocities higher than 15 m/yr, so it is therefore reasonable to assume velocity is constant with depth.

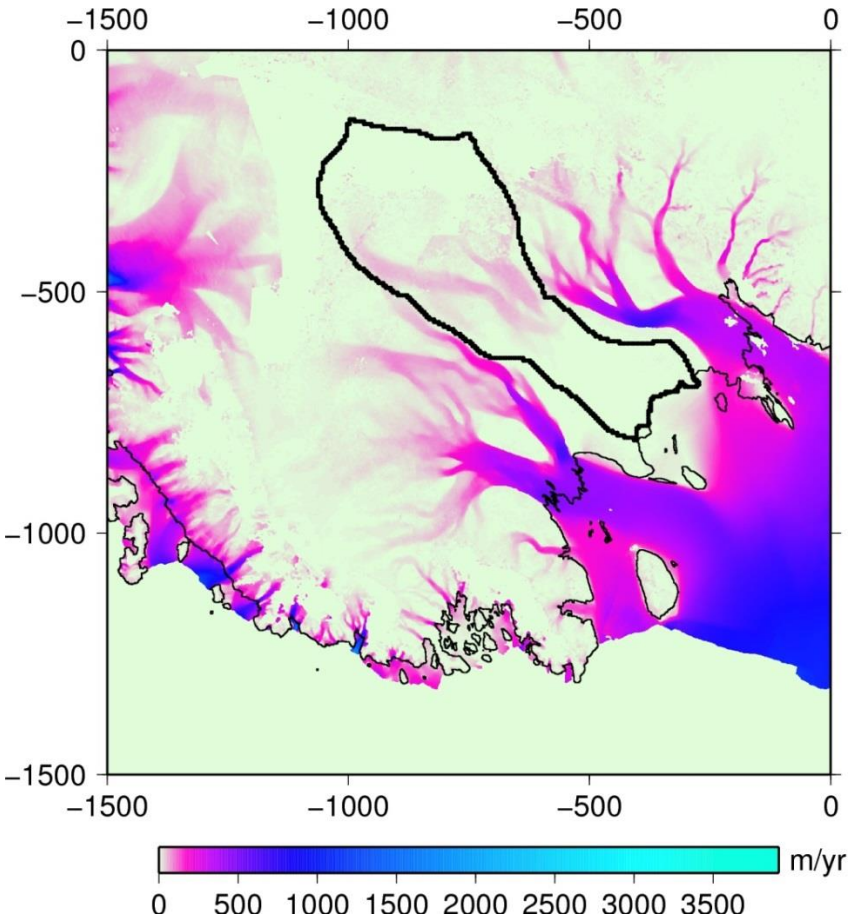

Figure 5.4: Present-day ice velocity adapted from Rignot et al. (2011). The extent of the study region is shown by the solid black line. Axes are polar stereographic X,Y in km.

5.3.5 Net Ice Build-up Calculation

The build-up of ice was calculated on a 5 km grid and stagnation of the ice stream propagates upstream in one year time steps. It is assumed that upstream of stagnation the ice sheet is in balance, in other words, accumulation is balanced by flow so that there is no change in ice-sheet thickness. At the stagnating grid cells, net ice-sheet thickness change is the sum of influx and accumulation. Grid cells downstream of stagnation are assumed to be out of balance, where ice is no longer flowing in or out and therefore any accumulation contributes to ice-sheet thickening.

When calculating the influx it is assumed that the ice is flowing at the same velocity with the full depth of the ice. Influx for a given cell in the area of fast flow is therefore:

$$Influx = velocity * width * thickness \qquad \text{Equation 5.1}$$

Ice thickness is taken from Bedmap2 (Fretwell et al., 2013). Because Bedmap2 is present-day ice-sheet thickness, using it in this calculation will lead to an overestimation of influx as the ice thickness prior to stagnation was presumably thinner than the present-day. It is assumed these differences are small and this is discussed further in Section 5.5.2. Furthermore it is assumed that the thickening at the surface of the ice sheet is not strictly confined to the area of the flowing ice stream, and there would be some degree of spread at the surface. This was accounted for by taking the total influx for a given time, using 80% to thicken grid cells in the flowing area, and 20% on the neighbouring grid cells in the drainage basin mask (Figure 5.1). Influx was divided by the area of the grid cells to obtain the height thickening and this field was smoothed using a Gaussian filter (with 35 km width). In addition to influx, accumulation also contributes to net ice-sheet thickness change for stagnating or stagnated (downstream) cells as there is no or little outflow from these regions. Accumulation is taken from RACMO2.1/ANT data as described in Section 5.2.2, and as mentioned earlier, accumulation has been stable in this region for the past 2 ka.

The ice build-up calculation is described in Table 5.3 where the profiles correspond to those described by Retzlaff and Bentley (1993) for the timing of stagnation.

After stagnation has reached profile 4, it is assumed that the ice stream has ceased to flow downstream of this location. Between profile 4 and 5, ice still flows at around 50 m/yr. Upstream of profile 5 it is assumed that flow is still occurring and accumulation is in balance with flow there. The ice loading history was calculated up to 2010. For the time steps between the end of stagnation and 2010 (see Table 5.2), the change in ice-sheet thickness was given by the ICESat-observed elevation change rate (Pritchard et al., 2009). It is assumed that elevation change is only due to inflowing ice where the rate of thickening is greater than 0.3 m/yr, as assumed by McMillan et al. (2014). That is, the elevation change is occurring at the density of ice (917 kg/m^3). The location of thickening of >0.3 m/yr coincides with the location of profile 4, where the tributaries cease to flow. Where elevation change is less than 0.3 m/yr, it is assumed to be due to short-term fluctuations in SMB (over the ICESat observing period) and hence does not contribute to net changes in ice-sheet thickness. The net ice-sheet thickness change is therefore given by ICESat elevation change where it is greater than 0.3 m/yr, plus accumulation (the long term average SMB from RACMO2.1/ANT) where the ice stream is stagnated down-stream of profile 4. A major assumption with this approach is that the spatial pattern of thickening observed by ICESat between 2003 and 2007 has

remained the same since the ice stream stopped stagnating. This is discussed further in Section 5.5.2.

Location	Description
Grounding Line to Profile 1	Profile 1 is the profile furthest downstream and is around 25 km from the current grounding line. It is assumed that stagnation between the grounding line and profile 1 occurred over 5 years at a rate of 5 km/yr. The starting time is given in Table 5.2 for each of the three loading scenarios.
Profiles 1-4	Between profile locations 1 and 4, ice-sheet thickness change is calculated on 1 year time steps. As stagnation propagates upstream, the number of grid cells "stagnating" at a given time depends on how far upstream stagnation is occurring and the speed of stagnation as detailed in Table 5.2. This is detailed below.
Profile 1-2	The ice stream is stagnating at a rate of 15 km/yr, so 3 grid cells width in the along stream profile direction are stagnating in 1 time step, based on the 5 km grid cells.
Profile 2-3	As for Profile 1-2, ice stream stagnating at a rate of 10 km/yr - 2 grid cells per time step.
Profile 3-4	As for Profile 1-2, ice stream stagnating at a rate of 5 km/yr - 1 grid cell per time step.
Profile 4-5	The section between profile 4 and 5 is treated a little differently because measurements of present-day velocity show that tributaries are still flowing into the KIS at around 50 m/yr (Rignot et al., 2011). Therefore for this section, flow of the ice stream is slowed down rather than stagnated completely. The velocity is reduced from the pre-stagnation values (i.e. 100, 200, 300 m/yr) to the present-day velocity (50 m/yr) linearly over the length of time this section takes to stagnate (28 time steps, see Table 5.2).

Table 5.3: Description of the ice build-up calculation by location.

Several ice sheet histories have been constructed based on the three timing scenarios detailed in Table 5.2 - lower bound (LB), best estimate (BE) and upper bound (UB) - and the different pre-stagnation velocities used (100, 200, and 300 m/yr). These are shown in Table 5.4, with the naming convention used.

	Velocity		
Timing	**100**	**200**	**300**
LB	LB_100	LB_200	LB_300
BE	BE_100	BE_200	BE_300
UB	UB_100	UB_200	UB_300

Table 5.4: Names of ice loading models constructed in this study.

5.3.6 Results

The results of the ice loading history calculations are shown in the following table and figures. The maximum ice-sheet thickness change for all models is given in Table 5.5. Cumulative change in ice-sheet thickness on 10 year time steps from 1820 to 2010 is shown for the two end member models "LB_100" (Figure 5.5) and "UB_300" (Figure 5.7) along with best estimate model "BE_200" (Figure 5.6).

Model	Timing of ice loading history	Total number of years	Maximum ice-sheet thickness change (m)
LB_100*	1863 - 2010	148	70.0
LB_200			88.7
LB_300			107.6
BE_100	1843 - 2010	168	81.9
BE_200*			100.4
BE_300			119.2
UB_100	1823 - 2010	188	93.7
UB_200			112.1
UB_300*			130.9
*Models corresponding to Figure 5.5, Figure 5.6, and Figure 5.7.			

Table 5.5: Maximum ice-sheet thickness change for all ice loading models.

The amount of ice build-up varies for each of the models, but in general the earlier stagnation occurs the greater the amount of ice that builds up. Similarly, a higher pre-stagnation velocity of the ice stream results in a larger amount of influx and hence increased ice build-up. There is little variation in the spatial pattern of ice build-up. A small anomalous area of ice build-up occurs towards the upstream section of the study domain in the models from 1910-1950 onwards. This is due to a small pocket of thickening of >0.3 m/yr in the ICESat data (see also Figure 5.3) that is included in the calculations for ice build-up once the ice stream has stagnated. This small anomaly will have a negligible effect on the GIA results.

There is significant overlap of the results from the nine ice histories. A shorter stagnation period combined with higher velocity gives similar results to a longer time with a lower velocity. For example, the maximum ice-sheet thickness change from model LB_200 (88.7 m) is similar to that of model BE_100 (81.9 m). Therefore, for input to the GIA model, only three ice histories were used; the extreme upper and lower bounds (LB_100, UB_300), and the best estimate (BE_200). The average maximum ice-sheet thickness change for all models is 100.5 m, almost identical to the 100.4 m from the BE_200 model, so this model can confidently be used as the best estimate.

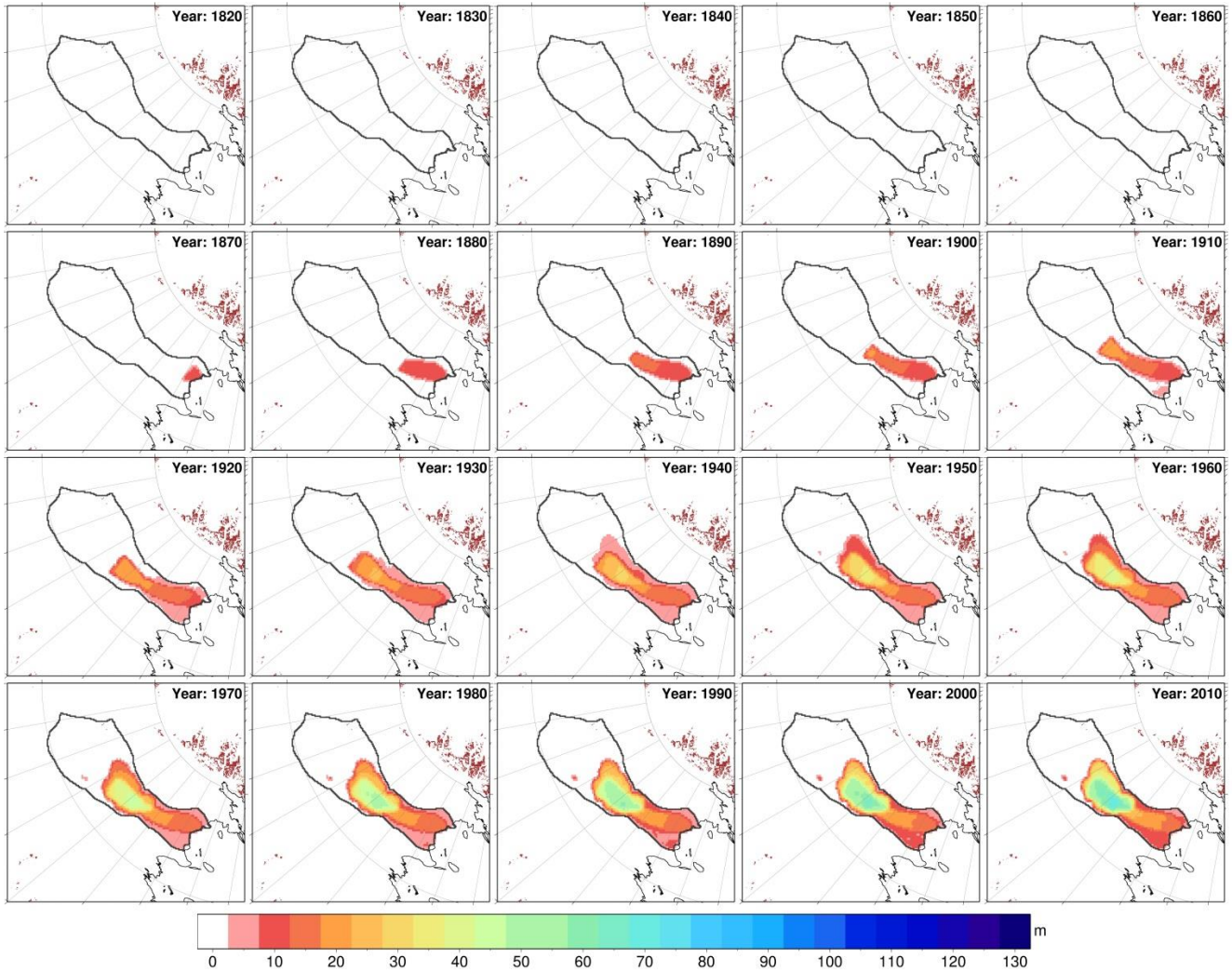

Figure 5.5: Cumulative ice-sheet thickness change for model LB_100 on 10 year time steps. The extent of the study region is shown by the solid dark grey line and rock outcrops are shown in brown.

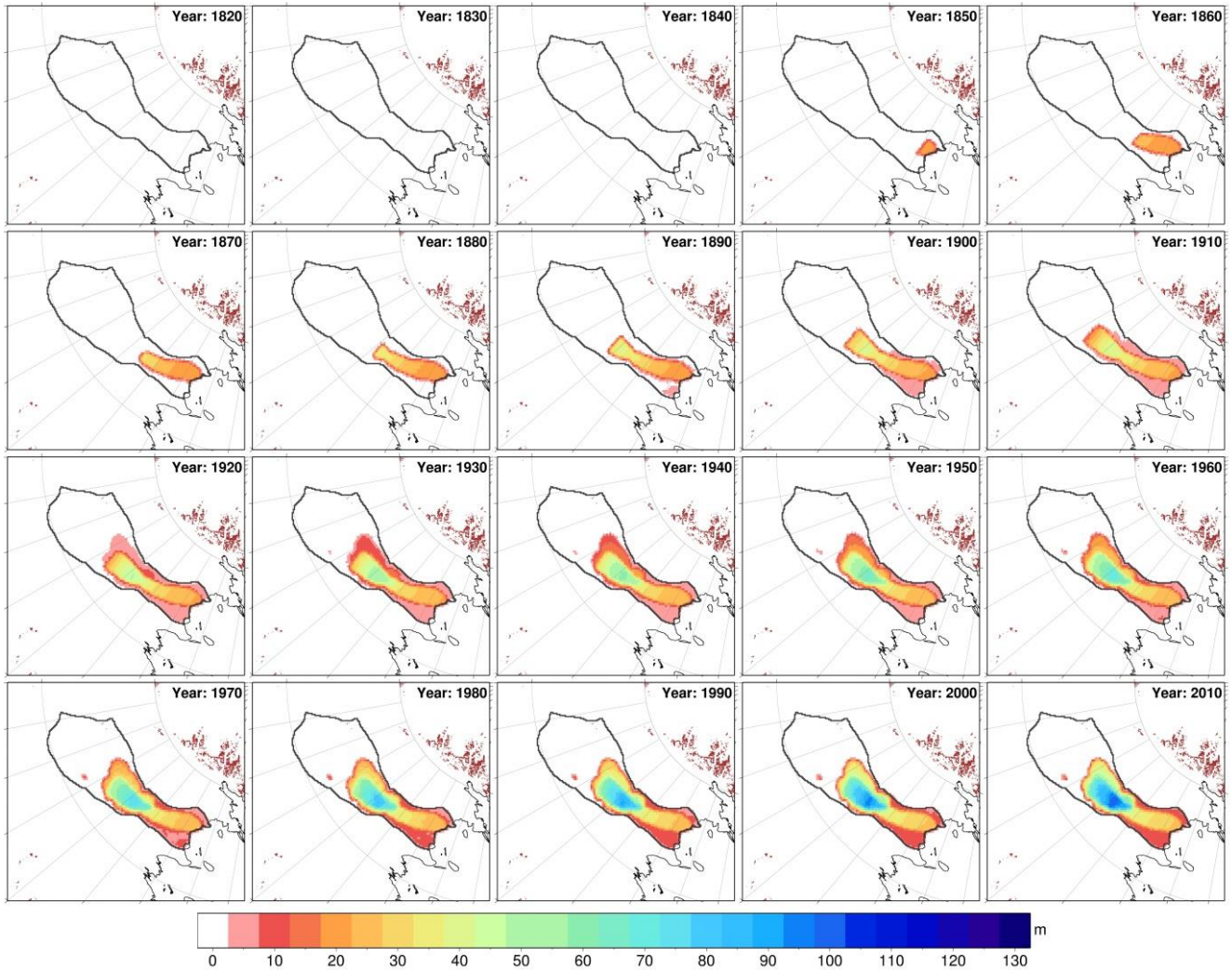

Figure 5.6: Cumulative ice-sheet thickness change for model BE_200 on 10 year time steps. The extent of the study region is shown by the solid dark grey line and rock outcrops are shown in brown.

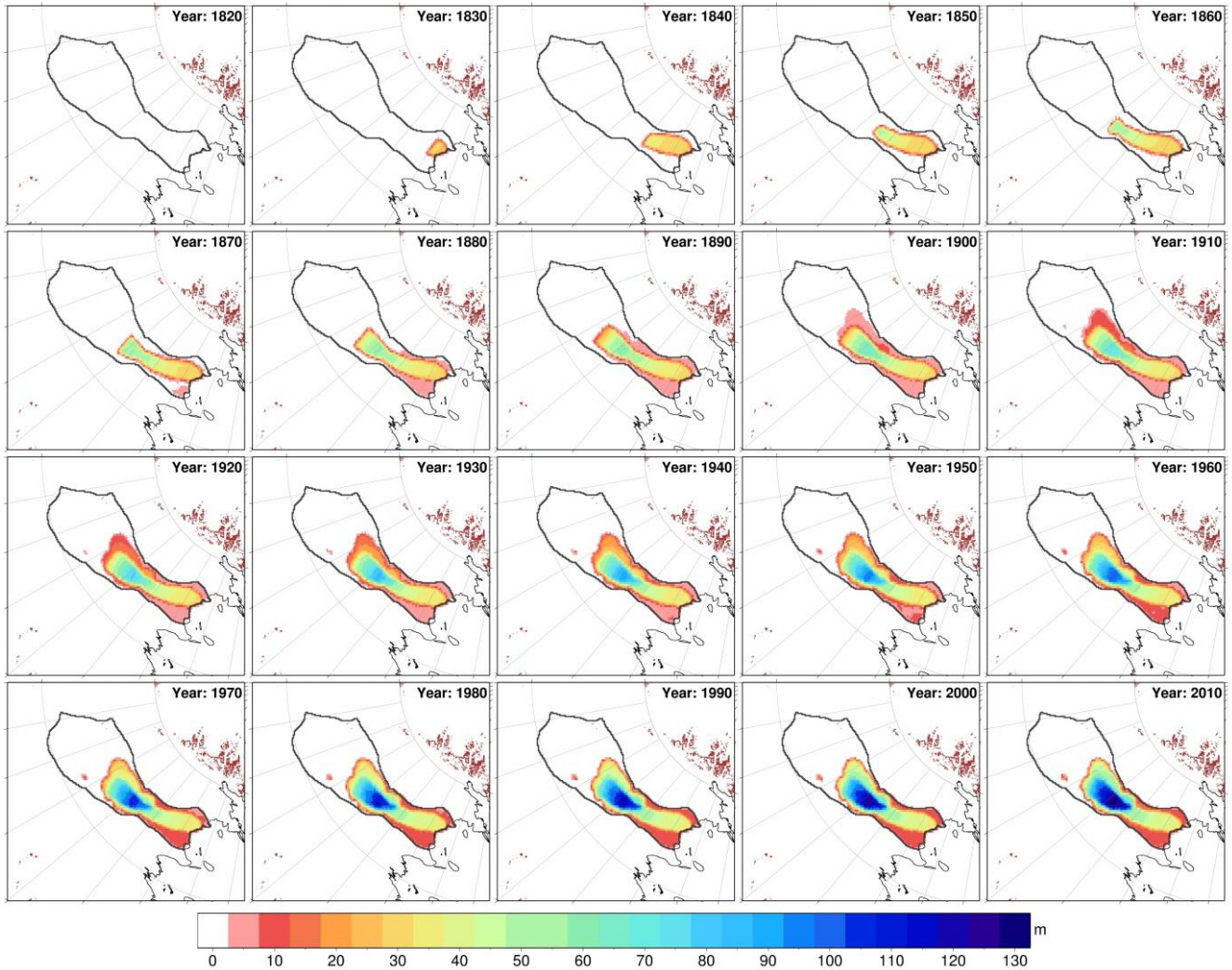

Figure 5.7: Cumulative ice-sheet thickness change for model UB_300 on 10 year time steps. The extent of the study region is shown by the solid dark grey line and rock outcrops are shown in brown.

5.4 GIA Modelling

The GIA model used for this work is described in Section 2.2.1. The ice loading history was interpolated onto a spherical harmonic grid of degree and order 256, corresponding to approximately 80 km spatial resolution. The ice thickness increase in the study region is a long wavelength signal, and unlike the Antarctic Peninsula with its steep topography, there is no particular requirement to increase the model resolution. Furthermore, the W12 deglacial model, which is used in three of the loading scenarios described below, is only available at degree 256 and so by consistently using degree 256 all results can be compared.

Four loading scenarios have been modelled:

1. The build-up of ice related to the recent stagnation of KIS has been modelled in isolation to examine the magnitude of this signal based on a range of Earth models (see Section 5.4.1). All ice-sheet thickness changes outside of the study region were set to zero. GIA model predictions have been made for three of the ice loading models described above; the two end member models, LB_100 and UB_300, and the best estimate BE_200 model.
2. The best estimate loading history (BE_200) has been added to the end of the W12 ice loading history to examine the signal in the context of an LGM deglaciation history.
3. A cyclical loading scenario has been considered, whereby KIS stagnates 1000 years BP and reactivates 500 years later in addition to the most recent stagnation event. This is added to the end of the W12 deglaciation model.
4. A further cyclical loading scenario has been modelled which includes a 2000 year history of stagnation and reactivation of KIS, WIS, and MacAyeal Ice Stream (MacIS) in combination with the W12 model. In this scenario KIS stagnates 1800 years ago and reactivates 1000 years ago, followed by WIS and MacIS which stagnate 850 years ago reactivating 400 years later. The most recent stagnation of KIS is then included from 165 years ago to present.

Following an introductory discussion of the Siple Coast Earth structure and Earth models in Section 5.4.1, each sub-section below describes in detail the four ice loading histories considered, and presents the results of the GIA modelling. Finally, a sub-set of the results are compared with an empirical model of GIA.

5.4.1 Earth Models

As discussed in Chapter 1, the Earth structure below Antarctica is poorly known and the Siple Coast is no exception to this. Typically, West Antarctica is considered to have a thin lithosphere and low viscosity mantle (Morelli and Danesi, 2004) compared with East Antarctica. A et al. (2013), and references therein, reported 3-D Earth structure for Antarctica (adopted from other studies) that they used for the purposes of GIA modelling. At a depth of 372 km below the Siple Coast study region, they suggest the mantle viscosity is in the range $3 - 5 \times 10^{20}$ Pa s. For the lithospheric thickness, they suggest a value of approximately 50 km near the grounding line, increasing to around 70-80 km at the upstream reaches of the drainage basin (their Figure 9). In their study of the effect of lateral viscosity variations on present-day deformations, Kaufmann et al. (2005) used an upper mantle viscosity between 1×10^{19} Pa s and 3×10^{20} Pa s for West Antarctica, with increasing viscosity towards the Trans-Antarctic Mountains. Below 450 km depth this increased to 1×10^{21} Pa s for much of West Antarctica. They combined this with a 100 km thick lithosphere.

Due to the uncertainty in the Earth structure, a range of Earth models has been used to model the solid Earth response to the ice loading scenarios described in the following sections, and these are listed in Table 5.6. The lithospheric thicknesses used in the modelling are 46, 71 and 96 km and the range of upper mantle viscosities tested is $0.5 - 5 \times 10^{20}$ Pa s. The Earth model corresponding to the W12 GIA model (Whitehouse et al., 2012b) is also tested, which has a 120 km thick lithosphere and an upper mantle viscosity of 1×10^{21} Pa s. The lower mantle viscosity is fixed at 1×10^{22} Pa s in all cases.

Lithospheric Thickness (km)	**Upper Mantle Viscosity ($\times 10^{21}$ Pa s)**	**Lower Mantle Viscosity ($\times 10^{21}$ Pa s)**
46	0.05, 0.1, 0.5	10
71	0.05, 0.1, 0.5	10
96	0.05, 0.1, 0.5	10
120	1	10 (W12 model)

Table 5.6: Earth models used in this study.

5.4.2 GPS Data

GPS data is available from several ANET sites in the region of the Siple Coast as detailed in Table 5.7, with locations shown on Figure 5.1. The observed uplift rates and uncertainties have been taken from Argus et al. (2014). Also given in Table 5.7 is the modelled elastic uplift at each site based on present-day ice loss in the northern Antarctic Peninsula and Amundsen Sea sector, as given by Argus et al. (2014). It is worth noting that Gunter et al. (2014) estimate elastic uplift to be <0.3 mm/yr at all GPS locations outside of the northern Antarctic Peninsula and Amundsen Sea sector, although they do not include SDLY or RAMG in their analysis. SDLY is located closer to the Amundsen Sea sector than the other sites and is therefore the only site likely to be affected by elastic uplift. The nearby site of Whitmore Mountains (WHTM) has been excluded as the time series is highly non-linear (M. King pers. comm. 04/08/14).

Site	Latitude (°)	Longitude (°)	GPS Observed Uplift (mm/yr)	Elastic uplift due to current ice loss (mm/yr)
Mount Howe (HOWE)	-87.42	-149.43	0.9 ± 2.4	0.3
Mount Paterson (PATN)	-78.03	-155.02	5.5 ± 3.1	0.4
Mount Sidley (SDLY)	-77.14	-125.97	0.8 ± 6.3	1.3
Clark Mountains (CLRK)	-77.34	-141.87	5.4 ± 6.1	0.6
Ramsey Glacier (RAMG)	-84.34	178.05	3.1 ± 5.1	0.3

Table 5.7: Location and observed uplift rates for ANET GPS sites in the Siple Coast region. Uncertainties are 10 mm divided by the time period of observation (see Argus et al. (2014)for full details). Last column is the present-day modelled elastic uplift at each site from Argus et al. (2014).

5.4.3 Single KIS Stagnation

The three ice loading histories shown in Figure 5.5, Figure 5.6, and Figure 5.7 (LB_100, BE_200, and UB_300) were interpolated onto a global spherical harmonic grid of degree and order 256 for input to the GIA model. Ice-thickness change outside the KIS basin is set to zero to isolate the response of stagnation-related ice build-up. The model was run on 10 year time steps for the build-up of ice related to KIS thickening, with a spin up between 3000 and 500 years ago on longer time steps in which it is assumed there is no change in ice-sheet thickness. There is also no change in ice-sheet thickness in the last five (1-year) time steps corresponding to 2010-2014 to ensure no ongoing

elastic uplift affects the predicted vertical deformation rate. The time steps are shown in Table 5.8.

Time-step (years before present)	Ice loading model output used LB_100	Ice loading model output used BE_200	Ice loading model output used UB_300
3000	1870	1850	1830
2000	1870	1850	1830
1000	1870	1850	1830
500	1870	1850	1830
182	-	-	1830
172	-	-	1840
162	-	1850	1850
152	-	1860	1860
142	1870	1870	1870
132	1880	1880	1880
122	1890	1890	1890
112	1900	1900	1900
102	1910	1910	1910
92	1920	1920	1920
82	1930	1930	1930
72	1940	1940	1940
62	1950	1950	1950
52	1960	1960	1960
42	1970	1970	1970
32	1980	1980	1980
22	1990	1990	1990
12	2000	2000	2000
2	2010	2010	2010
1	2010	2010	2010
0	2010	2010	2010
-1	2010	2010	2010
-2	2010	2010	2010

Table 5.8: GIA model time steps and the ice loading history used for each time step.

The model-predicted vertical deformation in response to the build-up of ice related to the stagnation of KIS only is shown in Figure 5.8 for a range of Earth models. As expected, the largest amount of deformation occurs at the location of maximum ice build-up. Solid Earth deformation is shown for the ice model BE_200 only. For the UB_300 and LB_100 ice models, the amount of subsidence is slightly more or less than the BE_200 model, respectively, for each Earth model. The maximum subsidence for each combination of ice and Earth model is given in Table 5.9. There is potentially a large amount of subsidence related to thickening on KIS, depending on the Earth model

used, which could be up to -17 mm/yr for the weakest Earth model combined with largest ice load, although this reduces to around -1 mm/yr for the stronger Earth models tested.

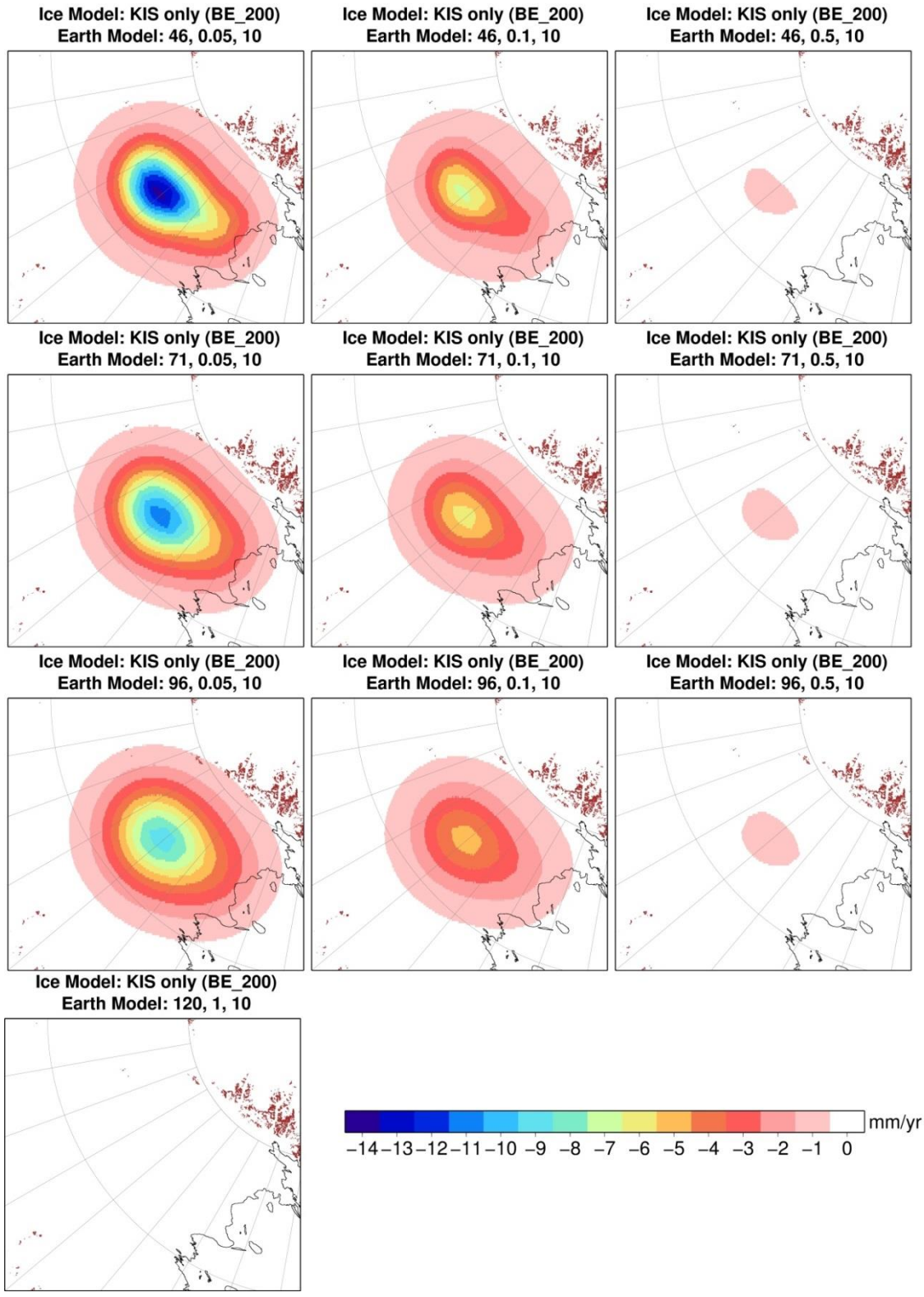

Figure 5.8: GIA model results for KIS-only ice history (model BE_200) combined with 10 Earth models. Rock outcrops are shown in brown. Earth model labels are lithospheric thickness (km), upper mantle and lower mantle viscosity (×10^{21} Pa s).

				Maximum subsidence (mm/yr) for ice models:		
Earth Model	**L**	**UM**	**LM**	**LB_100**	**BE_200**	**UB_300**
	46	0.05	10	-11.1	-14.2	-17.2
	46	0.1	10	-5.4	-7.0	-8.6
	46	0.5	10	-0.6	-0.7	-0.9
	71	0.05	10	-8.9	-11.3	-13.5
	71	0.1	10	-4.7	-6.0	-7.3
	71	0.5	10	-0.6	-0.8	-0.9
	96	0.05	10	-7.2	-9.1	-10.7
	96	0.1	10	-3.9	-5.0	-6.0
	96	0.5	10	-0.5	-0.7	-0.9
	120	1	10	-0.2	-0.2	-0.3

Table 5.9: Maximum present-day rate of subsidence for the different combinations of ice and Earth models. For the Earth models, L is lithospheric thickness (km), and UM and LM are upper and lower mantle viscosity (×10^{21} Pa s), respectively.

5.4.4 LGM Deglaciation and KIS

To investigate the solid Earth response to the stagnation-related ice build-up in the context of longer-term deglaciation, the best estimate model (BE_200) was added to the end of an existing LGM deglacial model, W12 (Whitehouse et al., 2012a). The combined ice history is referred to as W12+KIS. Although the W12 deglacial history has a specific Earth model (see Table 5.6) that ensures the best fit between model results and observational data, the deglacial model was developed independently of it. This means that the W12 deglacial history combined with the KIS ice build-up can be modelled with different Earth parameters, but that the resulting model predictions will no longer fit the relative sea-level data that W12 previously fit. The results can therefore only be examined on a regional scale for the Siple Coast. Furthermore, the LGM deglacial history being used is W12, and not W12a (Whitehouse et al., 2012b). This is because of the significant amount of ice that was added to the Antarctic Peninsula during the last 1000 years of W12a, a total of 300 m between 1000 and 100 years BP. Modelling the W12a deglacial history with a weaker Earth structure means that this extra ice may influence the GIA signal in the Siple Coast. Conversely, a more realistic amount of additional ice loading in the Antarctic Peninsula, such as the ~45 m suggested in Chapter 3, would likely not cause interference with the Siple Coast deformation, as shown by the spatial extent of the subsidence signal in Figure 3.11. The W12 deglacial history has no ice loading changes after 2 ka BP, so the combined model W12+KIS has a constant load between 2 ka and the commencement of KIS loading changes 162 years BP.

Present-day model-predicted uplift for each of the 10 Earth models is shown in Figure 5.9 along with the GPS-observed uplift rates. For the weaker Earth models, the vertical deformation is generally in the range -2 to 2 mm/yr, with the exception of a large subsidence signal over KIS of around -10 to -15 mm/yr. For the stronger Earth models, the uplift largely resembles the original W12 uplift (see the last panel of Figure 5.9, and Section 2.3.2) with a significant amount of uplift in the Ross Sea.

The GPS sites are located more than 400 km from the KIS basin, and consequently the uplift recorded at these sites cannot be used to place constraints on the large local subsidence predicted by the model in the region of KIS. Instead, the GPS-recorded uplift may be used to verify the wider-scale pattern of uplift from the combined W12+KIS model. In general, the Earth models with an upper mantle viscosity of 1×10^{20} Pa s (middle column of Figure 5.9) show a reasonably good fit to the GPS data, although not appreciably better than the original W12 Earth model (last panel of Figure 5.9).

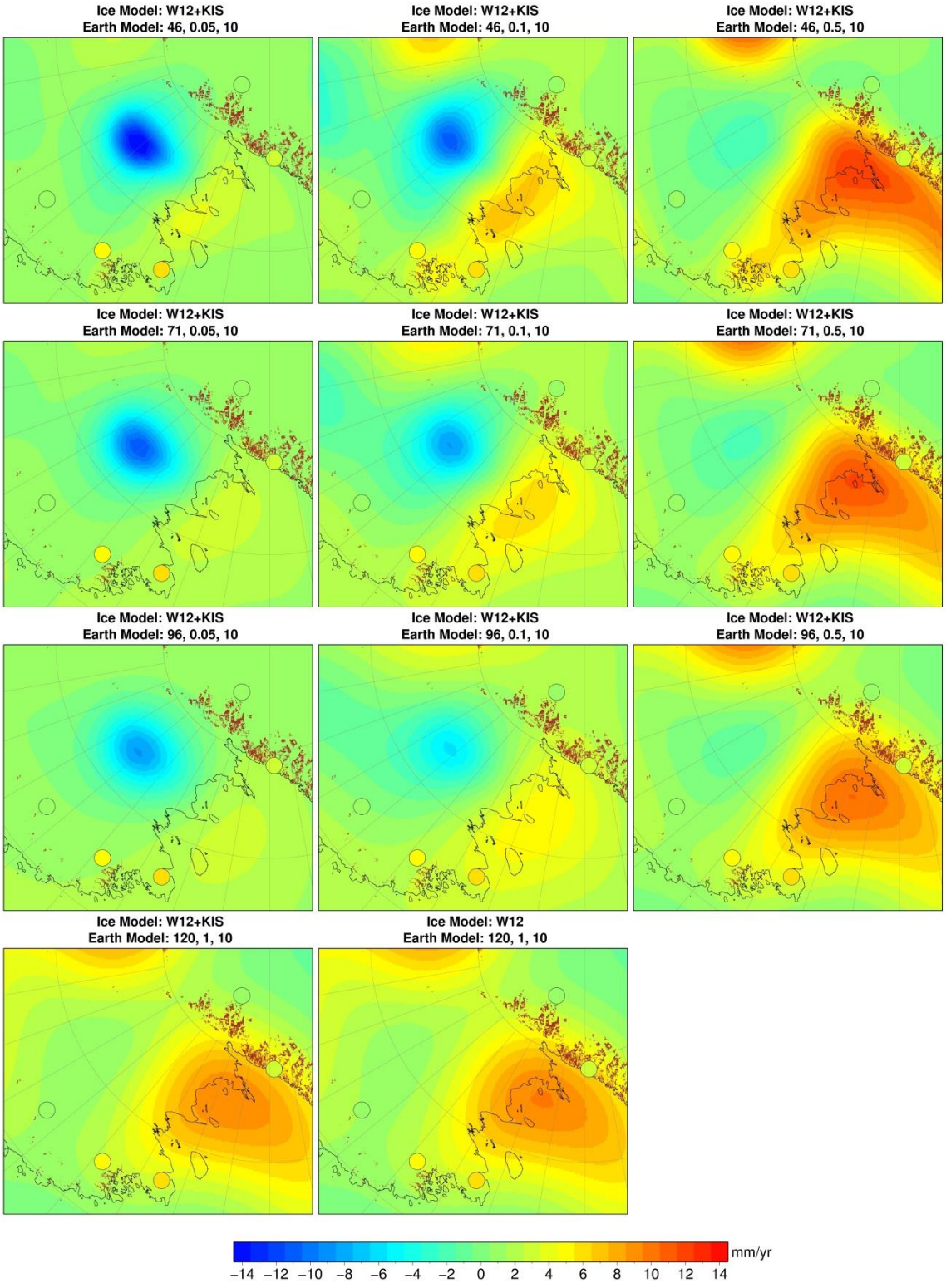

Figure 5.9: Present-day GIA uplift rates for the combined ice history W12+KIS for 10 Earth models. Earth model labels are lithospheric thickness (km), upper mantle and lower mantle viscosity (×10^{21} Pa s). GPS uplift rates are plotted as circles using the same colour scale.

5.4.5 KIS Cyclic Model

As described previously, Siple Coast ice streams have stagnated and reactivated periodically over the last 2000 years. To investigate the effects of a longer-term ice

history on the present-day GIA uplift, a cyclical loading model was created. An extra loading and unloading phase was added to the W12+KIS loading history between 1000 and 500 years BP to represent an additional stagnation and reactivation cycle of KIS. If an ice stream reactivates after stagnation-related ice build-up has occurred, the extra ice would diminish due to the increased flow, in other words there would be an unloading of ice. Unloading on KIS may result in uplift that counteracts the large subsidence caused by the most recent stagnation and loading. The extra loading and unloading was taken to be equivalent to the cumulative ice thickness at the 2010 time slice from the BE_200 ice model above and was applied instantly. The adjusted timings of this loading history are given in Table 5.10.

Time (years BP)	Event	Ice History
Prior to 1000		W12 ice loading
1000	KIS stagnates	Instant loading
500	KIS reactivates	Instant unloading
165-0	KIS stagnates	Loading – build-up as per BE_200 model (Table 5.8)

Table 5.10: Additional ice loading events and time steps for the KIS cyclic model.

The GIA model-predicted uplift from this adjusted loading model is differenced with the W12+KIS results and shown in Figure 5.10, for the same Earth models used previously. For the models with lower viscosity upper mantle (0.5-1 × 10^{20} Pa s) there is between -2 and -5 mm/yr difference between the models; that is, there is 2-5 mm/yr *less* subsidence at the present-day than the W12+KIS loading history alone. For stiffer Earth models, with upper mantle viscosity of 5 × 10^{20} Pa s, there is negligible difference between the models (~0.3 mm/yr less subsidence).

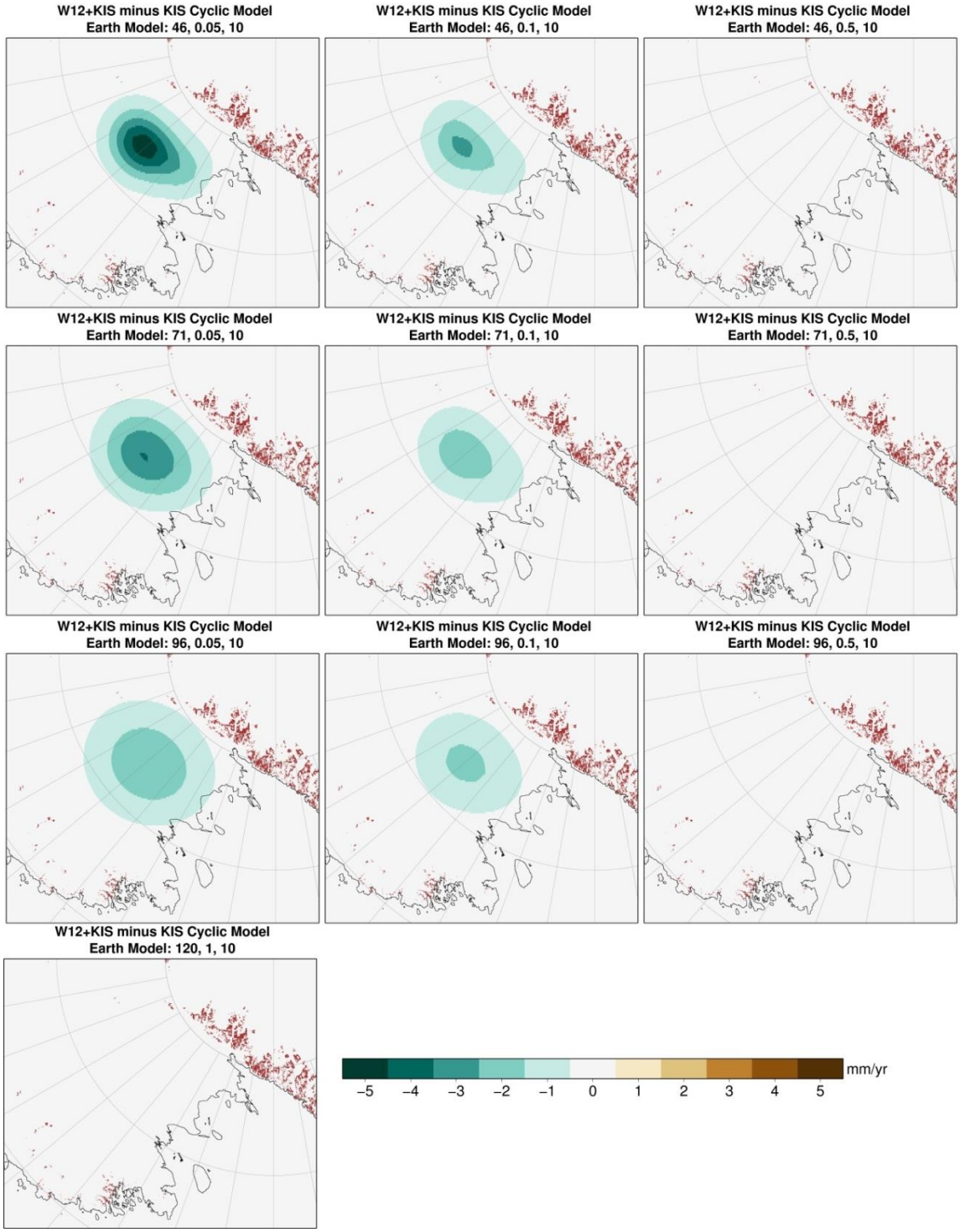

Figure 5.10: Difference between the W12+KIS model and the KIS cyclic model (W12+KIS minus KIS cyclic model) for 10 Earth models. Earth model labels are lithospheric thickness (km), upper mantle and lower mantle viscosity (×10^{21} Pa s).

5.4.6 Regional Cyclic Model

A further cyclical ice loading model was investigated, expanding the Late Holocene fluctuations to the past 2000 years and over a wider area. Catania et al. (2012) summarise stagnation and reactivation of all Siple Coast ice streams over the past 1000 years. This history was used to construct a simple loading history which includes

loading related to stagnation of the neighbouring ice streams WIS and MacIS 850 years BP, reactivating and unloading 400 years later. As detailed data is not available regarding the timing of the stagnation of these ice streams as for the recent stagnation of KIS, a simple model was constructed using an arbitrary uniform amount of ice thickening (200m) over a small portion of the ice stream, as shown by the green shaded regions in Figure 5.1. These areas were selected arbitrarily and represent a small section of the ice stream where maximum build up might be expected. As with the KIS cyclic model, the ice loading and unloading was applied instantly.

An additional stagnation and reactivation of KIS was also included between 1800 and 1000 years ago using, as before, a load equivalent to the 2010 time slice from the BE_200 model. Whilst there is no direct evidence for stagnation of KIS during this time, as buried crevasses only relate to the most recent stagnation event, it is reasonable to suppose it has previously stagnated and reactivated at some point in the past (e.g. Hulbe and Fahnestock, 2007). The final loading event is the progressive build-up of ice on KIS, as per BE_200. This 2000-year ice loading scenario was then added to the end of W12. The timings of this ice loading history are given in Table 5.11

Time (years BP)	Event	Ice History
Prior to 2000		W12 ice loading
1800	KIS stagnates	Instant loading
1000	KIS reactivates	Instant unloading
850	WIS stagnates	Instant loading
	MacIS stagnates	Instant loading
450	MacIS reactivates	Instant unloading
	WIS reactivates	Instant unloading
165-0	KIS stagnates	Loading – build-up as per BE_200 model (Table 5.8)

Table 5.11: Additional ice loading events and time steps for the regional cyclical model.

As for the KIS cyclic model, the GIA model-predicted uplift from this adjusted loading model has been differenced with the W12+KIS uplift and the results are shown in Figure 5.11. The magnitude of the differences are very similar to the previous ice loading history, showing 2-5 mm/yr *less* subsidence at the present-day than the W12+KIS model, for the lower viscosity models. However, the spatial pattern is slightly different, reflecting the additional loading events on the neighbouring ice streams. Furthermore, there is less uplift over the Ross Ice Shelf (indicated by the positive difference on Figure 5.11), which would act to reduce the uplift centre present in the

W12 model at this location. As before, the Earth models with upper mantle viscosity of 5×10^{20} Pa s show negligible difference between the ice models (~0.3 mm/yr less subsidence).

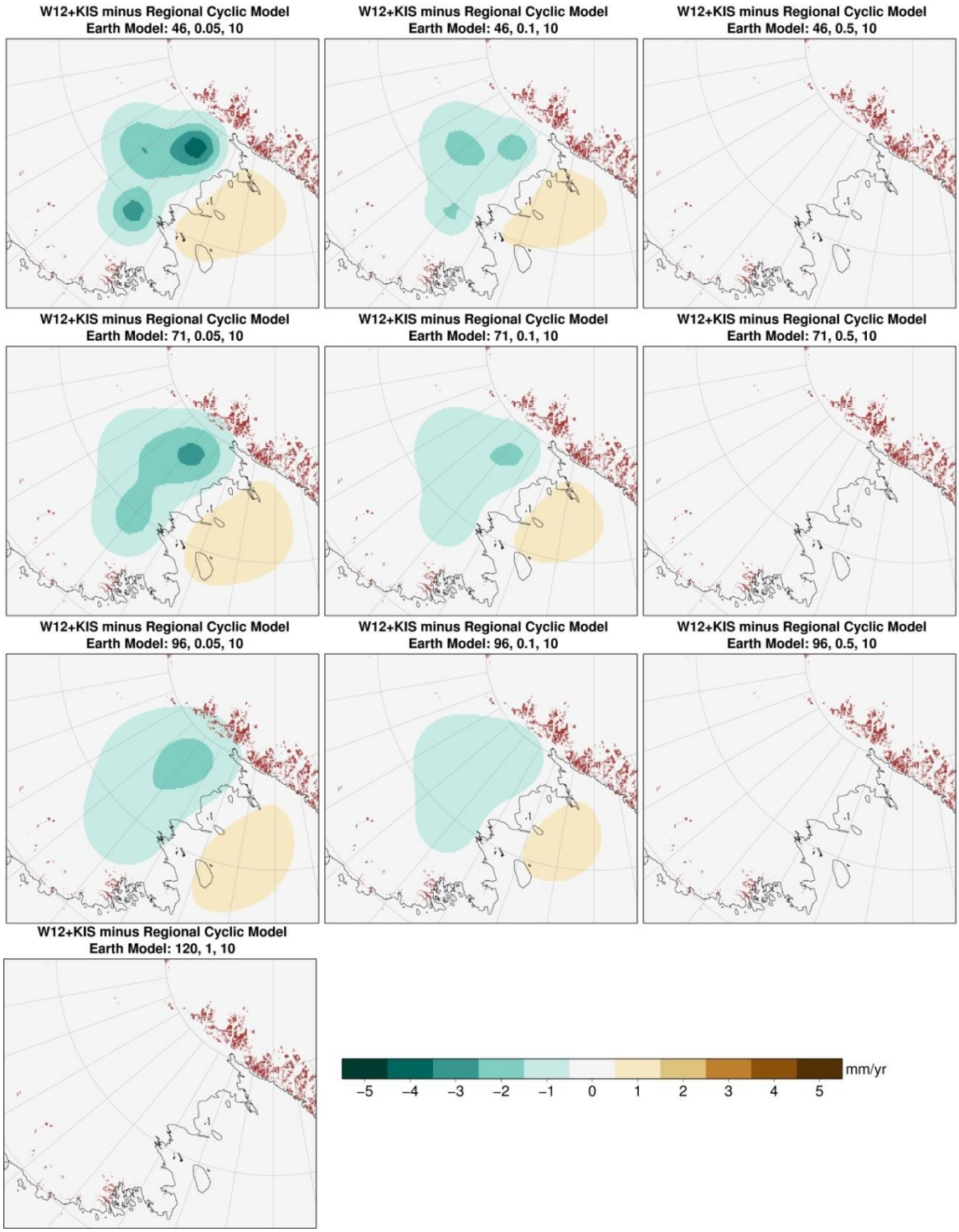

Figure 5.11: Difference between the W12+KIS model and the regional cyclic model (W12+KIS minus regional cyclic model) for 10 Earth models. Earth model labels are lithospheric thickness (km), upper mantle and lower mantle viscosity (×10^{21} Pa s).

5.4.7 Comparison with Empirical GIA Model

For comparison, the GIA model-predicted vertical displacements from the three long-term loading histories described above were compared with the empirically derived GIA model of Gunter et al. (2014). The Gunter et al. (2014) model of present-day GIA uplift is derived from a combination of GRACE data and ICESat elevation-change data, (see Section 1.3.3). The resulting GIA uplift is therefore not directly dependent on either the ice loading history or Earth structure and provides an observation-based model with which GIA model predictions can be compared. Gunter et al. (2014) present several different present-day uplift fields based on different solutions, but here only the "CSR RL05 DDK5" solution is used, which is one of their best-fitting solutions to GPS-observed uplift. The uplift is reproduced in Figure 5.12a and the 1-sigma uncertainty bounds in Figure 5.12b.

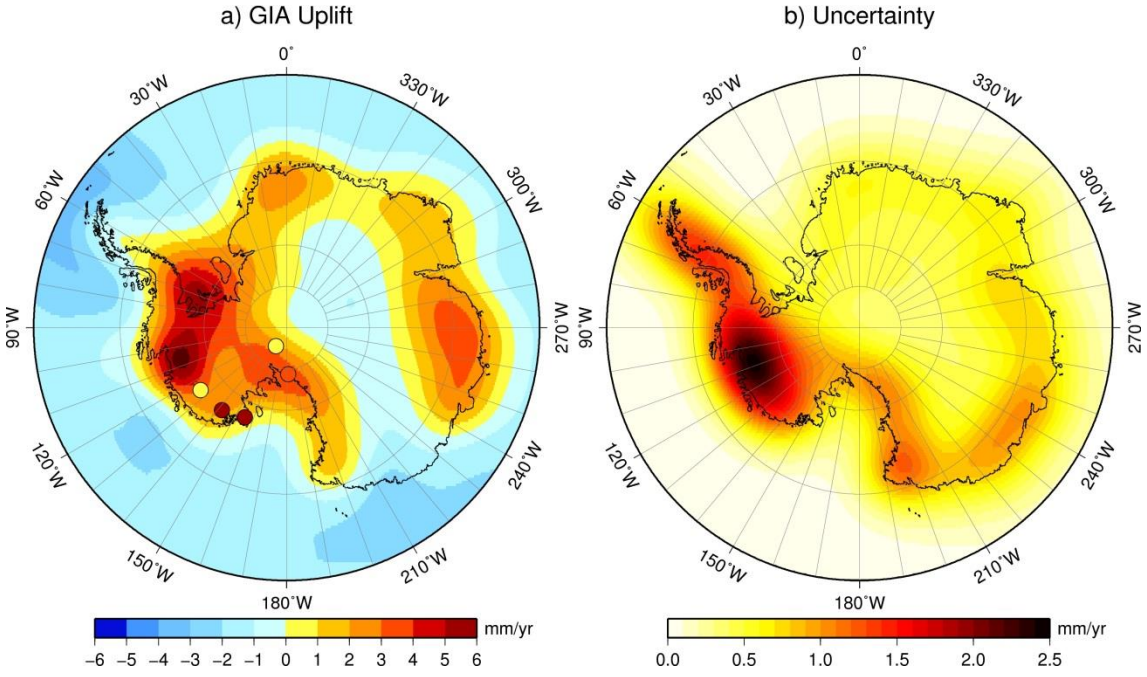

Figure 5.12: a) Present-day uplift and b) 1-sigma uncertainty from the Gunter et al. (2014)empirical GIA model, adapted from their Figures 8c and 9c. GPS-observed uplift is shown in panel a).

To compare the GIA model results with the Gunter et al. (2014) empirical model, the GIA model-predicted uplift was first smoothed with a 400 km (half width) Gaussian filter to ensure the resolution of the two models was the same, and then differenced with the empirical model. The difference in uplift is shown in Figure 5.13. The difference is shown for the three ice loading histories W12+KIS, the KIS cyclic model and the regional cyclic model, combined with 3 different Earth models – a weak Earth model

(46 km lithosphere and 0.05×10^{21} Pa s upper mantle viscosity), a medium-strength Earth model (71 km lithosphere and 0.1×10^{21} Pa s upper mantle viscosity), and the W12 Earth model (120 km lithosphere and 1×10^{21} Pa s upper mantle viscosity). For these difference figures, negative areas in blue represent the regions where the GIA model over-predicts uplift compared with the Gunter et al. (2014) empirical model, and the positive red areas indicate where the model under-predicts uplift compared with the empirical model.

The results for the weaker Earth models with an upper mantle viscosity of 1×10^{20} Pa s or less (first and second column of Figure 5.13), show widespread under-prediction of uplift, by up to 10 mm/yr, compared with the Gunter et al. (2014) empirical model. This is dominated by subsidence related to the recent build-up of ice on KIS, but the addition of multiple stagnation and reactivation events over the past 1000-2000 years lessens this slightly (row 2 and 3 of Figure 5.13). Over the Ross Ice Shelf, there is a better match between the two models, with misfits of 3 mm/yr or less for the weaker Earth models.

For the W12 Earth model (third column of Figure 5.13), the plots are almost identical for each of the ice loading histories, and the small load history fluctuations over the past 2000 years do not lead to much impact. The misfit with the Gunter et al. (2014) model is dominated by the large uplift centre on the Ross Ice Shelf that is present in the W12 model (see Figure 2.1), shown in blue on these plots. This indicates that the W12 model over-predicts uplift by up to 6 mm/yr compared with the Gunter et al. (2014) model. King et al. (2012b) also suggest that W12 over-predicts uplift on the Ross Ice Shelf, estimating that GIA here should be close to zero. Combining the W12 deglacial model with the ice build-up related to the stagnation of KIS, with or without the addition of multiple stagnation and reactivation cycles, does not produce a present-day uplift that is consistent with the Gunter et al. (2014) empirical GIA model, for any of the Earth models tested.

The difference between GPS-observed uplift rates and GIA-modelled uplift rates are also shown on Figure 5.13. These show a different pattern of misfits as the empirical model uplift rates do not agree with the GPS uplift rates, which can easily be seen on Figure 5.12a. SDLY and HOWE show misfits of ±1 mm/yr or less between the GPS uplift rates and GIA model predictions for all combinations of ice and Earth models. RAMG shows misfits of up to ±3 mm/yr and is the only site to agree with the empirical model rates. The largest misfits come from CLRK and PATN indicating that the model

under-predicts uplift by up to 4.5 mm/yr at these locations. The elastic uplift due to present-day ice loss at these sites is only 0.4-0.6 mm/yr which cannot explain the misfit.

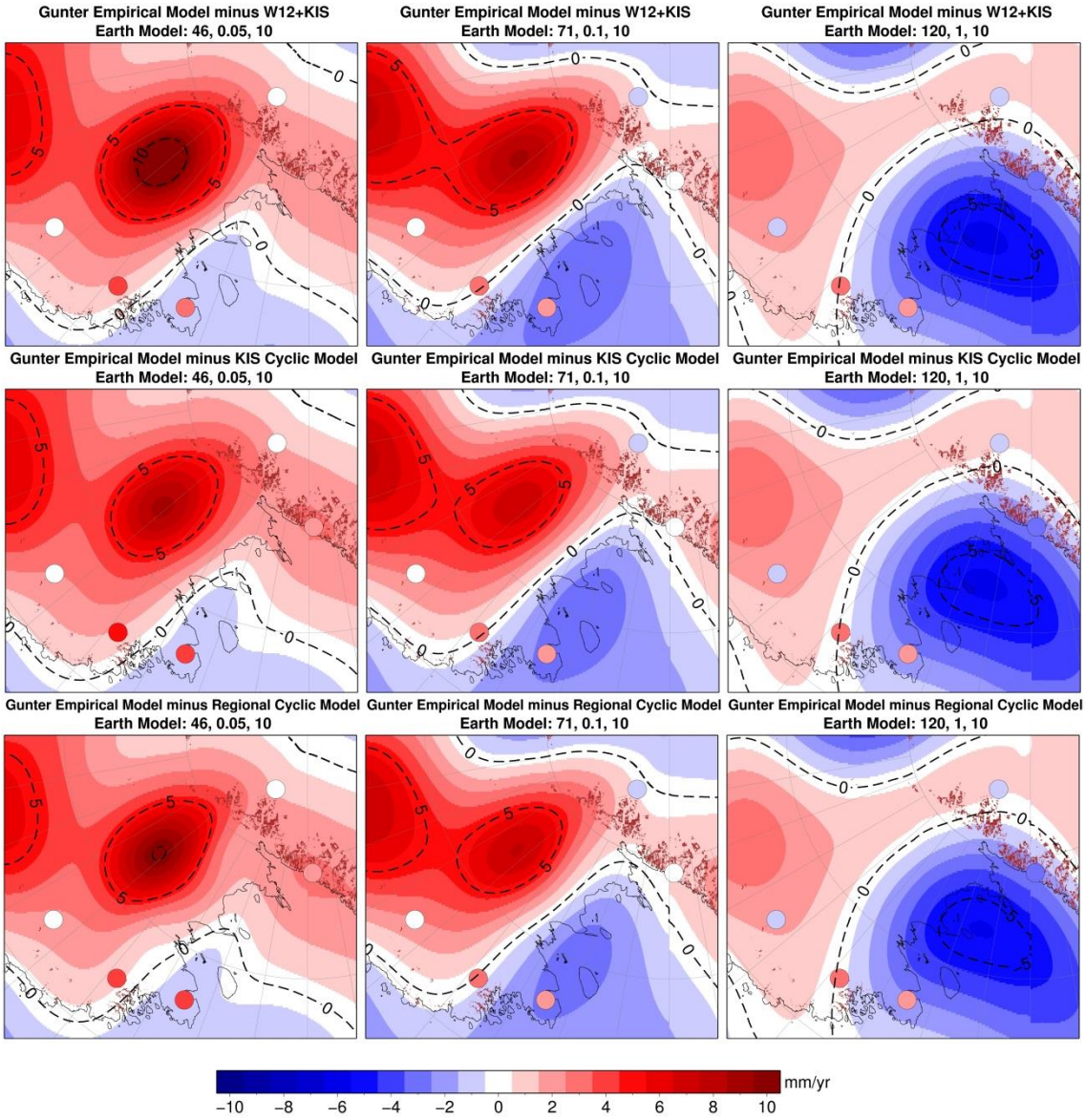

Figure 5.13: Difference between the Gunter et al. (2014) empirical model and GIA predictions for the W12+KIS ice model (top row), KIS cyclic model (middle row) and regional cyclic model (bottom rom). Earth model in the first column: 46 km, 0.05×10^{21} Pa s; second column: 71 km, 0.1×10^{21} Pa s; and last column: 120 km, 1×10^{21} Pa s. The circles show the difference between the GPS uplift rates and each GIA model plotted on the same colour scale.

5.5 Discussion

5.5.1 Ice Loading History Reconstruction

Using the available observational data a series of ice loading histories have been constructed for the ice build-up relating to stagnation of KIS. Uncertainties in the timing of ice stream stagnation, as given by Retzlaff and Bentley (1993), have been explored to obtain lower and upper bound ice histories. The pre-stagnation velocity of KIS, which

affects how much influx and build-up occurs, is also unknown and three realistic velocities were tested. This results in a total of nine ice loading histories which produce realistic amounts of ice-sheet thickness change, between 70 and 130 m over a time span of 148-188 years.

One of the limitations of the method of calculating ice build-up is that stagnation of a given grid cell occurs in one time step, equivalent to one year. Stagnation likely occurred over several years, as indicated by the Duckfoot region that shutdown in around 10 years (Catania et al., 2006). The result of this assumption is that ice thickness change would be underestimated; if the ice stream shut down over a number of years there would be additional influx to the system which has not been accounted for in these calculations. However, the amount of underestimation is likely to be small, and within the bounds already covered by varying the timing and velocity, which have the biggest impact on the ice-sheet thickness change. Furthermore, the effect of this on the resulting GIA signal would be negligible.

The ice loading histories have been constructed using a simple approach which does not incorporate modelling of ice-sheet dynamics. In this region, dynamic ice-sheet models struggle to accurately reproduce fast flow, and models have been specifically adapted to mimic observed behaviour by altering basal sliding conditions (Whitehouse et al., 2012a). Ice-sheet models using a shallow ice approximation (see Section 2.4.1) are not capable of fully reproducing the behaviour of ice streams (Kirchner et al., 2011). Employing a more sophisticated modelling technique, Pollard and DeConto (2012) derived basal sliding iteratively by matching modelled ice-sheet surface elevations to observed ice-sheet surface elevations. However, this method failed to reproduce observed velocities for KIS. In the future, a more detailed reconstruction of the Siple Coast is needed, but will require a more sophisticated ice-sheet model to successfully capture the ice stream behaviour. For the purposes of this study, a simple model approach is sufficient to enable the sensitivity of GIA to Late Holocene perturbations to be investigated.

5.5.2 Ice Loading History Data

Ice-sheet thickness was required to calculate the influx to the ice stream, and was taken from Bedmap2 (Fretwell et al., 2013), a present-day dataset. Using the present-day thickness leads to an overestimation of net ice-thickness increase as ice-sheet thickness determines the rate of influx, but the ice-sheet would have been thinner prior to the

stagnation-related build-up. The effect of this was tested by subtracting the final net ice thickness increase from the initial Bedmap2 ice-sheet thickness for each model. In theory, this would give an estimate of the ice-sheet thickness prior to stagnation of KIS. The ice histories were calculated again with the adjusted Bedmap2 ice thickness and it was found that the maximum ice-sheet thickness change was up to 5 m less, or <5%, compared with the original calculations, which when put into the GIA model will have a negligible effect.

The accumulation rate was used in reconstructing the ice loading history as it contributes to net ice-sheet thickness change down-stream of stagnation where there is no flow to balance mass input to the system. The accumulation rate used was from RACMO2.1/ANT, and it was assumed that the magnitude and spatial pattern remained constant for the whole time period of the stagnation. Any errors due to this assumption would be small and this was tested by calculating the ice loading histories again with double and half the accumulation rate. It was found to make <5% difference to the maximum ice-sheet thickness change for each model, which is well within the bounds captured by the three end-member models.

The present-day elevation change was taken from ICESat data (Pritchard et al., 2009) for the period February 2003 to November 2007. There is elevation change data from the new CryoSat-2, spanning 2010-2014, which is an improvement over ICESat, although the two datasets reveal similar results. As the ice loading histories are constructed up to 2010, it is more consistent to use the ICESat data. The major assumption with this approach is that the spatial pattern of thickening observed by ICESat between 2003 and 2007 has remained the same since the ice stream stopped stagnating. However, there is no way to test this, and no other data to indicate how ice has built up over time.

5.5.3 GIA due to Single KIS Stagnation

When modelling the build-up of ice related to the stagnation of KIS, the GIA model-predicted subsidence varies depending on the combination of ice and Earth model used. For the best estimate ice model with a maximum ice-sheet thickness increase of 100 m, subsidence is in the range -9 to -14 mm/yr for an upper mantle viscosity of 5×10^{19} Pa s, which reduces to -5 to -7 mm/yr for 1×10^{20} Pa s. For an upper mantle viscosity of 5×10^{20} Pa s and higher (e.g. the W12 Earth model), the subsidence is less than -1 mm/yr. The amount of subsidence increases for the ice loading histories with larger

amounts of ice-build-up (UB_300 ice model) and decreases with lower amounts of ice build-up (LB_100 ice model). This demonstrates that there may be a significant present-day GIA signal from stagnation-related ice build-up over the past 165 years, although it heavily depends on the regional upper mantle viscosity. The results of the modelling shows that this recent ice history cannot be neglected from ice-loading models if the upper mantle in this region is less than 1×10^{20} Pa s.

5.5.4 W12+KIS

The ice build-up due to the recent stagnation of KIS was considered in the context of an LGM deglacial model by combining the ice-loading history with the W12 deglacial model. The limitation of this is that only regional GIA can be considered by combining the W12 deglacial history with weaker Earth models, as the fit to relative sea-level data will no longer be preserved.

For the weaker Earth models, much of the uplift signal due to ice changes since the LGM signal has diminished by the present day, and the dominant signal is due to loading on KIS. For an upper mantle viscosity of 5×10^{20} Pa s and higher, the magnitude and spatial pattern of uplift is similar to that of the original W12 uplift as the recent loading on KIS has very little effect (<1 mm/yr) on the present-day uplift. Comparison of GIA model-predicted uplift with the GPS-observed uplift does not reveal much as the GPS sites are not located close enough to KIS to constrain deformation due to stagnation related ice build-up.

5.5.5 Cyclic Models

Evidence exists for multiple stagnation and reactivation cycles on the Siple Coast ice streams (Catania et al., 2012; Hulbe and Fahnestock, 2007), which would cause fluctuations in ice-sheet thickness as ice builds up during stagnation and diminishes on reactivation. To test perturbations to the present-day GIA signal from stagnation and reactivation cycles over a longer time period, two candidate loading models were constructed. The first model added an extra stagnation and reactivation cycle of KIS to the W12+KIS model in the past 1000 years, and the second included stagnation and reactivation of KIS, WIS and MacIS over the past 2000 years, culminating in the most recent stagnation of KIS.

For both ice histories combined with the weaker Earth models, the amount of present-day subsidence was reduced compared with the W12+KIS GIA results, as the uplift

resulting from reactivation of ice streams, and hence ice-mass loss, acted to damp the significant subsidence from the most recent loading on KIS. The addition of loading and unloading on WIS and MacIS did not change the overall magnitude of vertical deformation, but as expected, changed the spatial pattern. There was also a small amount of additional subsidence (up to -1 mm/yr) located in the region of the Ross Ice Shelf caused by consideration of these ice streams, most likely due to their closer proximity to the grounding line than the loading on KIS.

Combining these ice histories with stronger Earth models results in <±0.5 mm/yr difference with the W12+KIS ice history, showing that with an upper mantle viscosity of 5×10^{20} Pa s or higher, present-day uplift is not sensitive to perturbations in ice loading history of this magnitude over the past ~2000 years.

5.5.6 Comparison with Observations

Results from the three LGM to present-day ice loading histories (W12+KIS and KIS and regional cyclic models) combined with three Earth models (weak, medium and the W12 Earth model) were compared with the Gunter et al. (2014) empirical GIA model, which has been derived from observations and is essentially independent of ice or Earth models.

Misfits for the weaker Earth models are dominated by the large subsidence signal at KIS. The absence of this signal from the Gunter et al. (2014) model may indicate that the mantle viscosity in this region is relatively high, greater than 1×10^{20} Pa s. The misfit is reduced slightly with the addition of a longer term (1000-2000) ice history containing cycles of loading and unloading, but remains above 5 mm/yr for all ice histories.

For the W12 Earth model, the misfit of up to 6 mm/yr is dominated by the large uplift centre over the Ross Ice Shelf that is present in the original W12 model (Figure 2.1), and is larger than the uncertainty of the empirical model which peaks at ~2 mm/yr in West Antarctica. This misfit is reduced to <3 mm/yr with the weaker Earth models; however, it is not necessarily the case that a weaker Earth model provides a better fit as the misfit may also be due to errors in the ice history. If the W12 deglacial model has too much ice loss, for example between 20 and 15 ka BP, present-day uplift may be over-estimated. Consequently, the cause of this misfit is not clear. Comparison with the

empirical GIA model of Schön et al. (2014) would reveal larger misfits as they predict consistently lower uplift rates than Gunter et al. (2014) (Section 1.3.3).

The misfits between the GIA model-predicted uplift (for the three ice loading histories W12+KIS, the KIS cyclic model and the regional cyclic model, combined with 3 different Earth models) and the GPS-observed uplift shown in Figure 5.13 are within ±1 mm/yr for two of the five sites considered, and within ±3 mm/yr for a third site. The largest misfits come from CLRK and PATN showing that the model under-predicts uplift by up to 4.5 mm/yr for almost all combinations of ice and Earth models. However, the uncertainty on these uplift rates is high (Table 5.7) so this is not a significant result. The GPS sites used (Argus et al., 2014) are located far from the region of misfit caused by subsidence on KIS and W12 uplift over the Ross Ice Shelf, and have large uncertainties, meaning that the GPS results cannot support or disprove the main conclusions made from comparison with the empirical model.

5.6 Conclusions

Ice streams on the Siple Coast stagnate and reactivate on a century scale which leads to fluctuations in ice-sheet thickness. For the most recent stagnation of KIS ~165 years ago, a simple ice loading history has been constructed. A range of ice-sheet thickness changes has been estimated by varying both the timing and the amount of ice that builds up resulting in between 70 and 130 m ice thickness increase over a period of 148-188 years. These bounds capture uncertainties in the method and data that have been used, although the simple model reconstruction does not take into account the complex ice-sheet dynamics that occur in this region.

GIA model-predicted vertical deformation in response to the stagnation of KIS is up to -17 mm/yr depending on the combination of ice and Earth model used, showing that this recent event may contribute significantly to the present-day GIA signal if the upper mantle viscosity in this region is low (5×10^{19} Pa s). For an upper mantle viscosity of 1×10^{20} Pa s this decreases to -4 to -8 mm/yr, and for a viscosity of 5×10^{20} Pa s, which is within the suggested by A et al. (2013), subsidence is less than 1 mm/yr. Similarly, a higher upper mantle viscosity, such as that used by Whitehouse et al. (2012b) (1×10^{21} Pa s) would result in <1 mm/yr subsidence.

Testing this recent ice loading in the context of the W12 deglacial model shows that, for a weak Earth model, much of the LGM signal has diminished and present-day uplift is

dominated by subsidence over KIS. For the stronger Earth models, the resulting magnitude and spatial pattern of uplift is almost identical to the original W12 model. Introducing ice loading fluctuations over the last 1000-2000 years reduces the amount of subsidence at the present-day for the weak Earth models only, due to uplift relating to unloading several hundred years ago. However, for the stronger Earth models these additional loading events make very little difference.

Comparing the GIA model predictions with an empirical GIA model shows misfits that are dominated by the subsidence at KIS for the weaker Earth models, and the large uplift centre over the Ross Ice Shelf for the stronger Earth models. The absence of any large subsidence in the empirical model suggests that the upper mantle viscosity is above 1×10^{20} Pa s. Misfits between these two models may be caused by several factors. First, there may be other Late Holocene ice-mass changes that have not been included in the modelling performed here, such as loading/unloading on the other ice streams in the region. Second, the W12 deglacial history may contain too much ice loss between LGM and present, or the load centre is in the wrong place, which may be resulting in over-prediction of uplift over the Ross Ice Shelf. Limiting the modelling to a linear rheology may also be affecting the results, and the use of non-linear or transient rheology may improve the fit. Finally, not including a 3-D Earth structure in the GIA modelling is likely to have an impact in this area as it lies close to the boundary with East Antarctica where the upper mantle viscosity is believed to be much higher.

Late Holocene ice changes related to stagnation and reactivation of ice streams on the Siple Coast may be important in GIA models, and could perturb the present-day uplift signal significantly if the mantle viscosity is low in this region. However, other factors such as 3-D Earth structure and LGM deglacial history also need to be considered in order to improve GIA models in this region. In the future, an ice-sheet model reconstruction of this region would enable a more detailed loading history to be derived, including ice loading changes due to stagnation and reactivation of the other ice streams. Furthermore, an examination of GPS-observed horizontal rates may help to constrain GIA-related deformation in this region, but due to its proximity to East Antarctica and the likely differences in Earth structure, this would likely only be insightful if using a 3-D GIA model.

Chapter 6. Conclusions

The work presented in this thesis sought to investigate deficiencies in millennial-scale GIA models arising from omission of Late Holocene and present-day Antarctic ice-mass change. The focus was on the Antarctic Peninsula and Siple Coast regions of West Antarctica. This chapter summarises the work completed toward achieving each of the three aims and highlights the main results. The overall conclusions are presented in Section 6.2 and suggestions for future work are made in Section 6.3.

6.1 Summary of Work

6.1.1 Antarctic Peninsula

In the Antarctic Peninsula (AP), Glacial Isostatic Adjustment (GIA) models tend to over-predict uplift when compared with low GPS-observed uplift rates (Thomas et al., 2011). Whitehouse et al. (2012b) improved the fit between modelled and observed uplift by including additional loading in the last 1000 years of an LGM deglacial history. The work described in Chapter 3 investigated the possible GIA signal from recent loading related to a centennial increase in accumulation, and its potential for explaining GPS observations of low uplift rates observed in the southern AP.

An increase in accumulation since the 1850s has been observed in ice cores, most notably in the Gomez ice core on the western Peninsula. An accumulation history was reconstructed to provide mass balance forcing for an ice-sheet model. In response to the accumulation history, up to 45 m of ice-sheet thickening over the past 155 years was predicted. This results in modelled GIA subsidence rates of around 3-4 mm/yr for Earth models considered appropriate for the northern and southern Peninsula, with a spatially variable pattern predicting more subsidence on the west than the east. GRACE-determined rates of ice-mass change are biased slightly low for this region as a result of omitting the accumulation-related signal, which is not currently included in Antarctic GIA models.

6.1.2 Northern Antarctic Peninsula

The upper mantle viscosity in the Antarctic Peninsula is considered to be much lower than the rest of West Antarctica, however this remains uncertain. The work presented in Chapter 4 attempted to place bounds on a regional Earth model for the northern

Antarctic Peninsula using GPS-observed uplift and a high resolution dataset of present-day ice-mass loss on a decadal scale.

The breakup of ice shelves in 1995 and 2002 led to ice-mass loss from tributary glaciers, invoking a solid Earth response that can be observed in GPS records. Non-linear uplift observed at Palmer station cannot be explained by a purely elastic response, but a four layer viscoelastic model can produce a good fit to the time series. Using all seven GPS time series in the area, the upper mantle viscosity was robustly constrained to be less than 2×10^{18} Pa s, and the lithospheric thickness to be 100-140 km, although the latter remains less well constrained. The range of values for upper mantle viscosity is much lower than previously suggested for this region but is consistent with the back-arc tectonic setting. A more complex Earth structure or a transient/non-linear rheology may provide an equally good fit to the data, but at present neither is required to explain the existing data. Furthermore, an elastic response to variations in SMB may improve the fit between modelled uplift and GPS-observed uplift, but at present is limited by the resolution and time span of SMB model data.

6.1.3 Siple Coast

In the Siple Coast region of Antarctica, century-scale stagnation and reactivation of ice streams causes localised thickening and thinning of the ice sheet over the last 1000 years or longer. In Chapter 5, potential perturbations to the present-day GIA signal from these fluctuations in ice-sheet thickness were investigated. The most recent stagnation of Kamb Ice Stream (KIS) ~165 years ago is likely to have caused thickening of the ice sheet of up to 70-130 m. Modelled in isolation this loading results in up to 17 mm/yr subsidence at the present-day, but predictions are heavily dependent on the Earth model adopted. Combining this ice loading with the W12 deglacial history shows that for a weak Earth model the present-day uplift is dominated by the recent subsidence on KIS. Introducing ice loading and unloading cycles over the last 1000-2000 years reduces the amount of present-day subsidence slightly. For stronger Earth models, such as the W12 Earth model, the recent loading changes investigated do not make more than ±1 mm/yr difference to the present-day signal.

Comparing the GIA model results from the longer term ice loading histories with an empirically-derived GIA model (Gunter et al., 2014) reveals large misfits over KIS for the weaker Earth models and over the Ross Ice Shelf for the stronger Earth models. The absence of large subsidence over KIS in the empirical model suggests the Earth is

strong enough in this region that this signal does not matter. Furthermore, there is no evidence for large uplift on the Ross Ice Shelf from the empirical model or from GRACE data (King et al., 2012a). These misfits may be due to a combination of missing Late Holocene ice changes, errors in the W12 deglacial history and limitations of using a 1-D Earth model.

6.2 Conclusions

- Ice-mass changes over the past few hundred to thousand years cannot be neglected from Antarctic GIA models, as they may dominate the present-day signal in regions of low viscosity upper mantle such as the Antarctic Peninsula.
- The northern Antarctic Peninsula has lower viscosity mantle than previously thought and a viscoelastic response to decadal ice-mass changes must be considered before GPS observations can be used to constrain longer-term glacial isostatic adjustment in this region. It is likely that the LGM signal has diminished and present-day deformation reflects ice changes only in the last few thousand years at most.
- Recent loading may perturb GPS-observed uplift in low viscosity regions, and therefore they cannot be used to constrain GIA models unless these recent changes have been included in the model.
- Low viscosity regions are often misrepresented in 1-D GIA models that use a higher viscosity as a continent-wide average. This means resulting GIA model predictions are inaccurate.
- In the Siple Coast region, the upper mantle viscosity may not be as low as much of West Antarctica, and loading change over the past few hundred years may be insignificant.
- Current models of GIA from the Siple Coast show large misfits compared to GPS observations and empirically derived GIA, highlighting errors in current LGM deglacial models, which need addressing in future GIA models.
- There is a clear need for more constraints on Late Holocene ice-sheet evolution to drive high resolution ice-sheet and GIA modelling.
- New advances in 3-D GIA modelling will allow low viscosity regions to be modelled more accurately as part of a continent-wide Antarctic GIA model and using horizontal as well as vertical GPS deformation rates will help to constrain these models.

6.3 Suggestions for Future Work

One of the limitations faced, particularly for the work presented in Chapter 3, is the availability of observational data, and resolution of model data used in the work. The reconstructed accumulation history used to drive the ice-sheet model was based on the RACMO2.1/ANT SMB model at 27 km resolution. Whilst this is considered high resolution for Antarctic studies, it is somewhat coarse compared to the narrow glaciers and steep topography of the Antarctic Peninsula. It is suggested that this work could be repeated utilising the forthcoming higher resolution (5 km) RACMO SMB model, when this becomes available. Furthermore, this work would benefit from the addition of the accumulation history from the LARISSA Site Beta ice core (Zagorodnov et al., 2012) when published in the near future. This would allow a more accurate reconstruction of accumulation history for ice-sheet modelling purposes.

Similarly, the work in Chapter 4 could be repeated in the future using longer GPS time series, and the additional GPS sites that have been recently installed. A more spatially extensive GPS network might enable a more complex Earth structure or rheology to be resolved and firmer bounds to be placed on the lithospheric thickness. DEM differencing over a longer period than used in this study would improve the ice-mass change data and may further refine the Earth model, particularly if changes in the rate of ice-mass loss are detected. As shown in Section 4.5.6, including an elastic vertical deformation in response to SMB anomalies resulted in an improved fit between model-predicted time series and GPS-observed time series. Once the higher resolution and longer time span SMB dataset becomes available, an interesting study would be to examine the presence of an elastic response to SMB anomalies in the GPS time series. This may be applicable throughout Antarctica and not restricted to the northern Antarctic Peninsula.

The work completed in Chapter 5 shows that models of GIA would greatly benefit from an ice-sheet model reconstruction of the Siple Coast region for the past few thousand years. This would enable a more detailed and accurate loading history to be reconstructed, including loading and unloading of all the ice streams along this coast. This would require the use of a more sophisticated ice-sheet model which is capable of representing ice stream flow. GPS-observed horizontal rates could also be used to further constrain GIA in the Siple Coast and Ross Ice Shelf area, although this is only likely to be meaningful if lateral variations in Earth structure are included in the GIA

model. Horizontal motion is likely to be significantly affected by the contrast in mantle viscosity between West and East Antarctica in this region as it lies so close to the boundary. Forthcoming results from seismic studies of West Antarctica will give a stronger indication of the likely Earth structure, and further improve GIA models of the region.

Finally, it is hoped that the work presented here acts as a spring board for the next generation of Antarctic GIA models. Regions particularly sensitive to Late Holocene ice-mass changes have been highlighted, and the potential signal that may go unmodelled by omitting these has been quantified. The effect of Late Holocene changes on GIA must also be considered in other regions of West Antarctica where the upper mantle viscosity may be low, such as the well-studied Amundsen Sea sector (e.g. Groh et al., 2012). Including these changes in the context of an LGM deglacial history would be the first step forward, but a GIA model capable of modelling lateral variations in Earth structure is needed to fully explore the implications.

Appendix: List of Mathematical Symbols

Symbol	Meaning	Value (where applicable)
a	Radius of the Earth	6371 km
A	Flow law coefficient	
A_o	Area of the ocean	
C	Covariance matrix	
E	Eigenvectors	
G_Φ	Green's function for gravitational potential	
G_s	Sea-level Green's function	
G_u	Green's function for vertical deformation	
h	Ice thickness	
h_l	Love number for vertical displacement	
h_l^e	Elastic Love number for vertical displacement	
h_{lj}	Viscoelastic Love number for vertical displacement	
H	Diagonal operator matrix	
$H(t)$	Heaviside step function	1 for t≥0; 0 for t<0
I	Ice load	
k_l	Love number for gravitational potential	
k_l^e	Elastic Love number for gravitational potential	
k_{lj}	Viscoelastic Love number for gravitational potential	
l	Spherical harmonic degree	
m_e	Mass of the Earth	5.9726×10^{24} kg
m_i	Mass of ice	
M	Viscoelastic mode	
n	Flow law exponent	3
$P_l(cos\theta)$	Legendre Polynomial	
R	Error	
S	Relative sea-level change, or ocean load	
t	Time	
T^0	Vector of observations	
T_{lj}	Relaxation time	
$\boldsymbol{u}$	Velocity	
u	Vertical deformation	
α	Ice surface slope	
γ	Gravitational acceleration	$9.81\ m/s^2$
$\delta(t)$	Dirac's delta	
ε	Strain rate	
η	Viscosity	
θ	Colatitude	
λ	Longitude	

Λ	Eigenvalues	
ρ_i	Density of ice	917 kg/m^3
ρ_w	Density of water	999 kg/m^3
Σ	Diagonal matrix representing the instrumental error	
τ_b	Basal shear stress	
Φ	Gravitational potential	
ψ	Time series of amplitudes of the EOFs	

References

A, G., Wahr, J. and Zhong, S. (2013) 'Computations of the viscoelastic response of a 3-D compressible Earth to surface loading: an application to Glacial Isostatic Adjustment in Antarctica and Canada', *Geophysical Journal International*, 192, (2), pp. 557-572.

Argus, D. F., Peltier, W. R., Drummond, R. and Moore, A. W. (2014) 'The Antarctica component of postglacial rebound model ICE-6G_C (VM5a) based on GPS positioning, exposure age dating of ice thicknesses, and relative sea level histories', *Geophysical Journal International*.

Aristarain, A., Delmas, R. and Stievenard, M. (2004) 'Ice-Core Study of the Link between Sea-Salt Aerosol, Sea-Ice Cover and Climate in the Antarctic Peninsula Area', *Climatic Change*, 67, (1), pp. 63-86.

Auriac, A., Spaans, K. H., Sigmundsson, F., Hooper, A., Schmidt, P. and Lund, B. (2013) 'Iceland rising: Solid Earth response to ice retreat inferred from satellite radar interferometry and visocelastic modeling', *Journal of Geophysical Research: Solid Earth*, 118, (4), pp. 1331-1344.

Barker, D. H. N., Christeson, G. L., Austin, J. A. and Dalziel, I. W. D. (2003) 'Backarc basin evolution and cordilleran orogenesis: Insights from new ocean-bottom seismograph refraction profiling in Bransfield Strait, Antarctica', *Geology*, 31, (2), pp. 107-110.

Barker, P. F. (1982) 'The Cenozoic subduction history of the Pacific margin of the Antarctic Peninsula: ridge crest–trench interactions', *Journal of the Geological Society*, 139, (6), pp. 787-801.

Barker, P. F. (2001) 'Scotia Sea regional tectonic evolution: implications for mantle flow and palaeocirculation', *Earth-Science Reviews*, 55, (1–2), pp. 1-39.

Barker, P. F., Dalziel, I. W. D. and Storey, B. C. (1991) 'Tectonic Development of the Scotia Arc Region', in Tingey, R. J.(ed), *The Geology of Antarctica.*Oxford University Press, pp. 215-248.

Barletta, V. R. and Bordoni, A. (in prep.) 'High resolution Post Glacial Rebound over the European Alps', *manuscript in preparation*.

Barletta, V. R., Ferrari, C., Diolaiuti, G., Carnielli, T., Sabadini, R. and Smiraglia, C. (2006) 'Glacier shrinkage and modeled uplift of the Alps', *Geophys. Res. Lett.,* 33, (14), pp. L14307.

Bassett, S. E., Milne, G. A., Bentley, M. J. and Huybrechts, P. (2007) 'Modelling Antarctic sea-level data to explore the possibility of a dominant Antarctic contribution to meltwater pulse IA', *Quaternary Science Reviews,* 26, (17–18), pp. 2113-2127.

Beem, L. H., Tulaczyk, S. M., King, M. A., Bougamont, M., Fricker, H. A. and Christoffersen, P. (2014) 'Variable deceleration of Whillans Ice Stream, West Antarctica', *Journal of Geophysical Research: Earth Surface,* pp. n/a-n/a.

Benn, D. I. and Evans, D. J. A. (1998) *Glaciers and Glaciation.* London: Arnold.

Bentley, M. J. (1999) 'Volume of Antarctic Ice at the Last Glacial Maximum, and its impact on global sea level change', *Quaternary Science Reviews,* 18, (14), pp. 1569-1595.

Bentley, M. J. (2010) 'The Antarctic palaeo record and its role in improving predictions of future Antarctic Ice Sheet change', *Journal of Quaternary Science,* 25, (1), pp. 5-18.

Bentley, M. J., Fogwill, C. J., Kubik, P. W. and Sugden, D. E. (2006) 'Geomorphological evidence and cosmogenic 10Be/26Al exposure ages for the Last Glacial Maximum and deglaciation of the Antarctic Peninsula Ice Sheet', *Geological Society of America Bulletin,* 118, (9-10), pp. 1149-1159.

Bentley, M. J., Hodgson, D. A., Sugden, D. E., Roberts, S. J., Smith, J. A., Leng, M. J. and Bryant, C. (2005) 'Early Holocene retreat of the George VI Ice Shelf, Antarctic Peninsula', *Geology,* 33, (3), pp. 173-176.

Berthier, E., Scambos, T. A. and Shuman, C. A. (2012) 'Mass loss of Larsen B tributary glaciers (Antarctic Peninsula) unabated since 2002', *Geophys. Res. Lett.,* 39, (13), pp. L13501.

Bevis, M., Kendrick, E., Smalley, R., Jr., Dalziel, I., Caccamise, D., Sasgen, I., Helsen, M., Taylor, F. W., Zhou, H., Brown, A., Raleigh, D., Willis, M., Wilson, T. and Konfal, S. (2009) 'Geodetic measurements of vertical crustal velocity in West

Antarctica and the implications for ice mass balance', *Geochem. Geophys. Geosyst.,* 10, (10), pp. Q10005.

Bevis, M., Wahr, J., Khan, S. A., Madsen, F. B., Brown, A., Willis, M., Kendrick, E., Knudsen, P., Box, J. E., van Dam, T., Caccamise, D. J., Johns, B., Nylen, T., Abbott, R., White, S., Miner, J., Forsberg, R., Zhou, H., Wang, J., Wilson, T., Bromwich, D. and Francis, O. (2012) 'Bedrock displacements in Greenland manifest ice mass variations, climate cycles and climate change', *Proceedings of the National Academy of Sciences,* 109, (30), pp. 11944-11948.

Bradley, S. L., Milne, G. A., Shennan, I. and Edwards, R. (2011) 'An improved glacial isostatic adjustment model for the British Isles', *Journal of Quaternary Science,* 26, (5), pp. 541-552.

Bueler, E., Lingle, C. S., Kallen-Brown, J. A., Covey, D. N. and Bowman, L. N. (2005) 'Exact solutions and verification of numerical models for isothermal ice sheets', *Journal of Glaciology,* 51, (173), pp. 291-306.

Calafat, F. M. and Jordà, G. (2011) 'A Mediterranean sea level reconstruction (1950–2008) with error budget estimates', *Global and Planetary Change*, 79, (1–2), pp. 118-133.

Catania, G., Hulbe, C., Conway, H., Scambos, T. A. and Raymond, C. F. (2012) 'Variability in the mass flux of the Ross ice streams, West Antarctica, over the last millennium', *Journal of Glaciology,* 58, (210), pp. 741-752.

Catania, G. A., Scambos, T. A., Conway, H. and Raymond, C. F. (2006) 'Sequential stagnation of Kamb Ice Stream, West Antarctica', *Geophys. Res. Lett.,* 33, (14), pp. L14502.

Church, J. A., White, N. J., Coleman, R., Lambeck, K. and Mitrovica, J. X. (2004) 'Estimates of the Regional Distribution of Sea Level Rise over the 1950–2000 Period', *Journal of Climate,* 17, (13), pp. 2609-2625.

Clark, P. U., Dyke, A. S., Shakun, J. D., Carlson, A. E., Clark, J., Wohlfarth, B., Mitrovica, J. X., Hostetler, S. W. and McCabe, A. M. (2009) 'The Last Glacial Maximum', *Science*, 325, (5941), pp. 710-714.

Conway, H., Hall, B. L., Denton, G. H., Gades, A. M. and Waddington, E. D. (1999) 'Past and future grounding-line retreat of the West Antarctic Ice Sheet', *Science,* 286, (5438), pp. 280-283.

Cook, A. J., Fox, A. J., Vaughan, D. G. and Ferrigno, J. G. (2005) 'Retreating Glacier Fronts on the Antarctic Peninsula over the Past Half-Century', *Science,* 308, (5721), pp. 541-544.

Cook, A. J., Murray, T., Luckman, A., Vaughan, D. G. and Barrand, N. E. (2012) 'A new 100-m Digital Elevation Model of the Antarctic Peninsula derived from ASTER Global DEM: methods and accuracy assessment', *Earth Syst. Sci. Data,* 4, (1), pp. 129-142.

Cook, A. J. and Vaughan, D. G. (2010) 'Overview of areal changes of the ice shelves on the Antarctic Peninsula over the past 50 years', *Cryosphere,* 4, (1), pp. 77-98.

De Angelis, H. and Skvarca, P. (2003) 'Glacier Surge After Ice Shelf Collapse', *Science,* 299, (5612), pp. 1560-1562.

Dixon, J. E., Dixon, T. H., Bell, D. R. and Malservisi, R. (2004) 'Lateral variation in upper mantle viscosity: role of water', *Earth and Planetary Science Letters,* 222, (2), pp. 451-467.

Dziewonski, A. M. and Anderson, D. L. (1981) 'Preliminary reference Earth model', *Physics of the Earth and Planetary Interiors,* 25, (4), pp. 297-356.

Fairbanks, R. G. (1989) 'A 17,000-year glacio-eustatic sea level record: influence of glacial melting rates on the Younger Dryas event and deep-ocean circulation', *Nature,* 342, (6250), pp. 637-642.

Farrell, W. E. and Clark, J. A. (1976) 'On Postglacial Sea Level', *Geophysical Journal of the Royal Astronomical Society,* 46, (3), pp. 647-667.

Fox Maule, C., Purucker, M. E., Olsen, N. and Mosegaard, K. (2005) 'Heat Flux Anomalies in Antarctica Revealed by Satellite Magnetic Data', *Science,* 309, (5733), pp. 464-467.

Freed, A. M., Bürgmann, R., Calais, E. and Freymueller, J. (2006) 'Stress-dependent power-law flow in the upper mantle following the 2002 Denali, Alaska, earthquake', *Earth and Planetary Science Letters,* 252, (3–4), pp. 481-489.

Fretwell, P., Pritchard, H. D., Vaughan, D. G., Bamber, J. L., Barrand, N. E., Bell, R., Bianchi, C., Bingham, R. G., Blankenship, D. D., Casassa, G., Catania, G., Callens, D., Conway, H., Cook, A. J., Corr, H. F. J., Damaske, D., Damm, V., Ferraccioli, F., Forsberg, R., Fujita, S., Gim, Y., Gogineni, P., Griggs, J. A., Hindmarsh, R. C. A., Holmlund, P., Holt, J. W., Jacobel, R. W., Jenkins, A., Jokat, W., Jordan, T., King, E. C., Kohler, J., Krabill, W., Riger-Kusk, M., Langley, K. A., Leitchenkov, G., Leuschen, C., Luyendyk, B. P., Matsuoka, K., Mouginot, J., Nitsche, F. O., Nogi, Y., Nost, O. A., Popov, S. V., Rignot, E., Rippin, D. M., Rivera, A., Roberts, J., Ross, N., Siegert, M. J., Smith, A. M., Steinhage, D., Studinger, M., Sun, B., Tinto, B. K., Welch, B. C., Wilson, D., Young, D. A., Xiangbin, C. and Zirizzotti, A. (2013) 'Bedmap2: improved ice bed, surface and thickness datasets for Antarctica', *The Cryosphere,* 7, (1), pp. 375-393.

Gomez, N., Pollard, D. and Mitrovica, J. X. (2013) 'A 3-D coupled ice sheet – sea level model applied to Antarctica through the last 40 ky', *Earth and Planetary Science Letters,* 384, (0), pp. 88-99.

Greve, R. and Blatter, H. (2009) *Dynamics of ice sheets and glaciers.* Dordrecht: Springer.

Groh, A., Ewert, H., Scheinert, M., Fritsche, M., Rülke, A., Richter, A., Rosenau, R. and Dietrich, R. (2012) 'An investigation of Glacial Isostatic Adjustment over the Amundsen Sea sector, West Antarctica', *Global and Planetary Change,* 98–99, (0), pp. 45-53.

Gunter, B. C., Didova, O., Riva, R. E. M., Ligtenberg, S. R. M., Lenaerts, J. T. M., King, M. A., van den Broeke, M. R. and Urban, T. (2014) 'Empirical estimation of present-day Antarctic glacial isostatic adjustment and ice mass change', *The Cryosphere,* 8, (2), pp. 743-760.

Heroy, D. C. and Anderson, J. B. (2007) 'Radiocarbon constraints on Antarctic Peninsula Ice Sheet retreat following the Last Glacial Maximum (LGM)', *Quaternary Science Reviews,* 26, (25–28), pp. 3286-3297.

Hulbe, C. and Fahnestock, M. (2007) 'Century-scale discharge stagnation and reactivation of the Ross ice streams, West Antarctica', *J. Geophys. Res.*, 112, (F3), pp. F03S27.

Hulbe, C. L., Scambos, T. A., Lee, C.-K., Bohlander, J. and Haran, T. (2013) 'Recent changes in the flow of the Ross Ice Shelf, West Antarctica', *Earth and Planetary Science Letters,* 376, (0), pp. 54-62.

Huybrechts, P., Payne, A. J. and Group, E. I. (1996) 'The EISMINT benchmarks for testing ice-sheet models', *Annals of Glaciology,* 23, pp. 1-12.

Ivins, E. R. and James, T. S. (2005) 'Antarctic glacial isostatic adjustment: a new assessment', *Antarctic Science,* 17, (04), pp. 541-553.

Ivins, E. R., James, T. S., Wahr, J., O. Schrama, E. J., Landerer, F. W. and Simon, K. M. (2013) 'Antarctic contribution to sea level rise observed by GRACE with improved GIA correction', *Journal of Geophysical Research: Solid Earth*, pp. n/a-n/a.

Ivins, E. R., Raymond, C. A. and James, T. S. (2000) 'The influence of 5000 year-old and younger glacial mass variability on present-day crustal rebound in the Antarctic Peninsula', *Earth, Planets and Space,* 52, (11), pp. 1023-1029.

Ivins, E. R. and Sammis, C. G. (1996) 'Transient creep of a composite lower crust: 1. Constitutive theory', *Journal of Geophysical Research: Solid Earth,* 101, (B12), pp. 27981-28004.

Ivins, E. R., Watkins, M. M., Yuan, D.-N., Dietrich, R., Casassa, G. and Rülke, A. (2011) 'On-land ice loss and glacial isostatic adjustment at the Drake Passage: 2003-2009', *J. Geophys. Res.,* 116, (B2), pp. B02403.

Joughin, I., Bindschadler, R. A., King, M. A., Voigt, D., Alley, R. B., Anandakrishnan, S., Horgan, H., Peters, L., Winberry, P., Das, S. B. and Catania, G. (2005) 'Continued deceleration of Whillans Ice Stream, West Antarctica', *Geophys. Res. Lett.,* 32, (22), pp. L22501.

Joughin, I. and Tulaczyk, S. (2002) 'Positive Mass Balance of the Ross Ice Streams, West Antarctica', *Science,* 295, (5554), pp. 476-480.

Kaplan, A., Kushnir, Y. and Cane, M. A. (2000) 'Reduced Space Optimal Interpolation of Historical Marine Sea Level Pressure: 1854–1992*', *Journal of Climate,* 13, (16), pp. 2987-3002.

Kaplan, A., Kushnir, Y., Cane, M. A. and Blumenthal, M. B. (1997) 'Reduced space optimal analysis for historical data sets: 136 years of Atlantic sea surface temperatures', *Journal of Geophysical Research: Oceans*, 102, (C13), pp. 27835-27860.

Kaspari, S., Mayewski, P. A., Dixon, D. A., Spikes, V. B., Sneed, S. B., Handley, M. J. and Hamilton, G. S. (2004) 'Climate variability in West Antarctica derived from annual accumulation-rate records from ITASE firn/ice cores', *Annals of Glaciology*, 39, (1), pp. 585-594.

Kaufmann, G., Wu, P. and Ivins, E. R. (2005) 'Lateral viscosity variations beneath Antarctica and their implications on regional rebound motions and seismotectonics', *Journal of Geodynamics*, 39, (2), pp. 165-181.

Kendall, R. A., Mitrovica, J. X. and Milne, G. A. (2005) 'On post-glacial sea level – II. Numerical formulation and comparative results on spherically symmetric models', *Geophysical Journal International*, 161, (3), pp. 679-706.

King, M., Altamimi, Z., Boehm, J., Bos, M., Dach, R., Elosegui, P., Fund, F., Hernández-Pajares, M., Lavallee, D., Mendes Cerveira, P., Penna, N., Riva, R., Steigenberger, P., van Dam, T., Vittuari, L., Williams, S. and Willis, P. (2010) 'Improved Constraints on Models of Glacial Isostatic Adjustment: A Review of the Contribution of Ground-Based Geodetic Observations', *Surveys in Geophysics*, 31, (5), pp. 465-507.

King, M. A. (2013) 'Progress in modelling and observing Antarctic glacial isostatic adjustment', *Astronomy & Geophysics*, 54, (4), pp. 4.33-4.38.

King, M. A., Bingham, R. J., Moore, P., Whitehouse, P. L., Bentley, M. J. and Milne, G. A. (2012a) 'Lower satellite-gravimetry estimates of Antarctic sea-level contribution', *Nature*, 491, (7425), pp. 586-589.

King, M. A., Bingham, R. J., Moore, P., Whitehouse, P. L., Bentley, M. J. and Milne, G. A. (2012b) 'Lower satellite-gravimetry estimates of Antarctic sea-level contribution', *Nature*, advance online publication.

Kirchner, N., Hutter, K., Jakobsson, M. and Gyllencreutz, R. (2011) 'Capabilities and limitations of numerical ice sheet models: a discussion for Earth-scientists and modelers', *Quaternary Science Reviews*, 30, (25–26), pp. 3691-3704.

Kogan, M. G., Vasilenko, N. F., Frolov, D. I., Freymueller, J. T., Steblov, G. M., Prytkov, A. S. and Ekström, G. (2013) 'Rapid postseismic relaxation after the great 2006–2007 Kuril earthquakes from GPS observations in 2007–2011', *Journal of Geophysical Research: Solid Earth,* 118, (7), pp. 3691-3706.

Kunz, M., King, M. A., Mills, J. P., Miller, P. E., Fox, A. J., Vaughan, D. G. and Marsh, S. H. (2012) 'Multi-decadal glacier surface lowering in the Antarctic Peninsula', *Geophys. Res. Lett.*, 39, (19), pp. L19502.

Lange, H., Casassa, G., Ivins, E. R., Schröder, L., Fritsche, M., Richter, A., Groh, A. and Dietrich, R. (2014) 'Observed crustal uplift near the Southern Patagonian Icefield constrains improved viscoelastic Earth Models', *Geophysical Research Letters*, pp. 2013GL058419.

LARsen Ice Shelf System, A. L. (http://www.hamilton.edu/expeditions/larissa) *LARsen Ice Shelf System, Antarctica (LARISSA)*. Available at: http://www.hamilton.edu/expeditions/larissa (Accessed: 28 Aug 2013).

Larter, R. D., Rebesco, M., Vanneste, L. E., GambôA, L. A. P. and Barker, P. F. (1997) 'Cenozoic Tectonic, Sedimentary and Glacial History of the Continental Shelf West Of Graham Land, Antarctic Peninsula', in Barker, P. F. and Cooper, A. K.(eds) *Geology and Seismic Stratigraphy of the Antarctic Margin, 2.*Washington, D. C: American Geophysical Union, pp. 1-27.

Le Brocq, A. M., Bentley, M. J., Hubbard, A., Fogwill, C. J., Sugden, D. E. and Whitehouse, P. L. (2011) 'Reconstructing the Last Glacial Maximum ice sheet in the Weddell Sea embayment, Antarctica, using numerical modelling constrained by field evidence', *Quaternary Science Reviews,* 30, (19-20), pp. 2422-2432.

Le Brocq, A. M., Payne, A. J. and Vieli, A. (2010) 'An improved Antarctic dataset for high resolution numerical ice sheet models (ALBMAP v1)', *Earth Syst. Sci. Data,* 2, (2), pp. 247-260.

Le Meur, E. and Hindmarsh, R. C. A. (2000) 'A comparison of two spectral approaches for computing the Earth response to surface loads', *Geophysical Journal International*, 141, (2), pp. 282-298.

Le Meur, E. and Huybrechts, P. (1996) 'A comparison of different ways of dealing with isostasy: examples from modeling the Antarctic ice sheet during the last glacial cycle', *Annals of Glaciology,* 23, pp. 309-317.

Lenaerts, J. T. M., van den Broeke, M. R., van de Berg, W. J., van Meijgaard, E. and Kuipers Munneke, P. (2012) 'A new, high-resolution surface mass balance map of Antarctica (1979-2010) based on regional atmospheric climate modeling', *Geophys. Res. Lett.,* 39, (4), pp. L04501.

Leysinger Vieli, G. J. M. C. and Gudmundsson, G. H. (2004) 'On estimating length fluctuations of glaciers caused by changes in climatic forcing', *Journal of Geophysical Research: Earth Surface,* 109, (F1), pp. F01007.

Lidberg, M., Johansson, J., Scherneck, H.-G. and Davis, J. (2007) 'An improved and extended GPS-derived 3D velocity field of the glacial isostatic adjustment (GIA) in Fennoscandia', *Journal of Geodesy,* 81, (3), pp. 213-230.

Lythe, M. B. and Vaughan, D. G. (2001) 'BEDMAP: A new ice thickness and subglacial topographic model of Antarctica', *Journal of Geophysical Research: Solid Earth,* 106, (B6), pp. 11335-11351.

Martin, P. J. and Peel, D. A. (1978) 'The spatial distribution of 10m temperatures in the Antarctic Peninsula', *Journal of Glaciology,* 20, pp. 311-317.

McMillan, M., Shepherd, A., Sundal, A., Briggs, K., Muir, A., Ridout, A., Hogg, A. and Wingham, D. (2014) 'Increased ice losses from Antarctica detected by CryoSat-2', *Geophysical Research Letters,* pp. 2014GL060111.

Miles, G. M., Marshall, G. J., McConnell, J. R. and Aristarain, A. J. (2008) 'Recent accumulation variability and change on the Antarctic Peninsula from the ERA40 reanalysis', *International Journal of Climatology,* 28, (11), pp. 1409-1422.

Milne, G. A. and Mitrovica, J. X. (1996) 'Postglacial sea-level change on a rotating Earth: first results from a gravitationally self-consistent sea-level equation', *Geophysical Journal International,* 126, (3), pp. F13-F20.

Mitrovica, J. X. and Milne, G. A. (2003) 'On post-glacial sea level: I. General theory', *Geophysical Journal International,* 154, (2), pp. 253-267.

Mitrovica, J. X., Wahr, J., Matsuyama, I. and Paulson, A. (2005) 'The rotational stability of an ice-age earth', *Geophysical Journal International,* 161, (2), pp. 491-506.

Morelli, A. and Danesi, S. (2004) 'Seismological imaging of the Antarctic continental lithosphere: a review', *Global and Planetary Change,* 42, (1-4), pp. 155-165.

Mosley-Thompson, E. (1992) 'Paleoenvironmental conditions in Antarctica since A.D. 1500: Ice core evidence', in Bradley, R. S. and Jones, P. D.(eds) *Climate since A.D. 1500.*London: Routledge, pp. 572-591.

Mulvaney, R., Abram, N. J., Hindmarsh, R. C. A., Arrowsmith, C., Fleet, L., Triest, J., Sime, L. C., Alemany, O. and Foord, S. (2012) 'Recent Antarctic Peninsula warming relative to Holocene climate and ice-shelf history', *Nature,* 489, (7414), pp. 141-144.

Ng, F. and Conway, H. (2004) 'Fast-flow signature in the stagnated Kamb Ice Stream, West Antarctica', *Geology,* 32, (6), pp. 481-484.

Nield, G. A., Barletta, V. R., Bordoni, A., King, M. A., Whitehouse, P. L., Clarke, P. J., Domack, E. W., Scambos, T. A. and Berthier, E. (2014) 'Rapid bedrock uplift in the Antarctic Peninsula explained by viscoelastic response to recent ice unloading', *Earth and Planetary Science Letters,* in revision.

Nield, G. A., Whitehouse, P. L., King, M. A., Clarke, P. J. and Bentley, M. J. (2012) 'Increased ice loading in the Antarctic Peninsula since the 1850s and its effect on glacial isostatic adjustment', *Geophys. Res. Lett.,* 39, (17), pp. L17504.

Park, Y., Kim, K.-H., Lee, J., Yoo, H. J. and Plasencia L, M. P. (2012) 'P-wave velocity structure beneath the northern Antarctic Peninsula: evidence of a steeply subducting slab and a deep-rooted low-velocity anomaly beneath the central Bransfield Basin', *Geophysical Journal International,* 191, (3), pp. 932-938.

Payne, A. J., Huybrechts, P., Abe-Ouchi, A., Calov, R., Fastook, J. L., Greve, R., Marshall, S. J., Marsiat, I., Ritz, C., Tarasov, L. and Thomassen, M. P. A. (2000) 'Results from the EISMINT model intercomparison: the effects of thermomechanical coupling', *Journal of Glaciology,* 46, (153), pp. 227-238.

Peel, D. A. (1992) 'Ice core evidence from the Antarctic Peninsula region', in Bradley, R. S. and Jones, P. D.(eds) *Climate since A.D. 1500.*London: Routledge, pp. 572-591.

Peltier, W. R. (1974) 'The impulse response of a Maxwell Earth', *Reviews of Geophysics,* 12, (4), pp. 649-669.

Peltier, W. R. (2004) 'Global Glacial Isostasy and the Surface of the Ice-Age Earth: The ICE-5G (VM2) Model and GRACE', *Annual Review of Earth and Planetary Sciences,* 32, (1), pp. 111-149.

Peltier, W. R. and Drummond, R. (2008) 'Rheological stratification of the lithosphere: A direct inference based upon the geodetically observed pattern of the glacial isostatic adjustment of the North American continent', *Geophysical Research Letters,* 35, (16), pp. L16314.

Pollack, H. N., Hurter, S. J. and Johnson, J. R. (1993) 'Heat flow from the Earth's interior: Analysis of the global data set', *Reviews of Geophysics,* 31, (3), pp. 267-280.

Pollard, D. and DeConto, R. M. (2012) 'A simple inverse method for the distribution of basal sliding coefficients under ice sheets, applied to Antarctica', *The Cryosphere,* 6, (5), pp. 953-971.

Pollitz, F. F. (2005) 'Transient rheology of the upper mantle beneath central Alaska inferred from the crustal velocity field following the 2002 Denali earthquake', *Journal of Geophysical Research: Solid Earth,* 110, (B8), pp. n/a-n/a.

Price, S. F., Conway, H. and Waddington, E. D. (2007) 'Evidence for late Pleistocene thinning of Siple Dome, West Antarctica', *J. Geophys. Res.,* 112, (F3), pp. F03021.

Pritchard, H. D., Arthern, R. J., Vaughan, D. G. and Edwards, L. A. (2009) 'Extensive dynamic thinning on the margins of the Greenland and Antarctic ice sheets', *Nature,* 461, (7266), pp. 971-975.

Pritchard, H. D. and Vaughan, D. G. (2007) 'Widespread acceleration of tidewater glaciers on the Antarctic Peninsula', *J. Geophys. Res.,* 112, (F3), pp. F03S29.

Pudsey, C. J. and Evans, J. (2001) 'First survey of Antarctic sub–ice shelf sediments reveals mid-Holocene ice shelf retreat', *Geology,* 29, (9), pp. 787-790.

Rack, W. and Rott, H. (2004) 'Pattern of retreat and disintegration of the Larsen B ice shelf, Antarctic Peninsula', *Annals of Glaciology*, 39, pp. 505-510.

Ranalli, G. (1995) *Rheology of the earth.* London: Chapman & Hall.

Retzlaff, R. and Bentley, C. R. (1993) 'Timing of stagnation of ice stream C, West Antarctica, from short- pulse radar studies of buried surface crevasses', *Journal of Glaciology*, 39, (133), pp. 553-561.

Rignot, E., Bamber, J. L., van den Broeke, M. R., Davis, C., Li, Y., van de Berg, W. J. and van Meijgaard, E. (2008) 'Recent Antarctic ice mass loss from radar interferometry and regional climate modelling', *Nature Geosci*, 1, (2), pp. 106-110.

Rignot, E., Casassa, G., Gogineni, P., Krabill, W., Rivera, A. and Thomas, R. (2004) 'Accelerated ice discharge from the Antarctic Peninsula following the collapse of Larsen B ice shelf', *Geophys. Res. Lett.*, 31, (18), pp. L18401.

Rignot, E., Casassa, G., Gogineni, S., Kanagaratnam, P., Krabill, W., Pritchard, H., Rivera, A., Thomas, R., Turner, J. and Vaughan, D. (2005) 'Recent ice loss from the Fleming and other glaciers, Wordie Bay, West Antarctic Peninsula', *Geophys. Res. Lett.*, 32, (7), pp. L07502.

Rignot, E., Mouginot, J. and Scheuchl, B. (2011) 'Ice Flow of the Antarctic Ice Sheet', *Science*.

Riva, R. E. M., Gunter, B. C., Urban, T. J., Vermeersen, B. L. A., Lindenbergh, R. C., Helsen, M. M., Bamber, J. L., van de Wal, R. S. W., van den Broeke, M. R. and Schutz, B. E. (2009) 'Glacial Isostatic Adjustment over Antarctica from combined ICESat and GRACE satellite data', *Earth and Planetary Science Letters*, 288, (3-4), pp. 516-523.

Rott, H., Eineder, M., Nagler, T. and Floricioiu, D. (2008) 'New Results on Dynamic Instability of Antarctic Peninsula Glaciers detected by TerraSAR-X Ice Motion Analysis', *Proceedings of 7th European Conference on Synthetic Aperture Radar (EUSAR)*, pp. VDE Verlag, Berlin, Germany, 159-162.

Rott, H., Müller, F., Nagler, T. and Floricioiu, D. (2011) 'The imbalance of glaciers after disintegration of Larsen-B ice shelf, Antarctic Peninsula', *The Cryosphere*, 5, (1), pp. 125-134.

Rott, H., Skvarca, P. and Nagler, T. (1996) 'Rapid Collapse of Northern Larsen Ice Shelf, Antarctica', *Science,* 271, (5250), pp. 788-792.

Rutt, I. C., Hagdorn, M., Hulton, N. R. J. and Payne, A. J. (2009) 'The Glimmer community ice sheet model', *J. Geophys. Res.,* 114, (F2), pp. F02004.

Sato, T., Larsen, C. F., Miura, S., Ohta, Y., Fujimoto, H., Sun, W., Motyka, R. J. and Freymueller, J. T. (2011) 'Reevaluation of the viscoelastic and elastic responses to the past and present-day ice changes in Southeast Alaska', *Tectonophysics,* 511, (3–4), pp. 79-88.

Scambos, T. A., Berthier, E., Haran, T., Shuman, C. A., Cook, A. J., Ligtenberg, S. R. M. and Bohlander, J. (2014) 'Detailed ice loss pattern in the northern Antarctic Peninsula: widespread decline driven by ice front retreats', *The Cryosphere Discuss.,* 8, (3), pp. 3237-3261.

Scambos, T. A., Bohlander, J. A., Shuman, C. A. and Skvarca, P. (2004) 'Glacier acceleration and thinning after ice shelf collapse in the Larsen B embayment, Antarctica', *Geophys. Res. Lett.,* 31, (18), pp. L18402.

Schön, N., Zammit-Mangion, A., Bamber, J. L., Rougier, J., Flament, T., Rémy, F. and Luthcke, S. B. (2014) 'Simultaneous solution for mass trends on the West Antarctic Ice Sheet', *The Cryosphere Discuss.,* 8, (3), pp. 2995-3035.

Shapiro, N. M. and Ritzwoller, M. H. (2004) 'Inferring surface heat flux distributions guided by a global seismic model: particular application to Antarctica', *Earth and Planetary Science Letters,* 223, (1–2), pp. 213-224.

Shepherd, A., Ivins, E. R., A, G., Barletta, V. R., Bentley, M. J., Bettadpur, S., Briggs, K. H., Bromwich, D. H., Forsberg, R., Galin, N., Horwath, M., Jacobs, S., Joughin, I., King, M. A., Lenaerts, J. T. M., Li, J., Ligtenberg, S. R. M., Luckman, A., Luthcke, S. B., McMillan, M., Meister, R., Milne, G., Mouginot, J., Muir, A., Nicolas, J. P., Paden, J., Payne, A. J., Pritchard, H., Rignot, E., Rott, H., Sørensen, L. S., Scambos, T. A., Scheuchl, B., Schrama, E. J. O., Smith, B., Sundal, A. V., van Angelen, J. H., van de Berg, W. J., van den Broeke, M. R., Vaughan, D. G., Velicogna, I., Wahr, J., Whitehouse, P. L., Wingham, D. J., Yi, D., Young, D. and Zwally, H. J. (2012) 'A Reconciled Estimate of Ice-Sheet Mass Balance', *Science,* 338, (6111), pp. 1183-1189.

Shuman, C. A., Berthier, E. and Scambos, T. A. (2011) '2001-2009 elevation and mass losses in the Larsen A and B embayments, Antarctic Peninsula', *Journal of Glaciology,* 57, (204), pp. 737-754.

Simms, A. R., Ivins, E. R., DeWitt, R., Kouremenos, P. and Simkins, L. M. (2012) 'Timing of the most recent Neoglacial advance and retreat in the South Shetland Islands, Antarctic Peninsula: insights from raised beaches and Holocene uplift rates', *Quaternary Science Reviews,* 47, (0), pp. 41-55.

Simpson, M. J. R., Wake, L., Milne, G. A. and Huybrechts, P. (2011) 'The influence of decadal- to millennial-scale ice mass changes on present-day vertical land motion in Greenland: Implications for the interpretation of GPS observations', *Journal of Geophysical Research: Solid Earth,* 116, (B2), pp. B02406.

Spada, G. and Stocchi, P. (2006) *The Sea Level Equation, Theory and Numerical Examples.* Roma: Aracne.

Steffen, H. and Wu, P. (2011) 'Glacial isostatic adjustment in Fennoscandia—A review of data and modeling', *Journal of Geodynamics,* 52, (3–4), pp. 169-204.

Taylor, F. W., Bevis, M. G., Dalziel, I. W. D., Smalley, R., Frohlich, C., Kendrick, E., Foster, J., Phillips, D. and Gudipati, K. (2008) 'Kinematics and segmentation of the South Shetland Islands-Bransfield basin system, northern Antarctic Peninsula', *Geochemistry, Geophysics, Geosystems,* 9, (4), pp. Q04035.

Thomas, E. R., Marshall, G. J. and McConnell, J. R. (2008) 'A doubling in snow accumulation in the western Antarctic Peninsula since 1850', *Geophys. Res. Lett.,* 35, (1), pp. L01706.

Thomas, I. D., King, M. A., Bentley, M. J., Whitehouse, P. L., Penna, N. T., Williams, S. D. P., Riva, R. E. M., Lavallee, D. A., Clarke, P. J., King, E. C., Hindmarsh, R. C. A. and Koivula, H. (2011) 'Widespread low rates of Antarctic glacial isostatic adjustment revealed by GPS observations', *Geophys. Res. Lett.,* 38, (22), pp. L22302.

Thompson, L. G. (1994) 'Climate since AD 1510 on Dyer Plateau, Antarctic Peninsula: evidence for recent climate change', *Annals of Glaciology,* 20, pp. 420-426.

Trusel, L. D., Frey, K. E., Das, S. B., Munneke, P. K. and van den Broeke, M. R. (2013) 'Satellite-based estimates of Antarctic surface meltwater fluxes', *Geophysical Research Letters,* 40, (23), pp. 2013GL058138.

Turner, J., Lachlan-Cope, T. A., Marshall, G. J., Morris, E. M., Mulvaney, R. and Winter, W. (2002) 'Spatial variability of Antarctic Peninsula net surface mass balance', *J. Geophys. Res.,* 107, (D13), pp. 4173.

Vaughan, D. G., Marshall, G. J., Connolley, W. M., Parkinson, C., Mulvaney, R., Hodgson, D. A., King, J. C., Pudsey, C. J. and Turner, J. (2003) 'Recent Rapid Regional Climate Warming on the Antarctic Peninsula', *Climatic Change,* 60, (3), pp. 243-274.

Wahr, J., Khan, S. A., van Dam, T., Liu, L., van Angelen, J. H., van den Broeke, M. R. and Meertens, C. M. (2013) 'The use of GPS horizontals for loading studies, with applications to northern California and southeast Greenland', *Journal of Geophysical Research: Solid Earth,* 118, (4), pp. 1795-1806.

Wahr, J., Molenaar, M. and Bryan, F. (1998) 'Time variability of the Earth's gravity field: Hydrological and oceanic effects and their possible detection using GRACE', *J. Geophys. Res.,* 103, (B12), pp. 30205-30229.

Watcham, E. P., Bentley, M. J., Hodgson, D. A., Roberts, S. J., Fretwell, P. T., Lloyd, J. M., Larter, R. D., Whitehouse, P. L., Leng, M. J., Monien, P. and Moreton, S. G. (2011) 'A new Holocene relative sea level curve for the South Shetland Islands, Antarctica', *Quaternary Science Reviews,* 30, (21–22), pp. 3152-3170.

Wendt, J., Rivera, A., Wendt, A., Bown, F., Zamora, R., Casassa, G. and Bravo, C. (2010) 'Recent ice-surface-elevation changes of Fleming Glacier in response to the removal of the Wordie Ice Shelf, Antarctic Peninsula', *Annals of Glaciology,* 51, (55), pp. 97-102.

Whitehouse, P. L., Bentley, M. J. and Le Brocq, A. M. (2012a) 'A deglacial model for Antarctica: geological constraints and glaciological modelling as a basis for a new model of Antarctic glacial isostatic adjustment', *Quaternary Science Reviews,* 32, pp. 1-24.

Whitehouse, P. L., Bentley, M. J., Milne, G. A., King, M. A. and Thomas, I. D. (2012b) 'A new glacial isostatic adjustment model for Antarctica: calibrated and tested using

observations of relative sea-level change and present-day uplift rates', *Geophysical Journal International*.

Wiens, D. A., Seama, N. and Conder, J. A. (2006) 'Mantle Structure and Flow Patterns Beneath Active Back-Arc Basins Inferred From Passive Seismic and Electromagnetic Methods', in Christie, D. M., Fisher, C. R., Lee, S. M. and Givens, S.(eds) *Back-Arc Spreading Systems: Geological, Biological, Chemical, and Physical Interactions.* Vol. 166 Washington, DC: AGU, pp. 303.

Williams, S. (2008) 'CATS: GPS coordinate time series analysis software', *GPS Solutions,* 12, (2), pp. 147-153.

Williams, S. D. P. (2003) 'The effect of coloured noise on the uncertainties of rates estimated from geodetic time series', *Journal of Geodesy,* 76, (9), pp. 483-494.

Willis, M. J., Melkonian, A. K., Pritchard, M. E. and Rivera, A. (2012) 'Ice loss from the Southern Patagonian Ice Field, South America, between 2000 and 2012', *Geophysical Research Letters,* 39, (17), pp. L17501.

Wilson, T. J., Gohl, K. and López-Martínez, J. (2011) 'Understanding Earth's Polar Challenges: International Polar Year 2007-2008', in Krupnik, I., et al.(ed). Vol. Occasional Publications Series No. 69 CCI Press, pp. 273-293.

Wright, A. P., White, D. A., Gore, D. B. and Siegert, M. J. (2008) 'Chapter 12 Antarctica at the Last Glacial Maximum, Deglaciation and the Holocene', in Fabio, F. and Martin, S.(eds) *Developments in Earth and Environmental Sciences.* Vol. Volume 8 Elsevier, pp. 531-570.

Yokoyama, Y., Lambeck, K., De Deckker, P., Johnston, P. and Fifield, L. K. (2000) 'Timing of the Last Glacial Maximum from observed sea-level minima', *Nature,* 406, (6797), pp. 713-716.

Zagorodnov, V., Nagornov, O., Scambos, T. A., Muto, A., Mosley-Thompson, E., Pettit, E. C. and Tyuflin, S. (2012) 'Borehole temperatures reveal details of 20th century warming at Bruce Plateau, Antarctic Peninsula', *The Cryosphere,* 6, (3), pp. 675-686.

Zwally, H., Giovinetto, M. B., Beckley, M. A. and Saba, J. L. (2012) '(GSFC Cryospheric Sciences Laboratory, http://icesat4.gsfc.nasa.gov/cryo_data/ant_grn_drainage_systems.php)', [Online]. Available at: (Accessed: 06/10/2013).